MEASURING THE COSMIC MICROWAVE BACKGROUND RADIATION FROM CHILE

A Dissertation

Presented to the Faculty of the Graduate School

of Cornell University

in Partial Fulfillment of the Requirements for the Degree of

Doctor of Philosophy

by

Jason Roland Stevens

December 2020

MEASURING THE COSMIC MICROWAVE BACKGROUND RADIATION FROM CHILE

Jason Roland Stevens, Ph.D.

Cornell University 2020

Precise measurement of the cosmic microwave background (CMB) radiation holds the key to a surprising quantity of knowledge about cosmology and the early universe. Measurement of the power spectrum of the CMB yields information about inflation and gravitational waves in the early universe, the mass of the neutrino, and the number of effective neutrino species. As CMB photons pass through our universe, the interaction they have with its contents yield even more information. Scattering of the CMB photons off of the electrons in galaxy clusters can be used to extract the movement of those galaxy clusters, and gravitational lensing of the CMB photons tells the story of the evolution of massive structures in our universe. Extracting this information requires an extreme level of precision and care in the detection of these photons.

This dissertation covers a number of subjects related to measuring CMB photons with telescopes in Chile. I first discuss the superconducting transition edge sensors used on some of these telescopes, and the testing and characterization of these sensors for the Simons Observatory. It is necessary to multiplex the detector signals to reduce thermal load on the cryostat cold stages, so I then discuss testing and characterization strategies for superconducting multiplexers. This begins with characterization of the time domain multiplexing chips used on Advanced ACTPol, and leads into characterization of microwave multiplexing chips like those that will be used in the Simons Observatory. Next, I

present methods for designing and optimizing wide area CMB survey strategies from Chile, including the strategies that are used in Advanced ACTPol and the strategies that will be used in the Simons Observatory. I then describe recent results from the Atacama Cosmology Telescope that this work has contributed to. I conclude by summarizing the improvements we will see in measurements of the CMB from new observatories in the coming years.

BIOGRAPHICAL SKETCH

Jason grew up in Anchorage, Alaska. He earned an Associate's of Science from Paradise Valley Community College in Phoenix, Arizona in 2011 before transferring to Arizona State University. At ASU, he earned dual Bachelor's of Science in Physics and Mathematics. His interest in mathematics covers primarily algebra, number theory, and cryptography.

His undergraduate research in physics was on the KOTO project at J-PARC, an experiment to find the branching ratio $K_L^0 \to \pi^0 \nu \bar{\nu}$. He wrote data acquisition code and performed Monte Carlo simulations of the experiment.

Jason graduated from ASU in 2014 to attend graduate school at Cornell University for physics. He studied observational cosmology, and contributed to the Atacama Cosmology Telescope, the Simons Observatory, CMB-S4, and CCAT-prime. He focused on telescope survey strategies and superconducting detectors and readout.

Figure 1: Jason near Licancabur volcano in the Atacama desert, Chile. This photograph was taken near the site of the telescopes described in this document. The animals in the background are Vicuña.

Dedicated to my family - past, present, and future.

ACKNOWLEDGEMENTS

This manuscript would not exist if it weren't for the influence of a number of people. Here, I make an attempt to enumerate and acknowledge those who were most directly responsible.

Of course, my advisor, Mike Niemack, has certainly been the most immediately influential. Thank you for your guidance.

In the early days of my research in cosmology, a few people transferred vast amounts of knowledge to me in order to form a basis that my research built upon. To those people: Shawn Henderson, Francesco DeBernardis, and Brian Koopman, thank you.

I have had the good fortune of working with some very nice people over the past six years, and we have all had influence over each other and contributed to one another's work continually. Of course I must therefore also thank the rest of our team at Cornell: Nick Cothard, Eve Vavagiakis, Patricio Gallardo, Cody Duell, Steve Choi, and Thuong Hoang.

Some of our other collaborators outside of Cornell have also played a big role in my work. I have to specially acknowledge Matthew Hasselfield for this. Collectively, our collaborators at both Princeton University and the National Institute of Standards and Technology also deserve credit.

I would not even be studying at Cornell today if it hadn't been for the three years of experience I had doing research in kaon decay at Arizona State, so I owe great thanks to my undergraduate research advisor Joseph Comfort and his graduate student, Duncan McFarland. I would never have met Joe if it weren't for Jonathan Alfson, so I must thank him, too.

I have had a number of wonderful teachers over the years, but a few stand out to me. In no particular order, thank you to Mike Hamm, Scott Massey, John

Jones, Andrew Bremner, Mike Treacy, Matthias Kawski, Jay Taylor, and Richard Lebed. And to Nathan Ellis, my machine shop instructor and informal therapist through most of graduate school.

I was inspired to study physics and mathematics after reading a handful of books. Although I have never met these people, I am certain that I would not even have been to college if it weren't for the influence of these authors, so I thank them as well. To Stephen Hawking, for "A Brief History of Time." To Bruce Schneier, for "Applied Cryptography." To Jan Gullberg, for "Mathematics: From the Birth of Numbers." To Richard Feynman, for his "Lectures on Physics."

Thank you to some of my closest friends, whom I've stayed in touch with through the strange time period this text was written in. Among you, especially, Jeremy Van Marter, Tim Ohle, and Brian Edmunds. I tip my hat to the bands I have been in, Black Pearl and Tirade; and to the Cornell astronomy department softball team, The Big Bangers.

Thank you to my parents, and to my wife Nicole.

TABLE OF CONTENTS

LIST OF TABLES

LIST OF FIGURES

CHAPTER 1

INTRODUCTION AND COSMOLOGY

Here I briefly describe the current state of cosmology and a few examples of knowledge that can be obtained from CMB measurements. I will cover inflation, neutrinos, dark matter, and dark energy. These topics are summarized in greater detail in [63], [24], and [1], for example.

1.1 The Cosmic Microwave Background Radiation

The Cosmic Microwave Background radiation is the oldest light in the universe; of all the direct measurements available to modern instrumentation, it is the farthest back in time we can look. In the future, measurements of the cosmic neutrino background may allow us to view an earlier time, but for now, the CMB is the best we can do. Any speculation about earlier times must be inferred from models.

The universe has long been observed to be expanding. The farther back in time we consider, the more the universe increases in density and temperature. At very early times, the density and temperature would have been great enough to ionize the hydrogen in the universe; the density of free charges frequently scattered photons and made the universe opaque to light. When the universe cooled sufficiently, it became transparent, and many of those scattered photons were able to travel undisturbed to this day. Those photons form the CMB.

The CMB is approximately isotropic. It follows a black body spectrum with a mean temperature ~ 2.7 K. The low temperature is a result of the original black body spectrum red-shifting as the universe expands. The CMB formed at red-

shift ~ 1100, near the beginning of the universe. I say it is *approximately* isotropic because there are subtle anisotropies in the CMB for a number of reasons, and these anisotropies are the focus of CMB measurements today.

1.1.1 Primary Anisotropies

Primary anisotropies are anisotropies in the CMB that are the result of the initial conditions of the CMB at the surface of last scattering. They are the result of density fluctuations in the universe at that time, with overdense regions corresponding to cooler photons (they had to travel out of a deeper gravitational potential well, and thus lost more energy; this is called the Sachs-Wolfe effect) and underdense regions appearing warmer. The primary anisotropies give us a photograph of how the universe appeared at redshift 1100, the earliest time we can measure.

1.1.2 Secondary Anisotropies

CMB photons have had over 13 billion years to travel through the universe and many have interacted with the contents of the universe during that time. The effect of these interactions leave secondary anisotropies in the CMB. Since the CMB spectrum is so well characterized, these interactions are invertable and can teach us about the matter that the CMB has interacted with over the ages.

Gravitational lensing of the CMB occurs as CMB photons pass near dense regions of space. Not only can gravitational lensing of the CMB yield information about the structure of matter throughout the universe, but it is also valuable to

measure this lensing in order to de-lens the CMB data and get a correct measurement of the primary anisotropies [40].

CMB photons scattering off free electrons in galaxy clusters will exchange momentum with these electrons in an inverse Compton scattering process. This is called the Sunyaev-Zel'dovich (SZ) effect. This effect is often split into multiple contributing parts in analysis. The thermal SZ (tSZ) effect constitutes the component of momentum transmitted due to the thermal motion of the electrons. The kinetic SZ (kSZ) effect constitutes the component of momentum transmitted due to the bulk motion of the electrons, and therefore to the velocity of the associated galaxy cluster. The relativistic SZ (rSZ) effect is a relativistic correction to the change in momentum of the scattered photons [12].

1.2 Tools for Cosmology

1.2.1 The Friedmann Equation

Although modern cosmology is complicated, there are a few underlying themes that guide the theory. One is the Friedmann equation, which relates the expansion rate of the universe to its contents. It is derived by assuming an isotropic, homogeneous universe, and applying the Einstein equation of general relativity. It can be written:

$$H^2 \equiv \left(\frac{1}{a}\frac{d^2a}{dt^2}\right)^2 = H_0^2\left(\Omega_r a^{-4} + \Omega_m a^{-3} + \Omega_k a^{-2} + \Omega_\Lambda\right) \tag{1.1}$$

Here, H is the Hubble parameter, and H_0 is the Hubble parameter today. The scale factor, a, describes the expansion of space; the distance between two ob-

jects grows proportionally to a as long as they move with the expanding universe (the "Hubble flow"), with $a = 1$ by definition today. The scale factor is also related to the redshift z by $a = (1 + z)^{-1}$.

The remaining terms, Ω_X, describe the content of the universe today, each as a fraction of the *critical density* ρ_{crit}; ρ_{crit} is the energy density required to maintain a flat universe. Ω_r is the fraction of relativistic particles, which is largely photons, but includes anything with energy much greater than its rest mass. Ω_m is the matter fraction, including dark matter, or anything with smaller kinetic energy than rest mass. Ω_k is due to the curvature of space, which is close to zero and often is assumed to be zero. Finally, Ω_Λ is due to a cosmological constant, which is the simplest model of dark energy [24][63]. Table 1.1 provides recent constraints on these parameters.

If only Ω_m or Ω_r dominate the energy content of the universe, then the expansion of the universe slows. However, a universe dominated by Ω_Λ will expand exponentially. Note that, at very early times, a is small, so the Ω_r term is the largest contribution. Later, Ω_m becomes largest. Eventually, Ω_Λ dominates, after the other components have been diluted by expansion.

Measurements that reveal how the universe expands over time therefore also reveal the composition of the universe. Redshift surveys of type I supernovae, which all have the same luminosity, can reveal $H(z)$ [22]. CMB measurements can, too, even at late times by using secondary anisotropies.

Parameter	Value
$\Omega_r h^2$	2.47×10^{-5}
Ω_m	0.3111 ± 0.0056
Ω_b	0.02233 ± 0.00015
Ω_Λ	0.6889 ± 0.0056
H_0	67.27 ± 0.6 km s^{-1}Mpc^{-1}

Table 1.1: Some of the parameters of the Friedmann equation, Eqn. 1.1, as compiled by the Planck collaboration in 2018 [6], except for $\Omega_r h^2$, which comes from WMAP [39]. In Ω_r, I chose to leave the value as originally expressed in the result which includes a factor of h^2; here, $h = H_0/100$. Note that H_0 as measured by CMB experiments differs from H_0 as measured by astronomical observations at the 4.4σ level [53].

1.2.2 The Boltzmann Equations

The thermodynamic history of the universe, when combined with known physics of chemical, nuclear, and high energy particle interactions, explains the concentration of the universes' various constituents. The Boltzmann equation describes the concentrations of particles in systems that are thermodynamically coupled. It can apply to any chemical, nuclear, or particle interaction even in non-equilibrium conditions. By applying the equipartition theorem to the initial state of the universe to define initial conditions and then plugging known physics into the Boltzmann equation, the concentration of each particle type in the universe as a function of time can be predicted. As a specific example, the reaction $e^- + p \rightleftharpoons H + \gamma$ can be used to describe the formation of the CMB.

It is typical to assume both equilibrium conditions and reversible reactions. These assumptions give accurate answers in a cosmological context and simplify the equation. The expanding universe must be taken into account, since expansion dilutes the particle concentrations and reduces the reaction rate. For

a reaction like $A + B \rightleftharpoons C + D$, the equation looks like

$$\frac{1}{a^3}\frac{d(n_A a^3)}{dt} = n_A^{(0)} n_B^{(0)} \langle \sigma v \rangle \left(\frac{n_C n_D}{n_C^{(0)} n_D^{(0)}} - \frac{n_A n_B}{n_A^{(0)} n_B^{(0)}} \right) \tag{1.2}$$

where n_X is the concentration of X; $n_X^{(0)}$ is the species-dependent equilibrium number density (related to the chemical potential μ by $n_X/n_X^{(0)} = e^{-\mu/T}$), and $\langle \sigma v \rangle$ is related to the scattering cross-section and either must be measured or derived from fundamental physics [24]. In the context of early universe interactions, the chemical potential is usually equal to the particles' rest mass.

This says that the rate of change of the concentration of a particle species A is proportional to a reaction rate; multiply the concentrations of the reactants to get a negative contribution (this product is proportional to the rate of interactions decreasing A by converting it to products) and multiply the concentrations of the products to get a positive contribution (same, for the back-reaction). Also, since the left-hand side is proportional to H, if the reaction rate is not sufficiently large compared to the universal expansion, the reaction will cease; this is called "freeze out" [63].

1.2.3 The CMB Power Spectrum

The usual way to study CMB anisotropies is through the CMB power spectrum. The CMB map is projected onto its spherical harmonic components, $Y_\ell^m(\theta, \phi)$. The contribution for each ℓ is defined by

$$\langle \Delta T(\hat{n}) \Delta T(\hat{n'}) \rangle = \sum_l \sum_m C_\ell Y_\ell^m(\hat{n}) Y_\ell^{-m}(\hat{n'}) = \sum_l C_\ell \left(\frac{2\ell + 1}{4\pi} \right) P_\ell(\hat{n} \cdot \hat{n'}) \tag{1.3}$$

where $\hat{n}$, $\hat{n'}$ are arbitrary directions on the sky, $\Delta T(\hat{n})$ represents the temperature anisotropy (*ie* mean subtracted temperature) in the $\hat{n}$ direction. Y_ℓ^m are the spher-

ical harmonics and P_ℓ are the Legendre polynomials. Then the contribution C_ℓ, or some function of it, are typically plotted as a function of ℓ for CMB power spectrum analysis [63].

The above CMB power spectrum C_ℓ is also more explicitly described as the temperature power spectrum $C_{TT,\ell}$ in the context where CMB polarization is also being discussed. CMB polarization has not been as well measured as CMB temperature yet, and its precision measurement may reveal interesting physics, as I will soon describe. Polarization can also be described by power spectra, but it requires two sets of coefficients since photon polarization is described by a two dimensional vector space. The projection to spherical harmonics happens in a similar way, with coefficients $a_{P,\ell m}$ defined by

$$Q(\hat{n}) - iU(\hat{n}) = \sum_\ell \sum_m a^*_{P,\ell m} {}_2Y^m_\ell(\hat{n}) \tag{1.4}$$

where $Q(\hat{n}), U(\hat{n})$ are the second and third Stokes' parameters of the CMB in the $\hat{n}$ direction, and ${}_2Y$ are the spherical harmonics of spin 2.

The Q and U are directly measurable by experiment, but do depend on choice of coordinate system, so it is convenient to write the new coefficients

$$a_{E,\ell m} = -\frac{1}{2}\left(a_{P,\ell m} + a^*_{P,\ell m}\right); a_{B,\ell m} = \frac{i}{2}\left(a_{P,\ell m} - a^*_{P,\ell m}\right) \tag{1.5}$$

The new polarization scheme is usually called "E-modes" (for $a_{E,\ell m}$) and "B-modes" (for $a_{B,\ell m}$). The E-modes have parity $(-1)^\ell$, and the B-modes have parity $(-1)^{\ell+1}$; that is, under spatial reflection, the $a_{E,\ell m}$ transforms by gaining a factor $(-1)^\ell$, and the $a_{B,\ell m}$ a factor $(-1)^{\ell+1}$.

Now, similar to temperature, it is desirable to remove dependence on m and thus the dependence on choice of sky coordinates. Cross correlations between

temperature and the two new polarization modes have their own spectra. These are all described by

$$\langle a^*_{X,\ell m} a_{Y,\ell' m'} \rangle = C_{XY,\ell} \delta_{\ell\ell'} \delta_{mm'} \tag{1.6}$$

where X and Y are members of $\{T, E, B\}$. Then $C_{TT,\ell}$ is the temperature power spectrum; $C_{EE,\ell}$ and $C_{BB,\ell}$ are the E-mode and B-mode polarization power spectra, respectively; and $C_{TE,\ell}$, $C_{TB,\ell}$, and $C_{EB,\ell}$ describe correlations between T, E, B.

A power spectrum is often expressed as a function of C_ℓ, rather than the C_ℓ themselves, in order to make the data scale better at high ℓ. A common choice for this function is

$$D_\ell \equiv \frac{\ell(\ell+1)}{2\pi} C_\ell \tag{1.7}$$

1.2.4 The Matter Power Spectrum

Following [63], let the fractional mass overdensity $\delta_M(\mathbf{x}, t)$ be defined by

$$\delta_M(\mathbf{x}, t) \equiv \frac{\rho(\mathbf{x}, t) - \bar{\rho}(t)}{\bar{\rho}(t)} \tag{1.8}$$

which tells us the perturbation to the mass density field ρ (here $\bar{\rho}$ represents a spatial average). Then let $\xi(\mathbf{x}; \mathbf{x})$ be defined by

$$\xi(\mathbf{x}, \mathbf{x}') \equiv \langle \delta_M(\mathbf{x}, t) \delta_M(\mathbf{x}', t')) \rangle \tag{1.9}$$

which is an auto-correlation function for the fractional mass overdensity. Here, the appropriate t to use as an input into δ_M is the time corresponding to redshift at distance $|\mathbf{x}|$. Then the matter power spectrum is a Fourier transform of ξ,

$$\xi(\mathbf{x}, \mathbf{x}') = \int \frac{d\mathbf{k}}{(2\pi)^3} P(\mathbf{k}) e^{i\mathbf{k}\cdot(\mathbf{x}-\mathbf{x}')} \tag{1.10}$$

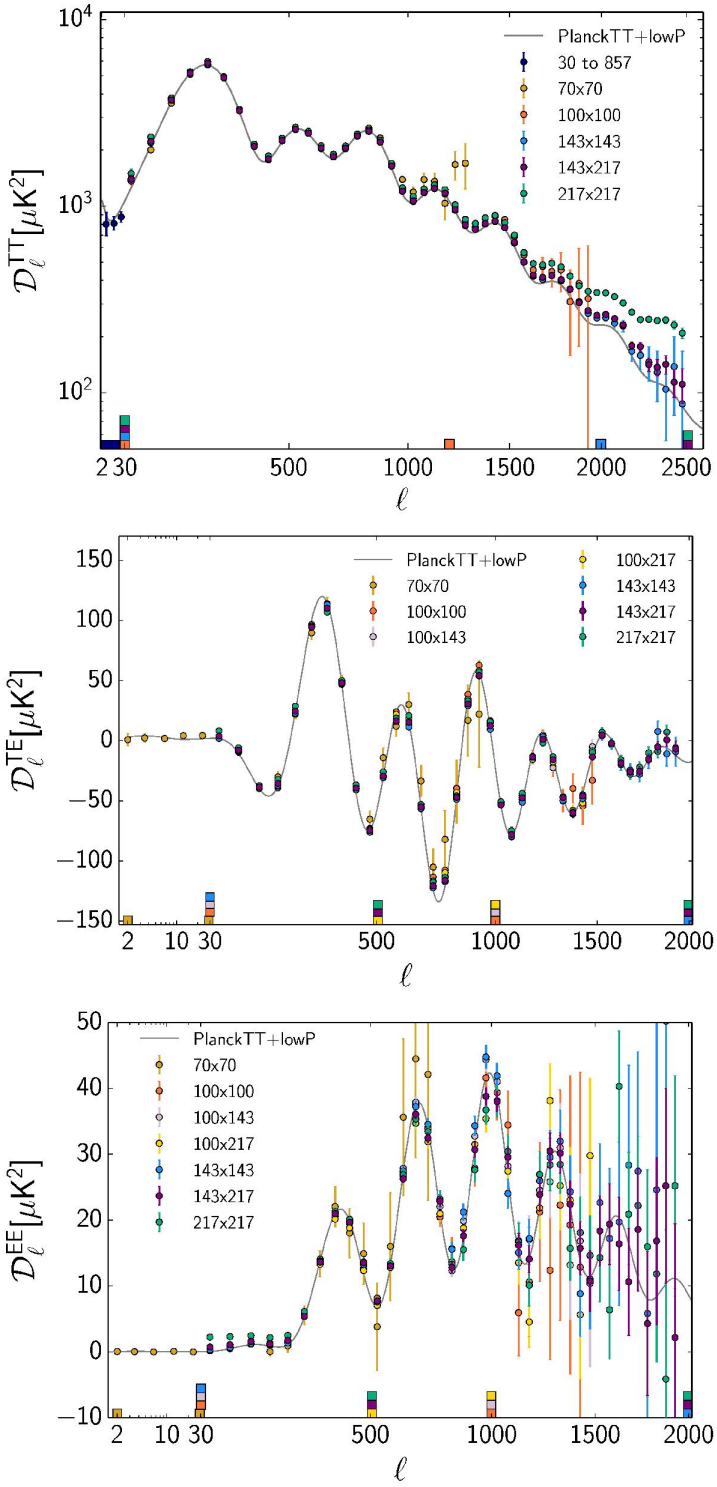

Figure 1.1: The CMB power spectrum described in Sec. 1.2.3. The top, middle, and bottom panels show the TT, TE, and EE components, respectively. Figure is from the Planck collaboration, 2015 [51].

The matter power spectrum tells us how the distribution of matter correlates on different scales. The matter power spectrum influences CMB secondary anisotropies at late times, so it can be inferred from kSZ and lensing effects. It is important for extracting information about neutrinos, dark matter, and dark energy.

1.2.5 Baryon Acoustic Oscillations

A sequence of peaks and troughs are apparent in the power spectrum in Fig. 1.1. These shapes are due to the baryon acoustic oscillations that occurred before photon decoupling. An excellent overview of these oscillations is presented in chapter 8 of [24].

Overdensities δ_M before photon decoupling led to sound waves propagating through the tightly coupled baryon and photon medium. Dark matter played a gravitational influence on the distribution of the medium, but is not coupled to other particles electromagnetically, so the sound waves are related specifically to the pressure of the baryon-photon medium.

The largest waves were the size of the sound horizon, and constitute the first acoustic peak (at lowest ℓ). The other peaks are harmonics of the first. These peaks represent statistical correlations between the density of regions of space at specific distance separations at the time of decoupling.

The acoustic peaks themselves can be shifted by dark matter annihilation [50]. Also, since the size of the sound horizon is known, it acts as a standard ruler in cosmology. Therefore, it is a probe of the evolution of the Hubble con-

Parameter	Fiducial	Planck	CMB-S4 + Planck
$100\Omega_b h^2$	2.23	±0.015	±0.003
$\Omega_c h^2$	0.120	±0.0014	±0.0006
H_0	67.27	±0.6	±0.24
$10^9 A_s$	2.1	±0.03	±0.021
n_s	0.965	±0.004	±0.002
τ	0.05	±0.01	±0.006

Table 1.2: The six Λ-CDM parameters, with fiducial values, uncertainties as measured by Planck, and forecasted uncertainty with the addition of CMB-S4. This table is reproduced from [1], except that I have updated the Planck column with more recent results from [6]. There is some redundancy with Tab. 1.1.

stant H, and can be used to constrain cosmological parameters like the behavior of dark energy.

ΛCDM

Most parameters of interest in cosmology can be calculated from only a few, given a model. The "standard model" of cosmology today is the Λ-CDM model; Λ indicates the inclusion of a cosmological constant, and CDM stands for "cold dark matter" (see Sec. 1.3.3).

The Λ-CDM model calculates all other quantities from only six input parameters, listed in Tab. 1.2. They are: The baryon fraction $\Omega_b h^2$ and the dark matter fraction $\Omega_c h^2$, the Hubble constant H_0 (or alternatively, the age of the universe), the scalar spectral index n_s, and scalar fluctuation amplitude A_s, and the reionization optical depth τ.

I have already introduced the density fractions and Hubble constant. The parameters n_s and A_s are related to the power spectrum $P(k)$ by fitting it to a

power law

$$P(k) = A_s k^{n_s - 1} \tag{1.11}$$

1.3 Examples of Physics Constrained by CMB Measurement

1.3.1 Inflation

Currently, the most popular theory describing physics of the earliest moments of the universe is the theory of slow-roll inflation. The simplest version of the theory suggests the existence of an inflaton field with a nearly flat potential that constituted the majority of the energy density of the universe at early times. The flatness of the potential would have caused it to behave like a cosmological constant, increasing the scale factor a exponentially. After a expanded by a factor[1] of between $\sim e^{47}$ and $\sim e^{57}$, the field entered a part of the potential that was no longer flat and dropped to near zero energy density. In doing so, it deposited its energy into other fields, generating what became the contents of the universe today [63][24].

If inflation occurred, it explains a number of observations about the universe. If there were any energy density in the universe prior to inflation, including due to curvature, it would be spread to practically zero density by the rapid expansion. Inflation would also provide a mechanism for thermally equilibrating distant parts of the universe with each other at early times, even if they are currently spatially separated by more than their cosmological horizon [63].

[1] This figure is estimated by Sec. 2.5 of [1], and makes certain assumptions stated therein.

Inflation would have expanded small-scale quantum fluctuations to large scales, seeding cosmological-scale perturbations to the metric of space-time and the Einstein energy-momentum tensor. These perturbations formed the large-scale structure we see today.

Importantly, tensor perturbations to the metric are only contributed to by the gravitational wave equation. Simultaneously, primordial B-modes are only contributed to by tensor perturbations to the metric. Therefore, detection of primordial B-mode polarization on large angular scales (see Fig.1.2) in the CMB suggests the existence of primordial gravitational waves, as predicted by inflation [63]. There is currently no direct evidence for inflation, so such a discovery would be groundbreaking to the field of cosmology. However, secondary anisotropies such as gravitational lensing can also create B-modes. Polarized dust emissions can contribute to a measured B-mode signal too, so the removal of the polarized dust foreground has become an important aspect of the search for primordial B-modes in recent years [38].

1.3.2 Neutrinos

Neutrinos are lightweight particles that interact through the weak nuclear force and have a very low interaction cross-section except at extremely high energies. In the standard model of particle physics they are massless, but neutrino oscillation experiments imply that they have a nonzero mass.

There are three flavors of neutrinos, each corresponding to one of the three leptons: electron, muon, and tau, although for neutrinos, mass eigenstates are not flavor eigenstates (this is what leads to the oscillations in free space). The

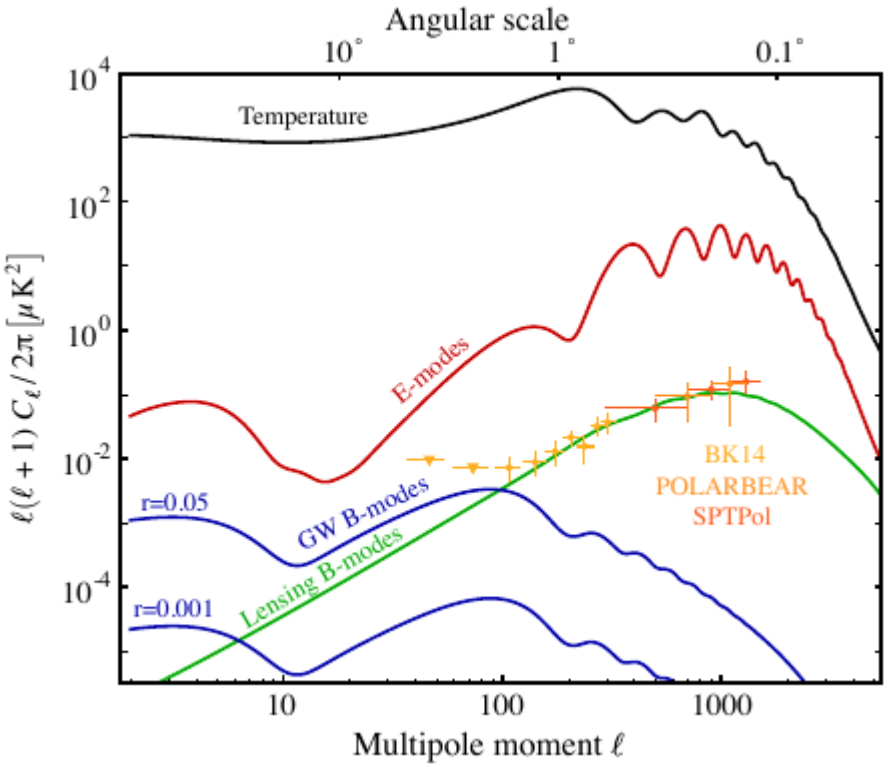

Figure 1.2: Temperature, E-mode, and primordial B-mode power spectra. In the case of the B-modes, two different predictions are shown based on different values of the tensor-to-scalar ratio r. The "lensing B-modes" curve is contribution to B-modes due to gravitational lensing of the E-modes. It is only at low ℓ that the primordial B-modes dominate. Figure is from [1].

mass difference between the mass eigenstates is known: $\Delta m^2_{21} = 7.53 \pm 0.18 \times 10^{-5}$ eV and $|\Delta m_{32}|^2 \approx 2.5 \times 10^{-3}$ eV. However, the absolute masses are not yet known [58].

Cosmology is sensitive to the sum of the neutrino masses, $\sum m_\nu$. The mass differences place a lower bound on this value of ~ 58 meV in the case of a "normal" hierarchy, and ~ 105 meV in the case of an "inverted" hierarchy [1].

Because they are so lightweight, neutrinos behave like relativistic matter at early times, contributing to Ω_r and free-streaming out of gravitational poten-

tials. Much later, as the universe's neutrino content cools, they behave more like ordinary matter and contribute instead to Ω_m. This transition occurs when the neutrino kinetic energy is of the order of the rest mass, so any phenomenon sensitive to this behavior of neutrinos is, in principle, sensitive to the neutrino mass. $\sum m_\nu$ can be probed through measurements of the CMB via the kSZ effect [48] and CMB lensing [21]; see Fig. 1.3.

Another cosmological probe of neutrino physics is measurement of $N_{\rm eff}$, the effective number of neutrino species. Probes of $N_{\rm eff}$ target the early universe. It is defined in relation to the radiation energy density:

$$\rho_r = \frac{\pi^2 k_b^4}{15\hbar^3 c^3}\left[1 + \frac{7}{8}\left(\frac{4}{11}\right)^{4/3} N_{\rm eff}\right] T_\gamma^4 \tag{1.12}$$

Under the approximation that neutrino decoupling (due to freeze-out) is instantaneous, $N_{\rm eff}$ is exactly 3. Since neutrino decoupling is not instantaneous, $N_{\rm eff}$ is really about 3.046. A measured deviation of $N_{\rm eff}$ from this value would suggest the existence of additional non-interacting massive particles, such as "sterile" neutrinos or light relics from other beyond-standard-model particles [2].

Unlike photons in the early, ionized universe, neutrinos do not interact much, so they can travel freely through space at speeds that exceed the sound speed. Their mass distribution still affects other particles gravitationally, though, so they have an effect on the amplitude and phase of the acoustic peaks in the CMB power spectrum [27]; see Fig. 1.4. This effect is distinguishable from other influences on the peaks, and is most apparent at high ℓ.

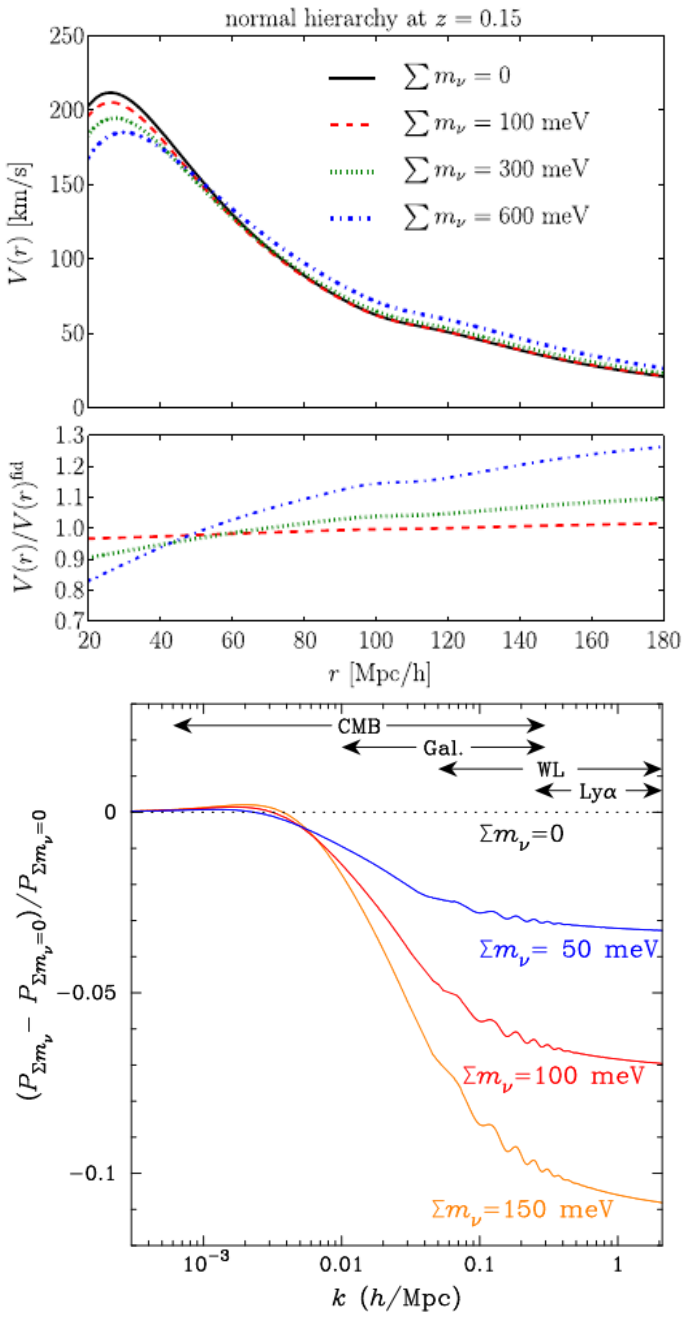

Figure 1.3: Above: Effect of $\sum m_\nu$ on the pairwise kSZ velocity. $V(r)$ is the average relative motion of a pair of galaxy clusters separated by distance r. $V(r)$ can be measured through the kSZ effect. Plot is from [48]. Below: Effect of $\sum m_\nu$ on the matter power spectrum, from [2].

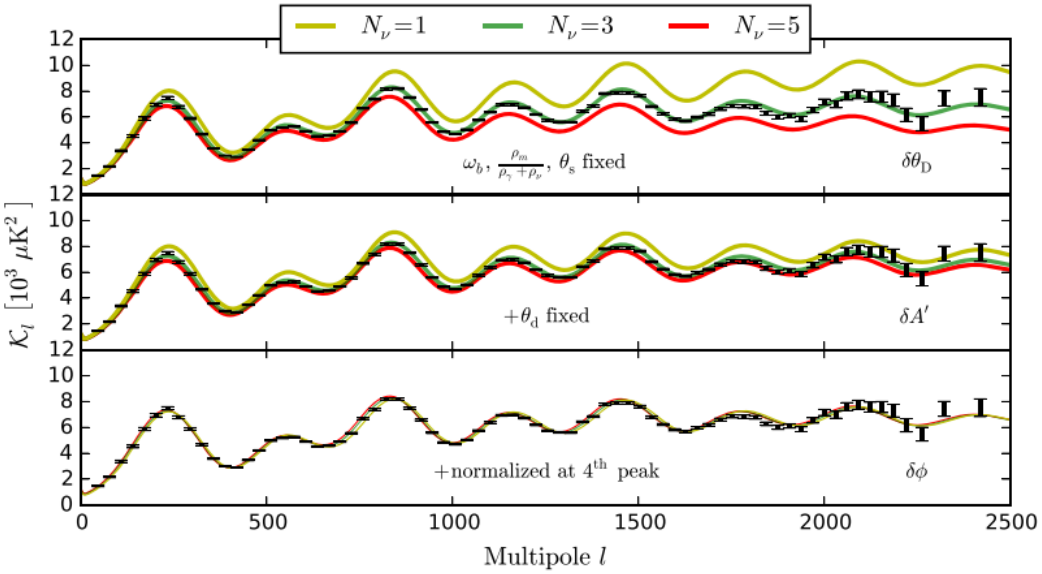

Figure 1.4: Effect of $N_{\rm eff}$ on the CMB power spectrum; y-axis is $\mathcal{K}_\ell \equiv \ell(\ell+1)/(2\pi)C_\ell$ times a function exponential in ℓ. The top panel holds the baryon density, matter to radiation ratio, and horizon at recombination fixed. The middle panel also fixes the photon damping scale. The bottom panel normalizes all three curves to the fourth acoustic peak. Figure is taken from [27].

1.3.3 Dark Matter

Most of the matter content of the universe seems to consist of beyond-standard-model particles that do not appear to interact electromagnetically, but do interact through gravitation. They are called, appropriately, dark matter. These particles have not been detected in any laboratory, but astronomy and cosmology provide convincing evidence of their existence. Dark matter was originally hinted at by studying the motion of objects within galaxies. Later, the gravitational influence of dark matter could be detected more directly through gravitational lensing. Dark matter also influences the shape of the CMB power spectrum.

The fundamental nature of dark matter is not yet known. However, that

does not mean there are not constraints on the nature of dark matter. Like other particles, the Boltzmann equation Eqn. 1.2 determines the concentration of dark matter today. Since this is a known quantity that depends on the interaction cross section $\langle \sigma v \rangle$ and dark matter particle mass m_χ, these parameters are already constrained for any dark matter candidate [24]. Also, dark matter is "cold," in that its kinetic energy is low enough that it doesn't behave relativistically; *i.e.* it contributes to Ω_m and not Ω_r. Currently, the two most popular dark matter models fall into one of two categories: Axion dark matter, and WIMP (weakly interacting massive particle) dark matter [1].

WIMPs, as the name implies, interact through the weak nuclear force. If dark matter is made of WIMPs, they may have a self-annihilating reaction that introduces energy into the universe at some low rate proportional to $\langle \sigma v \rangle / m_\chi$. The additional energy increases the photon abundance at recombination, shifting the equilibrium point in the Boltzmann equation. This introduces a small, extra abundance of ionization, which suppresses the power spectra at large ℓ and shifts the acoustic peaks by broadening the surface of last scattering [50].

Axion dark matter encompasses a large number of different models covering a wide range of masses (perhaps[2] 10^{-33} to 10^{-20} eV). In some cases, axions have degeneracy with the neutrino parameters mentioned in that section, $\sum m_\nu$ and N_{eff}; whether or not this is true depends on the axion mass [1].

[2]Wider ranges could be possible, but this is the mass range considered by [1]

1.3.4 Dark Energy

The Ω_Λ term in the Friedmann equation (Eqn. 1.1) describes the dark energy content of the universe. It behaves like a "cosmological constant" that has constant energy density throughout space, regardless of any expansion. This behavior causes the scale factor to expand exponentially. Ω_Λ is small enough that it has only made a significant contribution to a at more recent times, so it shouldn't affect the primary anisotropies. However, the effect of dark energy can be measured through secondary anisotropies.

One interesting question to address about dark energy is whether or not it is genuinely a cosmological constant, or if this is only approximate. Specifically, for each term in Eqn. 1.1, the exponent of a is related to the equation of state for the fluid described in the term. The equation of state $w \equiv P/\rho$ relates the pressure P to the density ρ, and fits into the exponent like so:

$$\rho \approx \Omega_X a^{-3(1+w)} \tag{1.13}$$

for some component X [24]. In the case of a cosmological constant, $w = -1$, an expression of the fact that dark energy exerts negative pressure. It may not be so simple, and one easy expansion of this model assumes that w is dependent on redshift z like

$$w(z) = w_0 + w_a \frac{z}{1+z} \tag{1.14}$$

for some w_0, w_a. Precision measurements of H over time could reveal a z dependence in dark energy.

The SZ and lensing effects mentioned in Sec. 1.1.2 are both sensitive to dark energy [55][47]. Additionally, there are models of dark energy that invoke a new beyond-standard-model scalar field [13]. Such a scalar field would introduce

cosmic birefringence, introducing C_{TE} and C_{TB} cross-correlations and would be an exciting indication of new physics [37].

1.4 Conclusion

There are many other things that can be studied through CMB measurements, and I have presented a few of the most interesting. There are clearly a wide range of physical models that can be explored with these instruments, capable perhaps of answering questions about the structure and origin of our universe. The final chapter, Ch. 6, will present the forecasts for current and next generation telescopes' sensitivity to these phenomena. The intervening chapters will discuss aspects of the instrumentation deployed on these telescopes. The development of this instrumentation provides a technically challenging and exciting field of study irrespective of cosmology.

CHAPTER 2

TRANSITION EDGE SENSORS

2.1 Introduction

A transition edge sensor (TES) is a superconducting material, electrically biased onto its superconducting transition, and thermally linked to a constant temperature heat bath. Since the TES is operated on the superconducting transition, its electrical resistance changes drastically if photon energy is deposited in it, providing a mechanism of detection. TESes provide a particularly high signal to noise ratio compared to other sensor technologies, making them useful for scientific research, despite their cryogenic requirements.

A TES can be operated either as a calorimeter (usually in an X-ray detection context) or a bolometer (usually in the millimeter and submillimeter range). Modern CMB telescopes typically use either TESes or magnetic kinetic inductance detectors (mKIDs), with TESes usually being more sensitive, but mKIDs easier to manufacture and read out. TES bolometers have been successfully deployed on ACT [41], the Simons Observatory [56], BICEP [35], and many other CMB observatories.

Modern TES readout involves voltage-biasing the TES, and reading the current through the TES by inductively coupling it to a SQUID. This method has good noise properties and proper impedance matching. There are a number of SQUID-based readout schemes used with these sensors today, including time domain multiplexing (TDM) [10], digital frequency domain multiplexing (dfMUX) [44], and microwave multiplexing (μ-MUX, which is technically also a

type of frequency domain multiplexing) [45].

At Cornell, TES prototypes fabricated at NIST, Berkeley, and HYPRES/SeeQC corporation were tested for the Simons Observatory. The characterization of these devices is an ongoing process that informs fabrication of the devices iteratively. This testing is thoroughly presented in [56], along with the results. The material will be reiterated here. The Simons Observatory will deploy over 60,000 TES bolometers in its polarization-sensitive focal planes [49]. These detectors will be split into six bands: "low frequency" LF-1 at ~27 GHz and LF-2 at ~39 GHz, "medium frequency" MF-1 at ~93 GHz and MF-2 at ~145 GHz, and "ultra-high frequency" UHF-1 at ~225 GHz and UHF-2 at ~285 GHz [56].

In this chapter, I begin by describing the theory of TES operation. I then describe the specific methods used to test the TES devices for the Simons Observatory. Finally, I will present the most current results of those tests.

2.2 TES Theory

As a superconductor passes through its superconducting transition temperature T_C, it rapidly transitions between the superconducting zero electrical resistance state and a state with nonzero resistance. The slope of the resistance versus temperature curve is extremely steep on that superconducting transition, so that even a small change in temperature leads to a relatively large change in electrical resistance. This phenomenon makes for a good sensor, and is the basis for the TES. Fig. 2.4 is an example of a resistance vs temperature measurement of a TES showing this superconducting transition. A thorough introduction to TES theory is described in [36], but here I will describe the most relevant portions

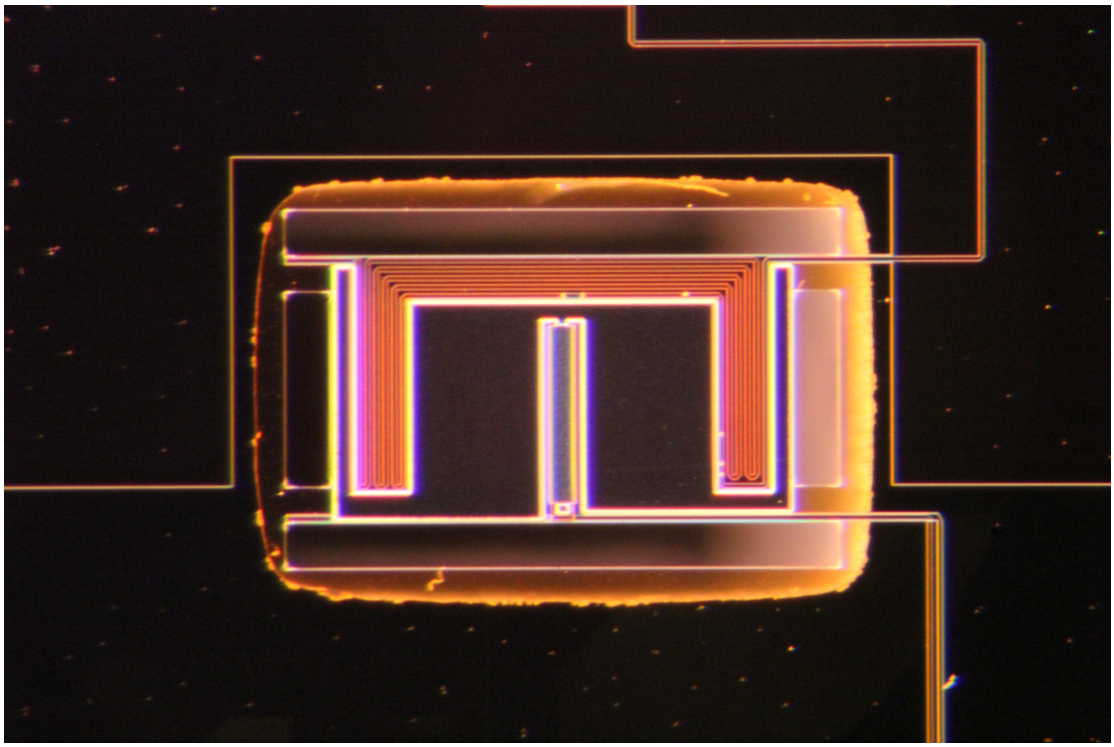

Figure 2.1: Photograph of a TES. This particular TES was fabricated at NIST. Traces and waveguides entering from the edge of the photo cross onto the bolometer island, where heat from the photons is dissipated. The traces are part of the TES bias line and pass through the superconducting element. Additional heat capacity on the bolometer island can control the heat capacity C, and the leg geometry affects the thermal conductance to the bath G.

for this chapter.

The total power into the TES is

$$P_{\mathrm{TES}} = P_{\mathrm{el}} + P_{\gamma} - P_{\mathrm{bath}} \tag{2.1}$$

where P_{el} is the electrical power into the TES due to its voltage bias, P_{γ} is the power of photons dissipated in the TES, and P_{bath} is the thermal power flowing to the temperature bath [36].

By voltage-biasing the TES, the electrical power becomes $P_{\mathrm{el}} = V^2/R_{\mathrm{TES}}$, so

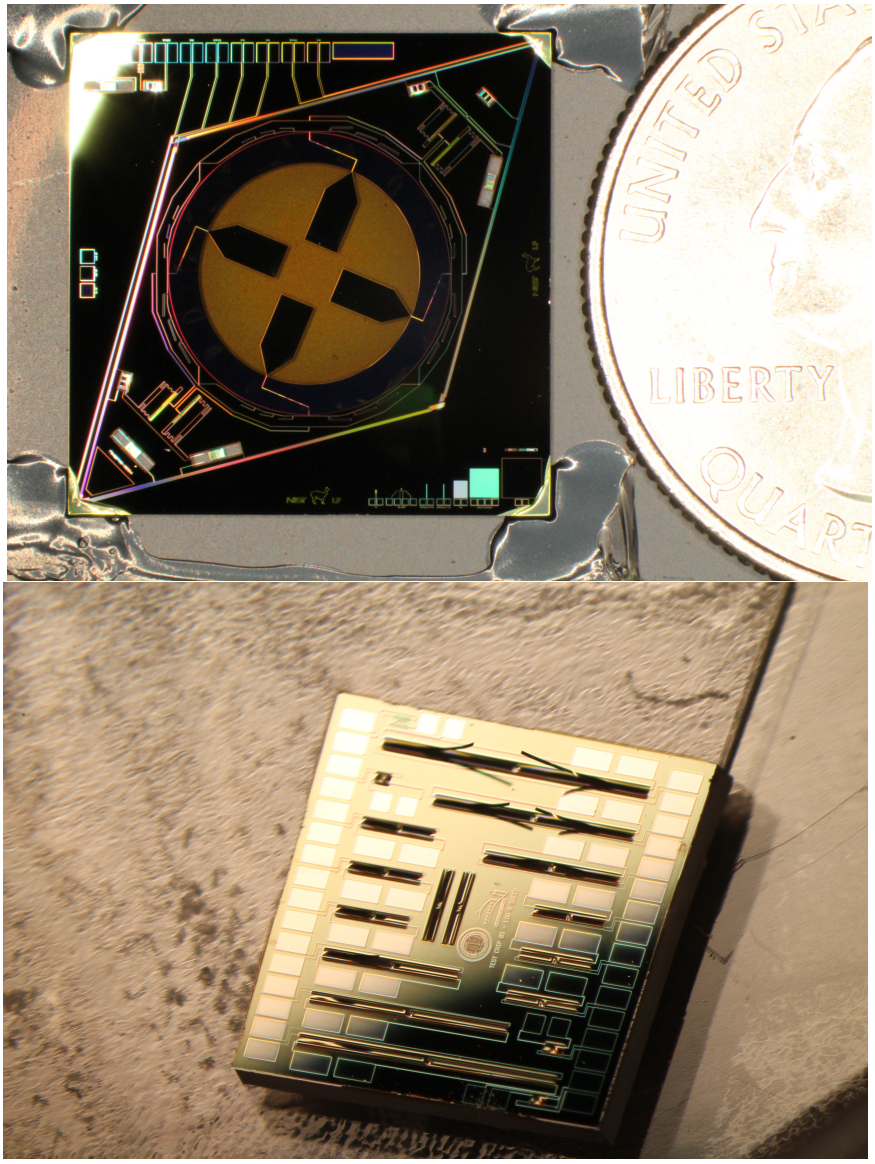

Figure 2.2: Photographs of TES test chips that were tested at Cornell for the Simons Observatory. Top: Ultra-high frequency (UHF) single pixel from NIST, with a quarter for scale. The central circular ortho-mode transducer is capable of collecting photons, which travel along a waveguide to TES bolometers near the edge of the rhombus. Many such rhombuses will be tessellated to form a detector array. Bottom: TES test die from Berkeley. This chip contains 16 distinct TES bolometers, each with different properties. In this case, the leg length of the TES is varies across the chip. Such chips are useful for probing the parameter space of physical characteristics in order to inform TES design.

the electrical power decreases as the TES resistance increases. This action serves to keep the TES on its superconducting transition. This voltage-biased arrangement is often called "negative electro-thermal feedback."

The relationship between the TES temperature, the bath temperature, and P_{bath} is well described by a power law,

$$P_{\text{bath}} = k(T^n - T_{\text{bath}}^n) \tag{2.2}$$

Here, the constant k is related to both the exponent n and the thermal conductivity to the bath G by $G = nKT^{n-1}$. T means the temperature of the TES, and T_{bath} is the temperature of the bath.

We can relate the TES power to its temperature with $P_{\text{TES}} = CdT/dt$ in Eqn. 2.1. This yields a differential equation in $T(t)$ with a general solution from which the TES thermal time constant $\tau \equiv C/G$ emerges. The heat capacity C is taken to be the heat capacity of the entire bolometer island. The thermal conductance G is due to bolometer legs connecting this heat capacity to the bath. The heat capacity can be controlled by manipulating the mass and type of material on the bolometer island, and the thermal conductance can be controlled by manipulating the leg geometry.

The TES is voltage-biased with a circuit like that in Fig. 2.3. In addition to the thermal differential equation, the TES is also modelled by an electrical differential equation

$$L\frac{dI}{dt} = V - IR_L - IR_{TES}(T, I) \tag{2.3}$$

where L is the total inductance of the circuit, I is the current through the TES, V is the bias voltage, R_{TES} is the resistance of the TES, and R_L is the equivalent load resistance, equal to the shunt resistance plus any parasitic resistance in the

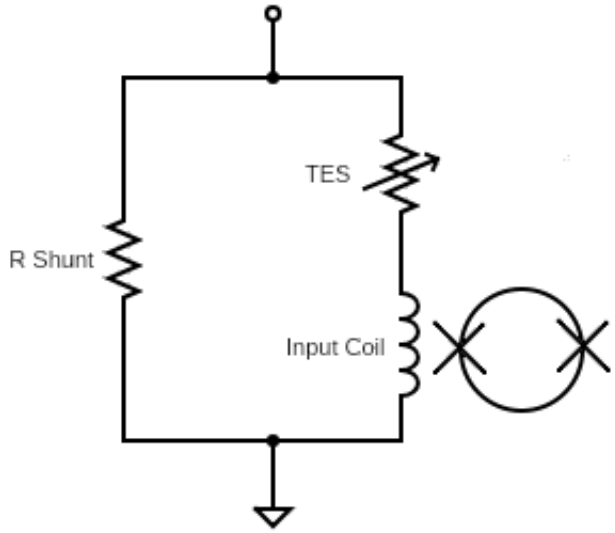

Figure 2.3: TES bias circuit. The circuit is current biased, but the shunt resistance voltage biases the TES. The TES is in series with the SQUID input coil. In a multiplexed system, many of these circuits can be chained together in series, allowing a large number of TES devices to be measured on a single TES bias line.

circuit. A similar method to solving the thermal equation yields an electrical time constant, $\tau_{\rm el} = L/(R_L + R_{\rm dyn})$ where $R_{\rm dyn} = \partial V/\partial I$ is the dynamic resistance of the TES at constant temperature.

The electrical and thermal differential equations can be linearized under approximation, then coupled to form a system of linear partial differential equations. The full solution is presented in [36]. The general solution is a linear combination of eigenvectors, each multiplied by a term exponentially decaying in time with time constants τ_+ and τ_-.

If L is small so that $\tau_+ \ll \tau_-$, then $\tau_+ \approx \tau_{\rm el}$ and $\tau_- \approx \tau_{\rm eff}$ (the effective thermal time constant, see Sec. 2.6). The stability of the TES can be related to these time constants; if a runaway solution occurs, rather than a decaying solution, the TES

will be unstable and not useful for making measurements. Simons Observatory TES devices are overdamped, so they are stable if the TES resistance is sufficiently large compared to the total load resistance. Details of the relationships between these variables, as well as details about the stability conditions, are outlined in [36], and are beyond the scope of this introduction; my aim here is mainly to convince the reader of the significance of measuring these parameters and ensuring that they are within specification for nominal performance.

Finally, a comment on noise performance of the TES. Obviously, along with creating a stable detector, minimizing noise is of supreme practical significance. Again from [36], the noise is the sum of four terms: the TES Johnson noise $S_{P_{\mathrm{TES}}}(\omega)$, the power noise $S_{P_L}(\omega)$, the thermal fluctuation noise $S_{P_{\mathrm{TFN}}}$, and the power-referred amplifier noise $S_{P_{\mathrm{amp}}}(\omega)$. In [30], the TES noise is shown to dominate over the readout noise for ACT. These noise terms increase with temperature, current, and electrical resistance, so each of those variables should be minimized within the limits of fabrication and the readout electronics.

2.3 Detector Testing and Parameters

In the following sections, I will describe the methods of testing used to characterize the Simons Observatory prototype TES detectors at Cornell. These parameters are extracted from the tests, and useful in informing TES design and fabrication:

- T_C - Superconducting transition temperature. Lower T_C suppresses detector noise, but requires additional cooling power.

- R_N - Normal resistance. The resistance of the TES in its normal (non-superconducting) state must be properly matched with the readout circuit. Lowering the resistance increases the power to current responsivity of the TES suppressing the SQUID readout noise relative to the TES noise.
- P_{sat} - Saturation power. This is equal to $P_{\mathrm{el}} + P_\gamma$ in Eqn. 2.1, although for these dark tests, $P_\gamma = 0$. P_{sat} is a function of temperature that follows Eqn. 2.2, but is often expressed at 100 mK.
- G - Thermal conductivity coupling the bolometer island to the bath. A larger G decreases the thermal time constant τ. G is also present in Eqn. 2.2 as a factor in k, so it plays a role in the bias power of the TES as a function of temperature.
- τ - Thermal time constant. In SO detectors, this time constant is slow relative to the electrical time constant; it is slow enough that it can be effectively resolved by the bias step measurements described in Sec. 2.6. The TES signal decays to its input power with this time constant. The thermal time constant must match the expected rate of change of the input signal, but it also plays an important role in detector stability.
- C - Heat capacity of the bolometer island. Measurements of G and τ reveal this parameter, which can be adjusted in order to affect τ.
- n - The exponent in Eqn. 2.2. This is highly degenerate with k in Eqn. 2.2 when fitted; this degeneracy is elaborated on in Sec. 2.5.

All tests were performed in a BlueFors dilution refrigerator. The refrigerator has a thermometer and heater on its mixing chamber stage, where the test is performed, that allows servoing to a fixed temperature. Except for the four-lead resistance measurements (which use their own custom PCB), all tests were

performed using the MCE time-domain SQUID multiplexing (TDM) system, with custom PCB and 200 $\mu\Omega$ shunt resistance. This is the same TDM readout system described in detail in Chapter 3.

2.4 Four-Lead Resistance Measurements

The simplest cryogenic test performed on the prototype Simons Observatory TES detectors was the four-lead resistance measurement. This test is capable of determining T_C and R_N. Although these parameters are also determined by the IV measurements described in Sec. 2.5, the four-lead resistance measurements are easier to perform, are more often successful in extracting meaningful data, and require less time to measure and analyze. Therefore, testing on a particular TES type will usually begin with a four-lead measurement in order to yield quick, definitive results. In fact, if a device fails to operate well with the TDM readout system used in the other tests, the four-lead resistance measurement may be the only measurement taken of that device. This is most likely to occur if T_C (or in principle R_N, though I have not experienced this situation) is sufficiently off target.

The test involves choosing an excitation current for the four lead measurement, which ideally should be well below the critical current of the detector. The temperature is set, and several resistance readings taken in order to get a statistical error bar. Then, the next temperature is chosen. Temperatures are selected in order, with fine steps. The entire process can be refined by then repeating with multiple excitation currents. A higher excitation current will reduce the statistical error bar, but reduces the measured T_C since critical current is a func-

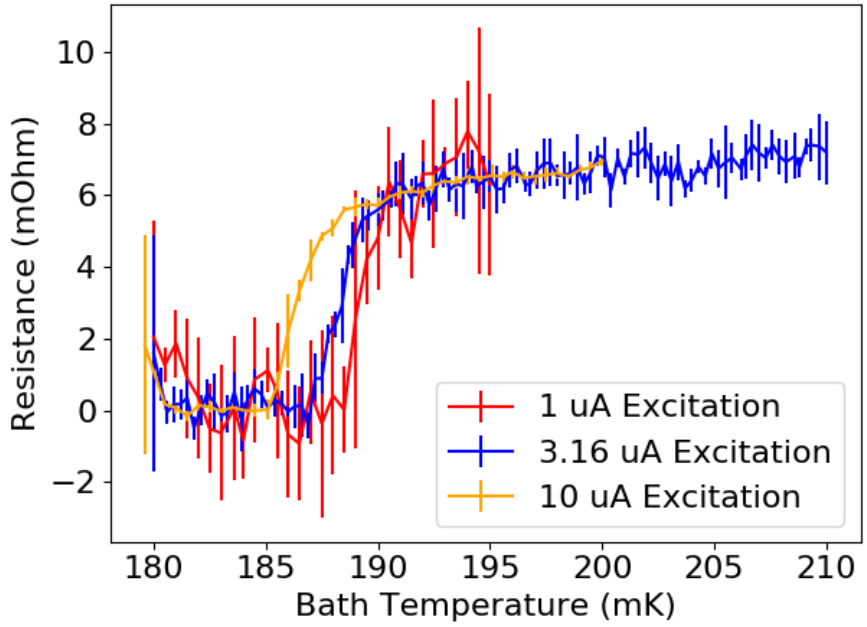

Figure 2.4: Four-lead resistance versus temperature measurement of a NIST UHF v1 TES showing the superconducting transition. Statistical error bars are shown on each data point. Three excitation currents are shown. A larger excitation current reduces the size of the error bar, but artificially suppresses measured T_C, since a larger excitation current will exceed the superconducting critical current at a lower temperature. As excitation current decreases, measured T_C approaches the zero current limit.

tion of temperature. An example of this kind of data is shown in Fig. 2.4. An example of T_C and R_N measurements as a function of TES geometry is shown in Fig. 2.6.

2.5 IV Measurements

IV data refers to current vs voltage curves for the TES devices under test as they cross the superconducting transition. Taking these curves is part of the standard

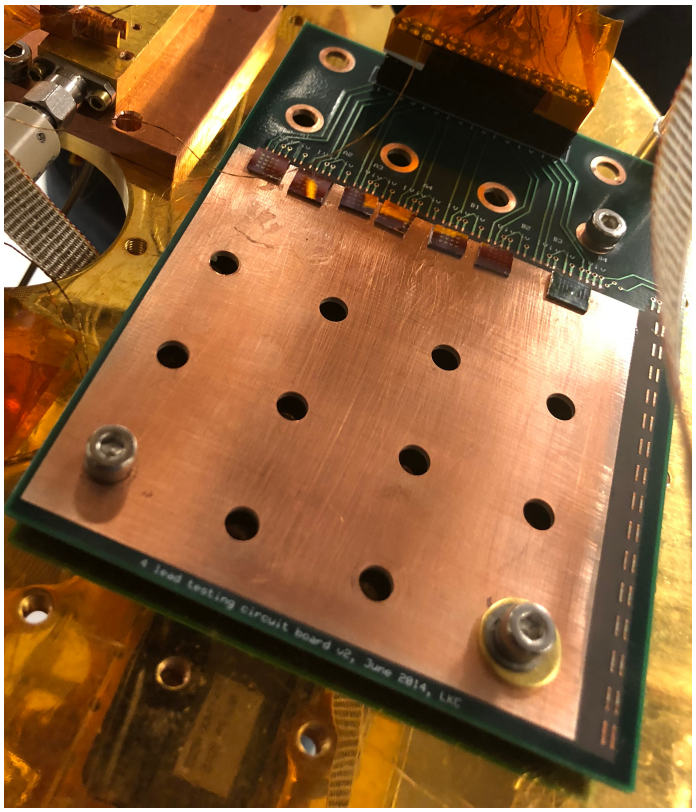

Figure 2.5: The four-lead resistance measurement PCB installed in the dilution refrigerator. Seven TES test chips from Berkeley are integrated. The custom connector and wiring at the top of the PCB routes the eight available channels into a Lakeshore 370 resistance bridge.

data acquisition protocol for telescopes in the field, so the MCE software is already equipped to take such cuves with ease and calculate several parameters based on these curves.

First, the dilution refrigerator is set to a fixed temperature. Then the TDM readout is tuned as described in Sec. 3.4. The SQ1 stage is servoed throughout the rest of the process. Then, each TES bias line is set to some large value to drive all of the TESes on that bias line normal. The voltage through the TES bias line is decreased to zero, which brings the TES through the superconducting transition. Meanwhile, the SQ1 servo records the current through the TES.

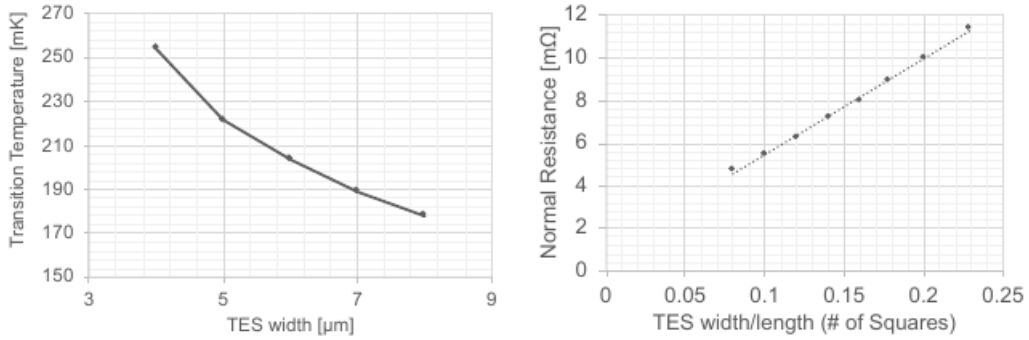

Figure 2.6: Measurements of TES bolometers manufactured by HYPRES/SeeQC demonstrating how T_C and R_N properties change as a function of the TES geometry. These data were acquired by IV measurement, but could just as easily have been acquired by 4-lead measurement. *Left*: TES T_C vs width, which changes due to the proximity effect of the Niobium leads. *Right*: TES R_N vs the TES width to length ratio. Plot originally published in [56].

This process is repeated at many different temperatures. Near the transition temperature, it is beneficial to record data somewhat finely; for example, with 1 mk steps. An example of this IV data for one detector is shown in Fig. 2.8. The resistance of the TES as a function of electrical power is also shown.

Notice that, in the IV curves, there is a very steep slope at low voltage bias, which corresponds to the superconducting portion of the curve. At higher voltage, there is a linear region with a shallower slope. This is the normal resistance portion of the curve. The superconducting transition is a region of negative slope. The negative slope happens because as the voltage drops across the transition, the resistance of the TES decreases quickly, diverting more current through the TES instead of the shunt resistor. Once the TES is completely superconducting, the resistance of the TES branch of the circuit is once again constant, so the current reduces in proportion to the voltage just as it did when the TES was resistive.

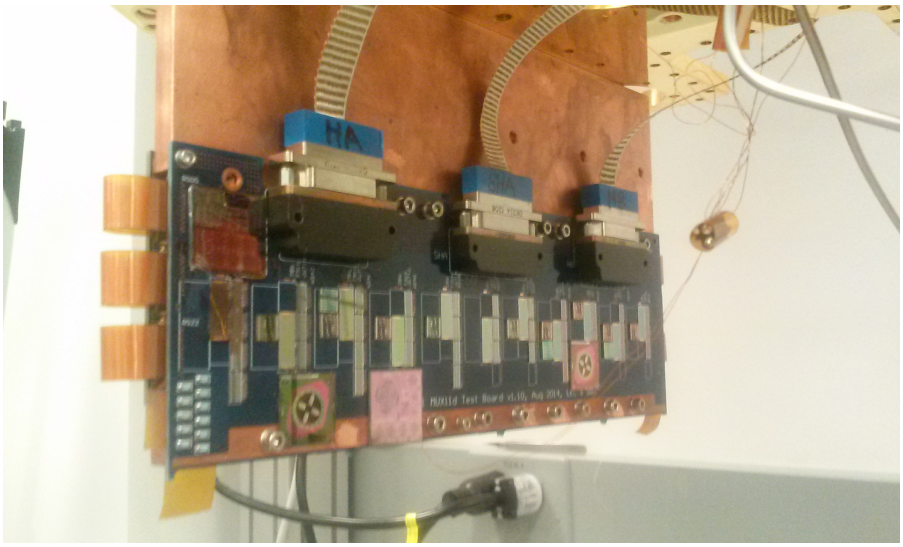

Figure 2.7: TDM test PCB, installed in the dilution refrigerator, with various TES test chips integrated. Compare with Fig. 3.4, when no TES test chips were installed. Typically, interface chips and TES test die or single pixels are integrated between the columns of mux chips. That is also true in this case, but here I also show larger, low frequency chips that are too big to fit between columns integrated beneath them instead.

Fig. 2.8 also has resistance vs power plots, calculated from the IV plot data. To calculate this, first the IV curve must be forced to intercept the point $(I, V) = (0, 0)$; it will have an arbitrary current offset due to the SQUID readout. Then the resistance is the ratio of the current and voltage, and the power is their product. Notice that, from the resistance vs power curve, it is easy to see both the normal resistance R_N of the TES (it is the horizontal region of the curve at high TES power) and the saturation power P_{sat} (it is the vertical region where the curve passes between zero resistance and R_N, which indicates the transition).

The normal resistance is consistent across all temperatures, as seen in the resistance vs power plot of Fig. 2.8. The average of all of these horizontal regions is taken to get a measurement of R_N from the IV data. This measurement of R_N can be compared with four lead resistance measurements to ensure consistency.

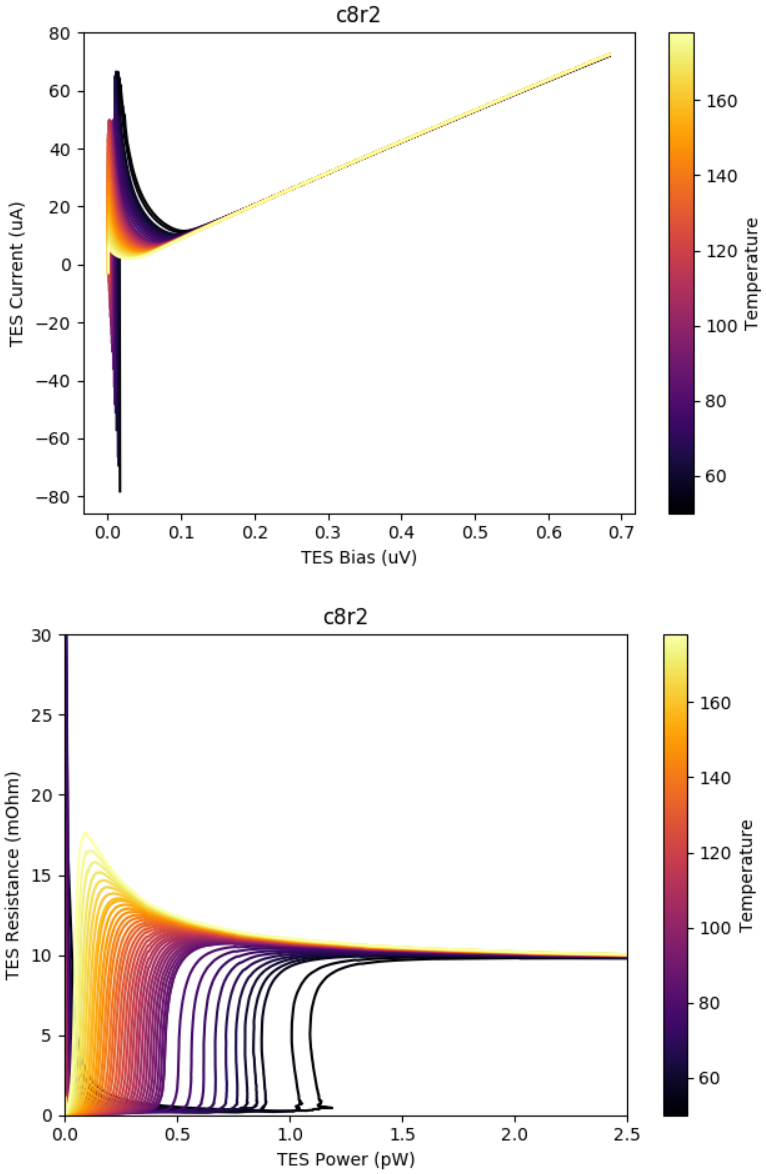

Figure 2.8: TES IV data for a HYPRES/SeeQC long leg TES across many temperatures. Top: IV. The linear portion that takes up most of the X range is the bias at which the TES is in the normal state; the critical current has been exceeded. The very steep slope at low currents is the superconducting region. The region of negative slope is the superconducting transition. Bottom: TES resistance vs power for the same data set. From this plot, it's easy to extract both the normal resistance (the horizontal portion of the curve) and the saturation power (the vertical portion of the curve).

Since these data are taken at many temperatures, P_{sat} can be extracted from the IV data and plotted as a function of bath temperature. These data are then fit to Eqn. 2.2. In this fit, T_C and k are allowed to float, but n is assumed to be some value, and then fixed. This is because k and n are highly degenerate; that is, by changing one of the two, a corresponding change in the other will result in nearly the same χ^2 during standard fitting algorithms. The result of trying to fit for both k and n simultaneously is fitted parameters that vary wildly and are inconsistent across data sets.

The value of n is assumed to be the target value for the fit, usually. If this value is incorrect, the curvature of the data will not match the curvature of the fit, which can be seen by eye. If a measurement of n is desired, then n can still be fixed during the fit, and the fit can be made for a range of values of n independently. The χ^2 is calculated for each n, and the fit is chosen that uses the value of n that minimizes χ^2. This method removes some of the chaos of fitting multiple degenerate parameters simultaneously at the cost of additional computation time.

These fits allow extraction of T_C, P_{sat} at 100 mK, and G (since it is calculable from T_C and k). Since IV data allows extraction of four (when R_N is included) useful parameters, it is one of the most important data sets that can be taken during characterization of the TES. An example of some of these fits for a number of devices can be seen in Fig. 2.9.

Fig. 2.9 also demonstrates how detector characterization can directly inform fabrication of the next iteration of devices. Each of these devices from Berkeley are identical except for the length of the four legs connecting the TES bolometer island to the thermal bath. The saturation power at 100 mK is proportional to

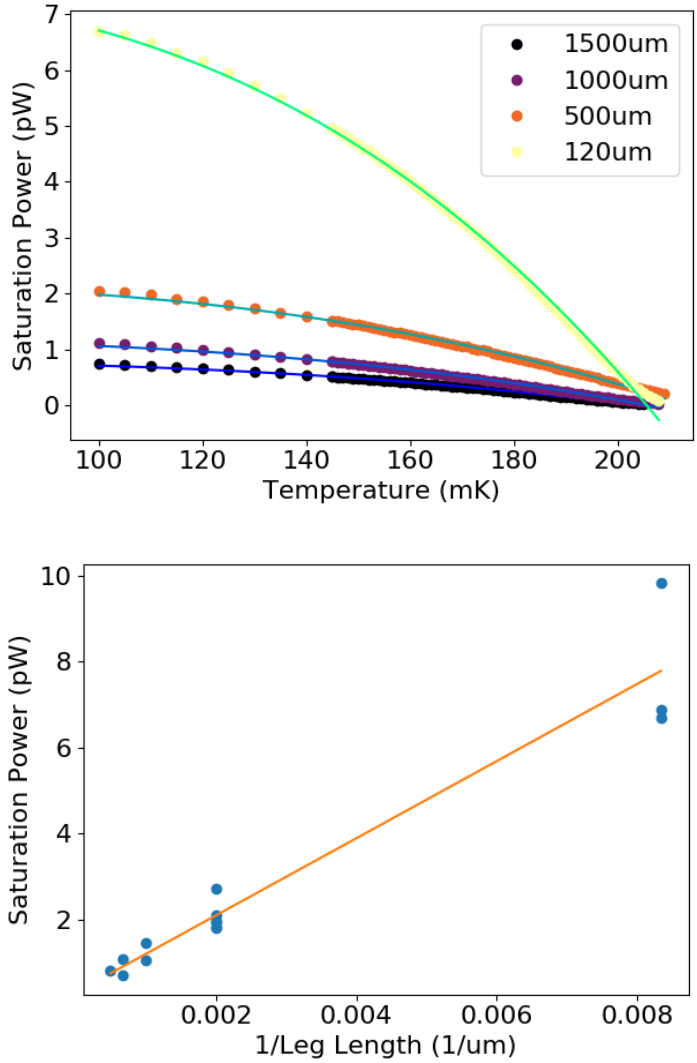

Figure 2.9: Top: Example fits of P_{sat} vs temperature data. This is for set of Berkeley TES devices with varying leg lengths. This is a fit to Eqn. 2.2, and allows extraction of G and T_C. Bottom: P_{sat} vs inverse leg length for the same Berkeley devices. Here, multiple examples of each leg length are shown. P_{sat} scales as the TES leg cross sectional area over the leg length, but each of these devices has the same cross sectional area. Both top and bottom were previously published in [56]

the cross sectional area of the legs (A) divided by the length of the legs (l), since it depends on G which is determined by the leg geometry. Fitting P_{sat} vs A/l allows the P_{sat} to be precisely tuned for a given TES design by altering the leg geometry in a known way.

2.6 Bias Step Measurements

The thermal time constant of the detector $\tau \equiv C/G$ is, in the case of the Simons Observatory detectors, much longer than the electrical time constant. It is long enough that it can be well resolved by the sampling rate of the MCE. By combining the measurement of τ with a known G (obtained from the IV measurements), the heat capacity C can be calculated. This heat capacity can then be adjusted in fabrication by adding or removing thermal mass from the TES bolometer island in order to speed up or slow down the time constant and match it with the optimal rate for data acquisition.

In the field, τ mostly measures the response of the detector to a change in input power P_γ; however, *any* change in P_{TES} from Eqn. 2.1 will result in an equivalent change. Therefore, at constant bath temperature for dark detectors in the laboratory, we simulated a P_γ signal by modulating P_{el}, the electrical bias power of the TES.

Stepping the TES bias voltage by a small amount provides a sharp, distinctive change in input signal. An exponential function can be fit to the SQ1 feedback signal to yield the effective thermal time constant. In practice, the first few samples of this must be discarded, because they will also be modulated by the electrical time constant. The electrical time constant can't also be extracted in

this case, because it is usually too fast to provide enough samples for a good fit. Since the voltage step is small, the TES stays approximately at the same point on the superconducting transition. Feeding a square wave into the TES bias line provides multiple steps that can be averaged, and provides both an upward and downward stepping measurement.

The effective thermal time constant, τ_{eff}, is extracted from this measurement; τ_{eff} is the effective thermal time constant under negative electrothermal feedback. The detector response is often expressed in terms of $f_{3\text{dB}}$ instead of τ, defined as

$$f_{3\text{dB}} \equiv \frac{1}{2\pi\tau_{\text{eff}}} \tag{2.4}$$

The quantity $f_{3\text{dB}}$ can be fit well to the model

$$f_{3\text{dB}} = A + BP_{\text{bias}}^{\frac{2}{3}} \tag{2.5}$$

where A and B are the fit parameters. The natural thermal time constant $\tau \equiv C/G$ is extrapolated from this fit by setting $P_{\text{bias}} = 0$ to remove the effects of the negative electrothermal feedback.

The bias step measurements require the TES to behave well, so only a mature detector technology can be accurately measured this way. Therefore, only the NIST UHF detectors underwent bias step measurements.

2.7 Noise Measurements

If a detector functions well enough to take data, then noise spectra can be acquired. With the temperature fixed, the dilution refrigerator's heater was set to

constant power mode (which is atypical; usually it is servoed with a thermometer) and allowed to equilibrate in order to minimize thermal drift in the data. The TDM was tuned and an IV acquired in order to prepare the detectors for data acquisition. The detectors were biased to a specific fraction of their normal resistance. Then, data were sampled from the detector at 3200 Hz for one minute.

The detectors were not exposed to light, so if they are also held at constant temperature in thermal equilibrium with the bath, and pickup from external sources is negligible, then the data stream from the detector should be noise from the detector and readout system. The detector noise can be demonstrated to be much greater than the readout noise by comparing noise spectra of channels with detectors to channels with no detectors. Since the spectra are dominated by detector noise, the use of the TDM readout system to acquire noise data is justified, even though the Simons Observatory will use the μ-MUX architecture.

Data streams are acquired for each detector at many different fractions of normal resistance. Then, a sixth degree polynomial fit is subtracted from each data stream to remove any remaining thermal drift. This polynomial subtraction will only affect the noise spectrum in the $1/f$ regime. If the detector is appropriately biased on the transition, then the noise should be approximately constant when the frequency is of order 10 Hz to 100 Hz. Much below this, $1/f$ noise dominates. Above this, the data begin to be affected by the high frequency roll off from the low-pass filtering of the TES circuit's L. In some cases, extra inductance can be added to the circuit intentionally to reduce aliasing noise.

A TES noise spectrum within the 10-100 Hz range should be comparable

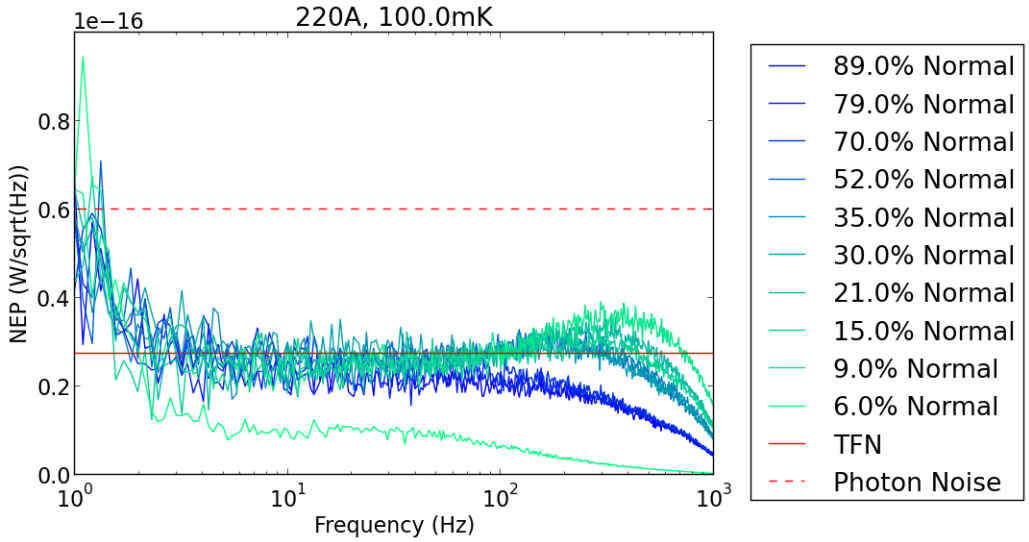

Figure 2.10: Noise measurements for one NIST UHF-1 v2 TES at various percentages of normal resistance, at 100 mK. The data were sampled at 3200 Hz. A DC approximation of thermal fluctuation noise (TFN) is shown (solid red line) and is consistent with the measured noise level between a few to 100 Hz. The photon noise level for UHF-1 on the SAT is expected to be greater than 60 aW/Hz$^{1/2}$ (dashed red line) [5]. The fact that the measured dark detector noise is significantly less than the expected photon noise suggests that these detectors will be photon-noise limited when deployed. Figure and caption originally published in [56].

with the thermal fluctuation noise from [36]:

$$P_{\mathrm{TFN}} = \sqrt{4k_b T^2 G F_{\mathrm{link}}} \tag{2.6}$$

where k_b is Boltzmann's constant, and F_{link} is an order 1 factor. I assume $F_{\mathrm{link}} = 1$ in all calculations. It is typically between 0.5 and 1 [36], so this estimate may be slightly high.

2.8 Results

The devices tested were fabricated at NIST, Berkeley, and HYPRES/SeeQC corporation. The Berkeley and SeeQC chips share a common design, though they were fabricated at different facilities. The NIST devices do not share a design with the others. This is partly due to the design heritage of the devices - NIST has previously fabricated bolometers for ACT, while Berkeley has fabricated devices for POLARBEAR. However, design standardization was not possible due to the different approaches each facility uses to thermally isolate the bolometer island. NIST uses deep reactive ion etching, while Berkeley and HYPRES/SeeQC use Xenon diflouride etching.

The target T_C and R_N for Simons Observatory devices are both well below that of previous detectors fabricated at Berkeley. Therefore, the Berkeley and HYPRES/SeeQC devices are less mature and have so far only been subject to four-lead resistance and IV measurements. The NIST devices have undergone all four types of described tests: four-lead, IV, bias step, and noise. NIST has fabricated exclusively ultra-high frequency (UHF) devices for the Simons Observatory, although NIST does have experience fabricating similar, lower frequency detectors for ACT. The Berkeley design will be used for low-frequency (LF) devices, pending successful tests.

Target parameters for P_{sat} and τ are listed in Tab. 2.1. Results from IV measurement of NIST UHF detectors are summarized in Tab. 2.2. The T_C and R_N results from the four lead resistance measurements were consistent with the IV measurements and so are not explcitly listed here.

Results from bias step measurements of the NIST UHF detectors are shown

Frequency	Parameter	Target	Variation
MF-1 (93 GHz)	P_{sat}(100mK)	4 pW	3-5 pW
	τ_{eff}	0.61ms	0.37-1.1 ms
MF-2 (145 Ghz)	P_{sat}(100mK)	6.3 pW	4.7 - 7.9 pW
	τ_{eff}	0.53 ms	0.32-0.96 ms
UHF-1 (225 GHz)	P_{sat}(100mK)	16 pW	12-19 pW
	τ_{eff}	0.36 ms	0.2-0.65 ms
UHF-2 (285 GHz)	P_{sat}(100mK)	24 pW	18-31 pW
	τ_{eff}	0.31 ms	0.18-0.57 ms
All	T_C	160 mK	
	R_N	8 mΩ	

Table 2.1: Current SO targets for some of the measured parameters in various bands. P_{sat} targets, are chosen based on loading estimation for bands; noise targets are motivated by sensitivity requirements; τ_{eff} targets are motivated by the expected rate of change of the TES input signal. T_C was chosen for use in dilution refrigerator systems. R_N was chosen to match with the microwave readout system described in [45]. We have omitted the low frequency (LF) bands as their target parameters have not been sufficiently determined as of this writing. Table and caption modified from original table published in [56]

Parameter	Target	Measured, v1	Measured, v2
T_c	160 mK	186 mK	166 mK
P_{sat} 225 GHz	12-19 pW	26 pW	18 pW
P_{sat} 285 GHz	18-31 pW	30 pW	24 pW
R_n 225 GHz	8 mΩ	7.1 mΩ	7.8 mΩ
R_n 285 GHz	8 mΩ	7.6 mΩ	7.9 mΩ

Table 2.2: Some measured parameters from NIST UHF detectors compared to their target ranges as gathered from IV analysis. P_{sat} values are listed for a bath temperature of 100mK. Measurements are presented for both v1 and v2 detectors. In each case, the v2 value is closer to the target. Table and caption originally published in [56]

in Fig. 2.11. The bias step measurements show that the thermal time constant has improved between v1 and v2 by removing some heat capacity from the bolometer island, but a v3 detector should speed up these detectors further. The IV measurement results show that T_C was slightly high in v1, which is the likely cause of a high P_{sat}. The T_C is much closer to target in v2, and thus, so is P_{sat}.

Fig. 2.10 shows an example of noise spectra. Data from a single detector are shown, at multiple fractions of normal resistance, at 100 mK. The thermal fluctuation noise from Eqn. 2.6 and the photon noise from [5] are also shown. These spectra were calculated for a large number of NIST UHF detectors for the Simons Observatory, and a histogram of these noise levels is visible in Fig. 2.12. The same detector may appear in the histogram multiple times, because each measurement (one combination of detector, bath temperature, and fraction of normal resistance) counts as a single datum in the histogram.

Some Berkeley IV results are shown in Fig. 2.8. R_N for these devices has been consistently nominal. The range of saturation powers explored are appropriate for MF or LF band detectors. Notice the P_{sat} vs T_{bath} plot shows that T_C for these detectors is slightly above 200 mK (each curve crosses the temperature axis here), which is significantly above the target. The HYPRES/SeeQC devices show a similar result.

Devices from all three facilities used AlMn sourced from ACI Alloys, Inc. Even so, the annealing process used to achieve target T_C varies between facilities due to the differences in device design and fabrication processes [56]. Berkeley is now attempting to produce AlMn in-house. Since these tests were performed, a number of device iterations have occurred that underwent four-lead resistance

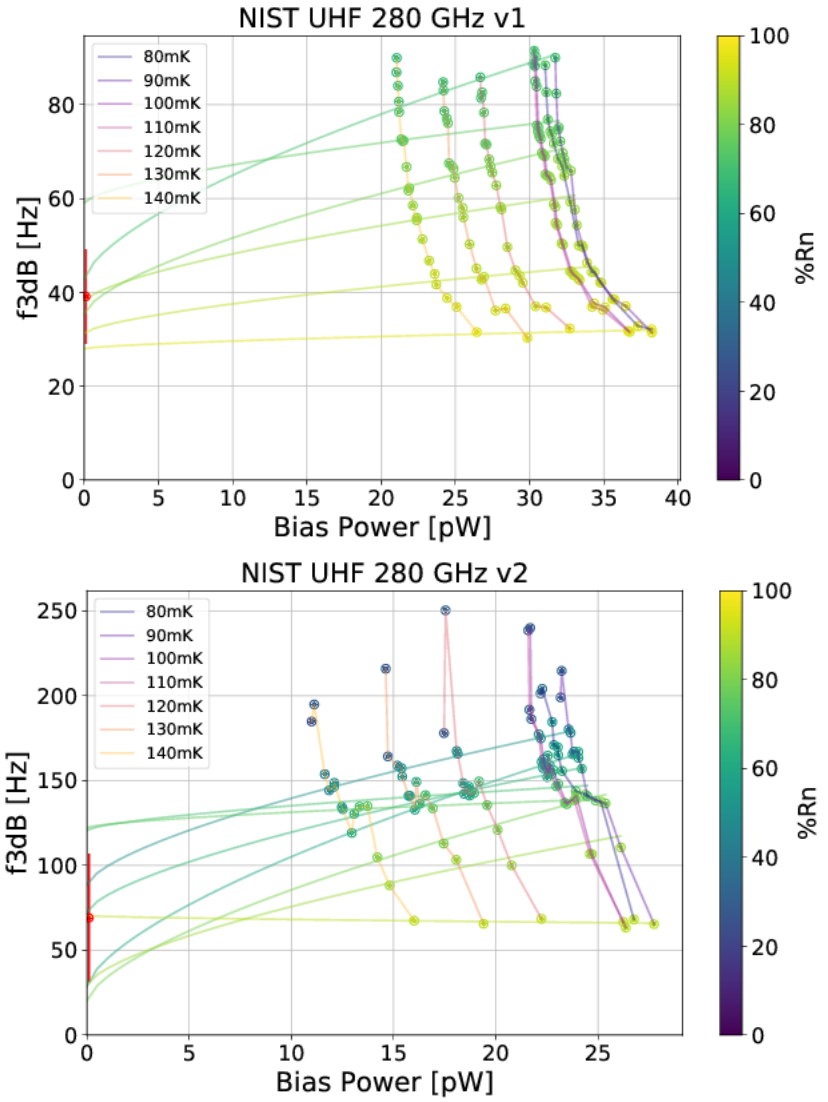

Figure 2.11: Measurements of f_{3dB} vs P_{bias} for two detectors. The top is a NIST UHF v1 detector, the bottom is a NIST UHF v2 detector. The v2 detectors had some heat capacity removed when the v1 detectors were measured to have a slow response compared to the target. The v2 detectors are still too slow, but are closer to nominal. The data are shown with fits to Eqn. 2.5. Figure is courtesy of Nicholas Cothard and was first published in [56].

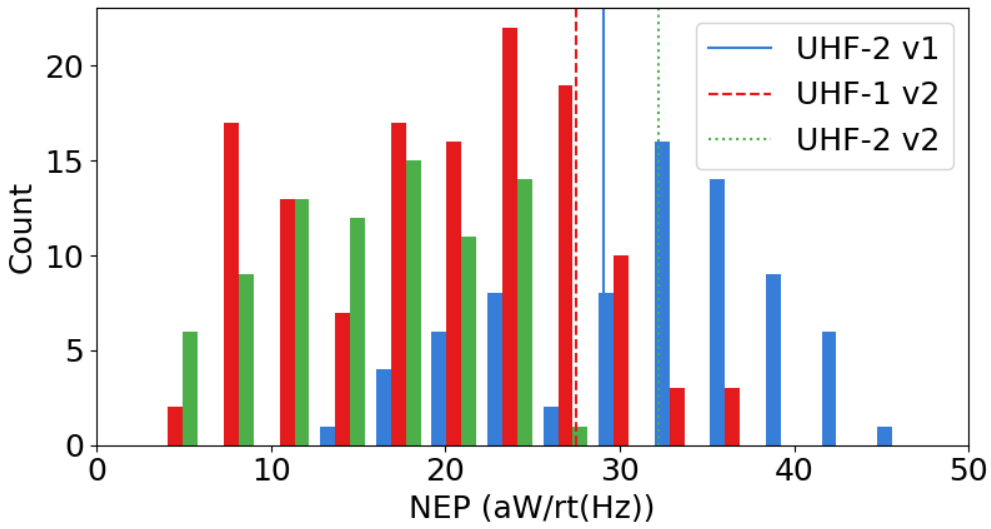

Figure 2.12: Histograms of measured NEP for NIST UHF detectors. In these histograms, each detector was measured at various temperatures and fractions of normal resistance, and each measurement counts as a point on the histogram. In total, there are six independent physical detectors measured. The thermal fluctuation noise (TFN) is estimated and plotted as a vertical line for each detector type. The measured noise levels cluster around (v1) or slightly below (v2) the TFN, suggesting it is the dominant noise source. The TFN is calculated by using the average measured G and T_C of the devices. The NEP of the detector is a fit of a constant function to the NEP spectrum in the range 10-100 Hz. The TFN calculation assumes $F_{\text{link}} = 1$, but F_{link} may be as small as 1/2 [36]. The UHF-1 v1 detectors were not measured. Figure and caption originally published in [56]

testing in order to push T_C towards the target, adjusting annealing temperature in order to tune T_C. This process is still underway, and the Simons Observatory collaboration hopes to soon have detectors from Berkeley and HYPRES/SeeQC that show nominal T_C.

These results demonstrate that this testing process has improved the design of transition edge sensors for the Simons Observatory. These detectors will soon

be within nominal design parameters.

CHAPTER 3

TIME DOMAIN SQUID MULTIPLEXERS

3.1 Introduction

Modern CMB telescopes have thousands of transition edge sensors, and measuring each detector with its own set of readout lines quickly becomes unfeasible for more than a few detectors. This is due not only to spatial design constraints, but also the need to decrease the thermal load on the cryogenic stages. Therefore, multiplexing of transition edge detectors is absolutely essential. There are currently several methods for performing multiplexing and readout of transition edge sensors. The most mature of these technologies, and the subject of this chapter, is time domain multiplexing (TDM). In particular, the Atacama Cosmology Telescope makes use of this style of readout and has achieved a multiplexing factor of 64 [30]; that is, 64 detectors are read out per channel. I will describe the specifics of the TDM readout used in in Advanced ACTPol and the testing procedure that was used to ensure quality of the cryogenic readout electronics.

3.2 Superconducting Quantum Interference Devices

The cryogenic portion of TDM circuits are based on superconducting quantum interference devices (SQUIDs); specifically, DC-SQUIDs. The electronic behavior of DC-SQUIDs is well documented; an overview of SQUID theory is available in [14] or [19]. DC-SQUIDs have the following basic characteristics that are

relevant to our discussion:

- A DC-SQUID is a superconducting ring with two Josephson junctions.
- It conducts electricity without any resistance below some critical current I_C^{min}.
- Above I_C^{min}, a voltage drop occurs across the SQUID. The critical current is a periodic function of the magnetic flux Φ threading the area of the SQUID, with periodicity equal to a single magnetic flux quantum (Φ_0). This makes the SQUID an extremely sensitive magnetometer.
- There are minimum and maximum critical currents, I_C^{min} and I_C^{max} respectively. If a current between these is applied, $I_C^{min} < I < I_C^{max}$, and we measure the voltage as a function of flux, there is range of flux for which the SQUID is superconducting (zero voltage drop). Above I_C^{max}, no such superconducting branch exists.

Much of this behavior is illustrated in Fig. 3.1. In the context of TDM, inductors are used to couple magnetic flux into a SQUID, thus modulating the SQUID voltage according to the current through the inductor. SQUIDs play essentially two roles in these circuits. First, they are used as ammeters. To measure the current through a line, inductively couple it to a SQUID or an array of SQUIDs. Second, they are used as flux-activated switches (FAS) by taking advantage of the fact that they can be made either superconducting or resistive depending on current through a coupled inductor (by biasing the SQUID between I_C^{min} and I_C^{max}).

Since the SQUID response to magnetic flux is periodic, it is necessarily nonlinear; in fact, it is approximately sinusoidal. In order to correctly infer the cur-

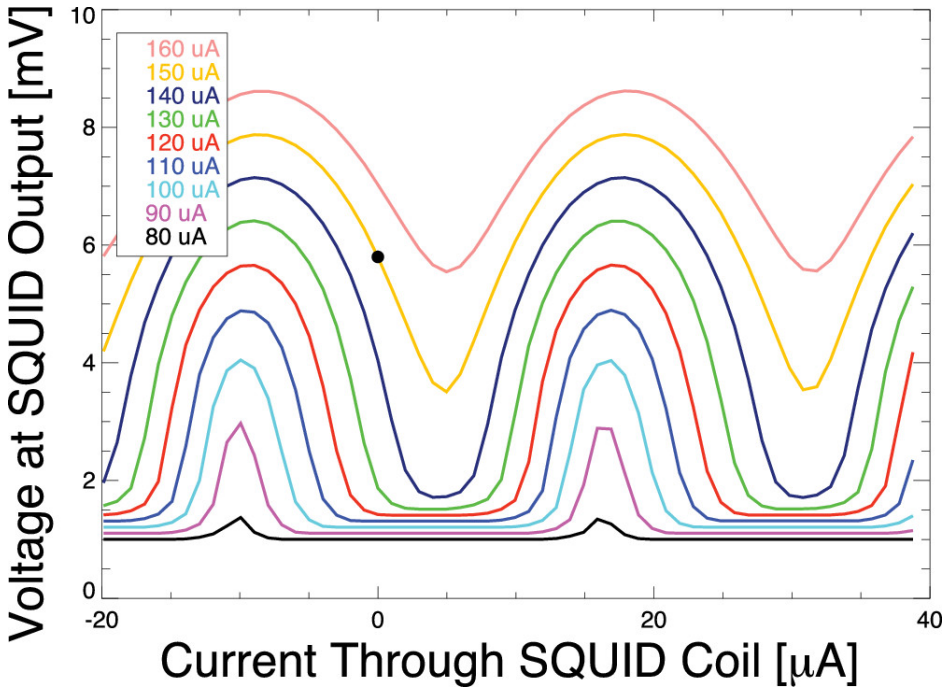

Figure 3.1: SQUID voltage vs magnetic flux (V-Φ curve) at multiple applied SQUID bias currents. The x-axis is input current applied to an inductor coupled to the SQUID, and is proportional to magnetic flux. As the applied bias current increases, the superconducting portion of the curve shrinks until it disappears entirely. Figure is from [23].

rent through the coupled inductor and use the SQUID as an ammeter, it is necessary to somehow linearize the SQUID response. In TDM, this is accomplished by "servoing" [10]. In addition to the SQUID's input coil inductor, a second feedback coil is inductively coupled into the SQUID and directly connected to the warm electronics. The purpose of this feedback line is to cancel any changes in magnetic flux through the SQUID from the input coil, and thus keep magnetic flux constant. By doing this, the SQUID can be kept at a single point on the V-Φ curve (the position with the steepest slope is usually chosen), called the lock point. The amount of current in the feedback coil becomes the measured signal. Note that if the feedback required extends beyond the dynamic range

of the DAC, then changing feedback by one flux quantum moves the SQUID to another V-Φ period. This can put the DAC back in range.

3.3 TDM Architecture

The time-domain multiplexing architecture is largely described in [10], but has been developed since. The second stage SQUIDs (SQ2) mentioned in that text have been eliminated completely, as described in [25]. Also, the software and firmware has been modified to increase the multiplexing factor from 33 to 64 [30] by repurposing some of the SQ2 bias lines as additional row select lines. This did not require a hardware change in the room temperature electronics.

A schematic of the cryogenic portion of the TDM circuit used in this work can be seen in Fig. 3.2. The portion labeled "SSA" (SQUID Series Array) is a SQUID servo that reads the current through the SQUID bias line (SQ1B). On SQ1B, there are a number of SQUIDs (these SQUIDs are called "SQ1") that are servoed by the SQ1FB (SQ1 Feedback) line to read current to their input. This input is connected to a TES, so the SQ1 acts as an ammeter to read the current through a single TES. Many SQ1s share a single bias and feedback line. Each SQ1 is in parallel with an FAS, normally kept in the superconducting state, to keep it from being biased. Current passing through the row select coupled to an FAS will turn it on and create a voltage drop, driving current to that FAS's SQ1 and biasing it on. Each FAS and each SQ1 actually represent 33 SQUIDs in series, acting effectively as a single unit.

The object described so far, and depicted in Fig. 3.2, is called a "column." There are multiple columns; 32 in AdvACT. The row selects for each column

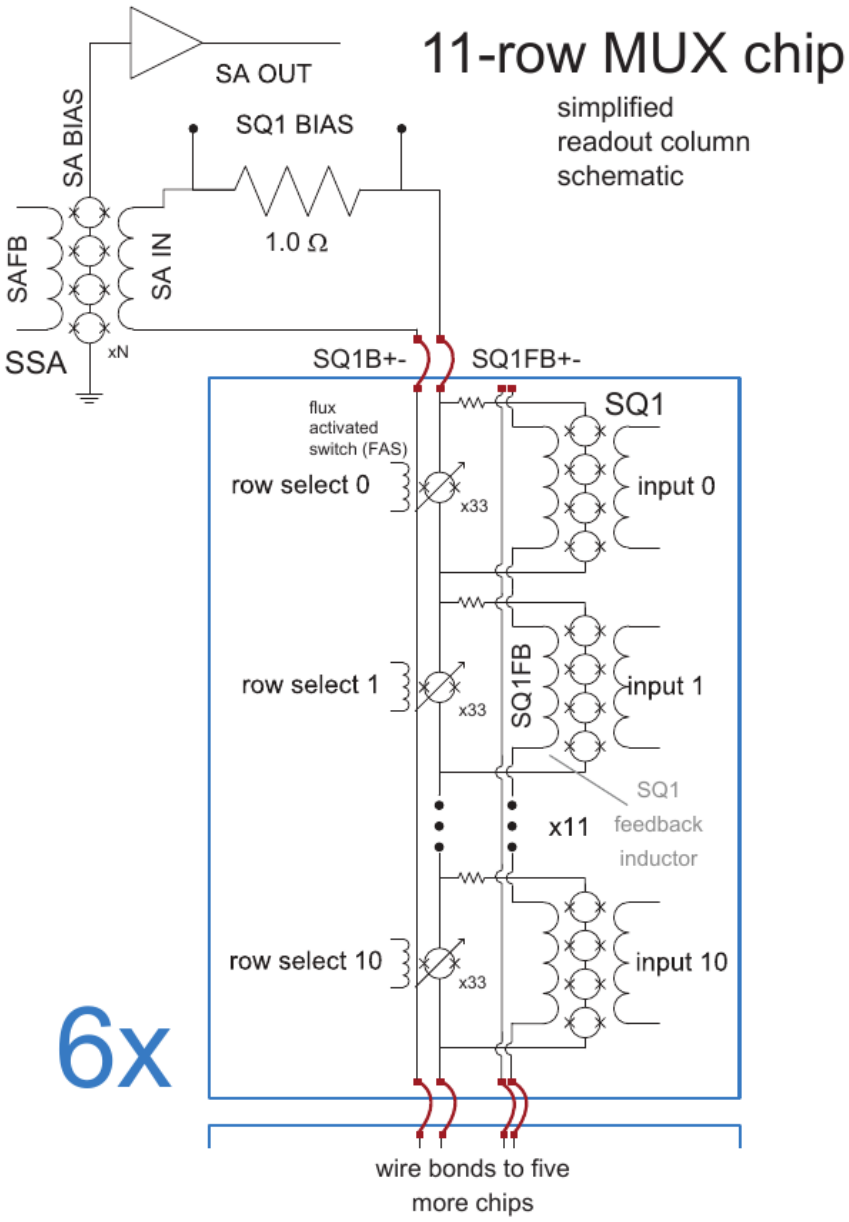

Figure 3.2: Schematic of the TDM architecture. Variants of this figure from NIST are common in TDM literature but this particular figure is from [30]. The blue box contains the elements of a single TDM mux chip. In AdvACT, six of these are chained in series on a column to achieve 64 row multiplexing. SQ1B and SQ1FB lines are electrically closed by wire bonds at the end of the column. The part of the schematic outside of the blue box represents the series array circuit at 1 K. There is one series array circuit per column. See the text in 3.3 for a detailed description of the circuit.

are connected in series. One row of each column is read out at a time, and all columns are read out simultaneously. The room temperature readout electronics, which control the SA Bias, SAFB, SQ1B, SQ1FB, and row select lines, turn on and read out each row in succession in order to read out all TESes on the array. Note that this requires six wires per column and two per row, counting both signal and return. The number of wires required for readout therefore scales as the number of rows times the number of columns. Roughly speaking, the number of detectors that can be read out goes as the square of the number of wires.

The portion in the blue box in Fig. 3.2 represents a mux chip. Several of these can be chained together on a single column. Each is capable of reading out 11 channels. There have been several design variations of these over the years. The first chips tested for Advanced ACTPol had the "MUX13C" designation (third design from 2013). Soon after testing began, a "MUX15B" design was adopted (second design from 2015). The MUX13C chips that were tested were not deployed, in order to maintain hardware consistency across the array.

A multi-channel electronics (MCE) crate constitutes the room temperature portion of the TDM readout system and acts as an electronic hardware interface between the data acquisition computer and the cryogenic superconducting electronics. The MCE system was developed at the University of British Columbia, and originally deployed on SCUBA-2 [34]. Advanced ACTPol uses one MCE crate per detector array [30] for total of three, but in the TES and multiplexing test apparatus at Cornell, only one MCE crate is necessary.

3.4 Tuning

In order for the warm readout electronics to set each line to its proper DAC value to read out a TES, the V-Φ response of each SQUID in the circuit must be known. The process of measuring these curves is called "tuning" and requires several specific steps. Some of these steps are represented in Fig. 3.3. The tuning procedure is described in [9]. The steps of tuning the readout, in order, are:

1. `ssa`. The V-Φ of the series array SQUID is obtained by ramping current through the SAFB line. This determines the appropriate current to apply to SAFB to keep ther series array SQUID locked to the appropriate position on V-Φ. This is the top plot in Fig. 3.3.
2. `rs_servo`. The series array SQUID is servoed to read out current on SQ1B. Notice that the current measured by the series array servo is only the current that passes through the branch of the circuit entering the multiplexing chips and excludes current shunted through the parallel 1 Ω resistor. Current is ramped through each row select line, one at a time. As the voltage across the FAS changes, the current measured by the series array changes. This results in an `rs_servo` curve that can be used to determine the appropriate current to apply to each row select in order to turn the row on or off. This is the center plot in Fig. 3.3.
3. `sq1servo_sa`. The series array SQUID remains locked. Each row is turned on one by one. While a given row is on, current is ramped through SQ1FB. The current read on the SQ1B line by the series array is modulated by the SQ1 SQUID. This results in a measurement of the SQ1 V-Φ and is used to determine the lock point for the SQ1 so that it can also be used as a servo. This is the bottom plot in Fig. 3.3.

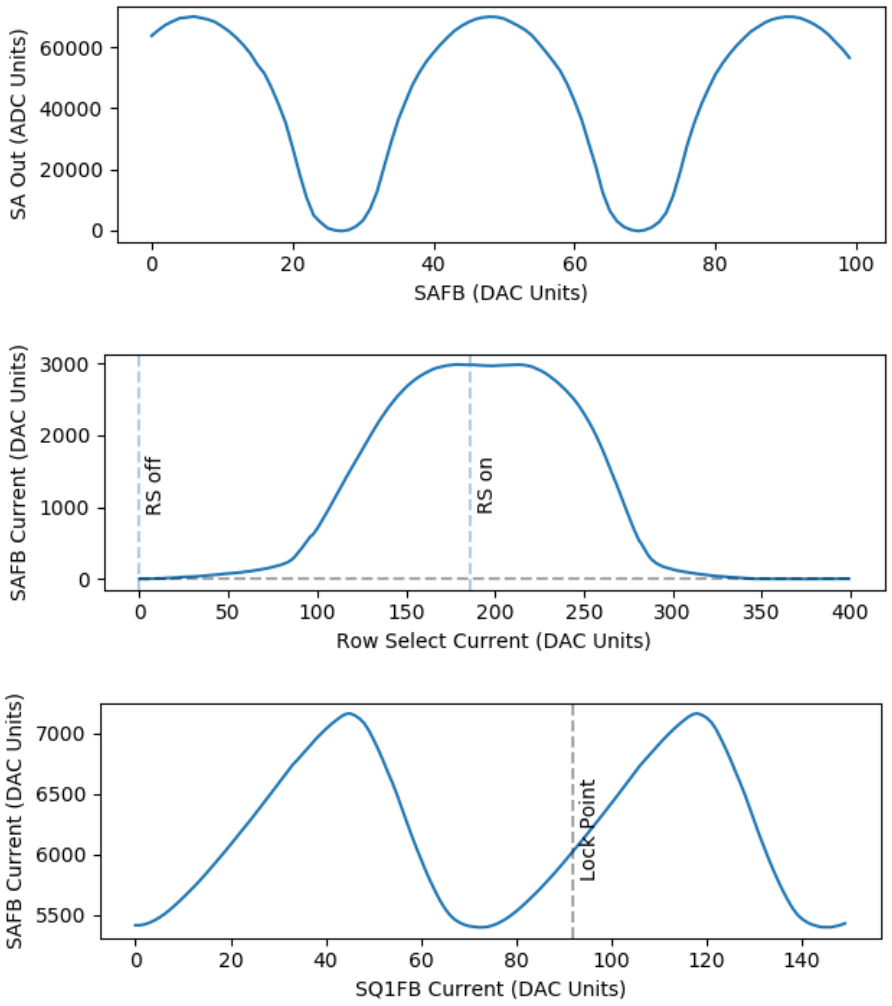

Figure 3.3: Some sample plots from tuning. Top: ssa. Middle: `rs_servo`. Bottom: `sq1servo_sa`. These three plots indicate a fully functioning multiplexing channel. On the `rs_servo` plot, "RS off" and "RS on" indicate the flux values chosen to turn the FAS off and on, respectively. A horizontal line has been drawn at SAFB=0; values near this point represent the superconducting branch of the FAS. On the `sq1servo_sa` plot, the lock point has been indicated.

4. `sq1_ramp`. This is the same as `sq1servo_sa` except that the series array is *unlocked*; that is, SA OUT is measured without changing current through SAFB while current is ramped through SQ1FB as each row is successively turned on. In practice, I have not used this information except as a sanity check to confirm `sq1servo_sa`.

5. `sq1ramptes`. Now the SQ1 servo is locked and current is ramped through each TES bias line. The current required on SQ1FB to keep SQ1 locked is the signal. If the TES circuit is connected to the SQ1 input coil and continuous, the data will show modulation of the SQ1 SQUID.

The `ssa` and `sq1servo_sa` are used to determine correct lock points for their respective SQUID feedback lines. The `rs_servo` determines the currents to apply to the row selects to turn each on and off. In addition to determining these values, each of these curves can be used to identify problems. Typically, if one stage of tuning fails, all stages after it will as well, and the failure point can be used to determine the part of the circuit that is causing a problem. Additionally, the `sq1ramptes` stage can be used to determine which channels are connected and continuous.

Note that one remaining variable is the amount of current that should be applied to SQ1B, since this is never determined in the tuning process. In practice, the amount of current to apply is hard-coded. The testing procedure in Sec. 3.5 determines the optimal bias level, chosen to be near I_C^{max}.

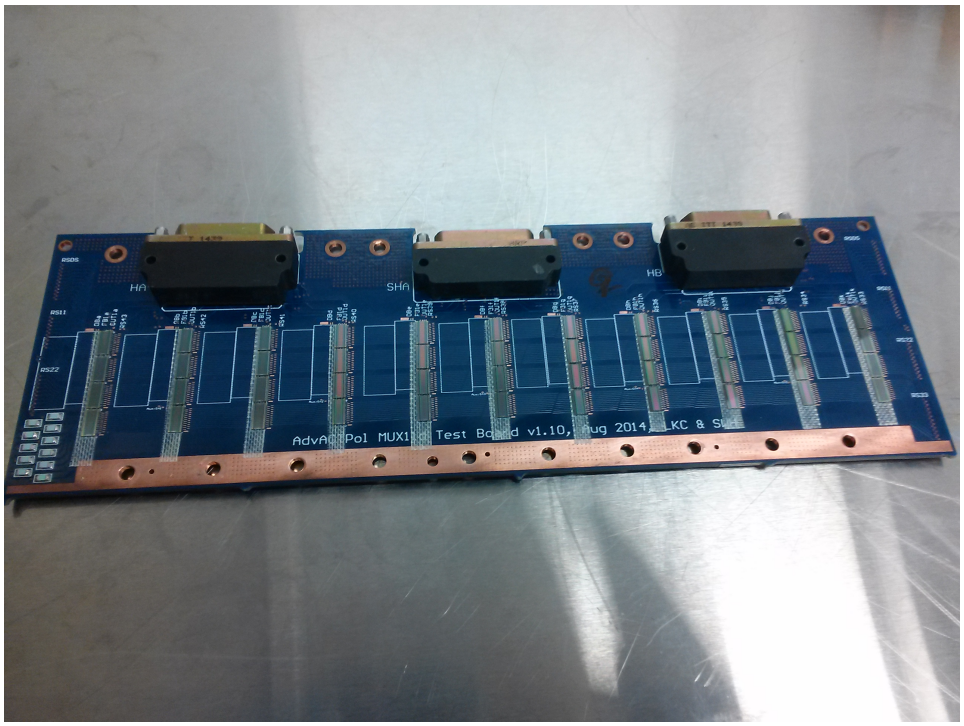

Figure 3.4: "Single pixel" test board designed for screening and characterization of AdvACT TES, mux, and interface chips. The board allows readout of up to 11 columns and 44 rows (4 mux chips per column). In this photograph, the board is being used to screen mux chips to determine if they may be deployed to the fielded array.

3.5 Multiplexer Chip Screening

For Advanced ACTPol, each multiplexer chip was screened at Cornell prior to being integrated in any deployed array. Chips that did not perform optimally were not selected for deployment. Among chips that were deployable, their properties were characterized in order to inform the multiplexing layout of the array. In total, over 1000 chips were characterized and about $\frac{2}{3}$ were approved for deployment. In this section, I describe the testing process for these chips.

The chips are integrated with a test PCB depicted in Fig. 3.4. This PCB is

probed for continuity, to show open lines or shorts between lines. The PCB is then put in a dilution refrigerator and cooled to 100 mK, the nominal operating temperature of the detector plane in the telescope.

Once the chips are cold, tuning data is taken and the tuning stages described in Sec. 3.4 are manually inspected for each channel. The initial tune sets the SQ1 bias value to a default (2000 DAC Units, or 29.7 μA) that works reasonably well for most channels. By inspecting the various curves from this initial tune, a large fraction of the undeployable chips are identified.

Next, full tuning data are taken varying the SQ1 bias from a value at or near zero to values well above I_C^{max}. From these data, I_C^{min} and I_C^{max} are extracted by finding the sudden change in slope of the curves in Fig. 3.6. An easy way to do this is to perform linear regression of SAFB current at low SQ1 bias current to get the superconducting branch, then subtract this regression line from the full curve to get an order parameter. Finally, the full tune data vs SQ1 bias can be used to make three dimensional plots like Fig. 3.5, which neatly summarizes the data set and allows quick diagnosis of some problems (See Sec. 3.6).

Finally, the full tuning data are taken again, but the flux activated switches remain off for the entire test by setting the "row select on" value seen in the row select curve of Fig. 3.3 to zero. The maximum SQ1 bias tested here may be might higher than in the previous set of tests in order to find the value of $I_{C,col}^{FAS}$. The purpose of this test is to check for "persistence," a failure mode described in Sec. 3.6. If persistence is discovered, and the offending channel is identified, then the chip is marked as unusable. It sometimes occurs that a chip develops persistence in the field, and in this case, this "FAS off" data might be used to work around the problem.

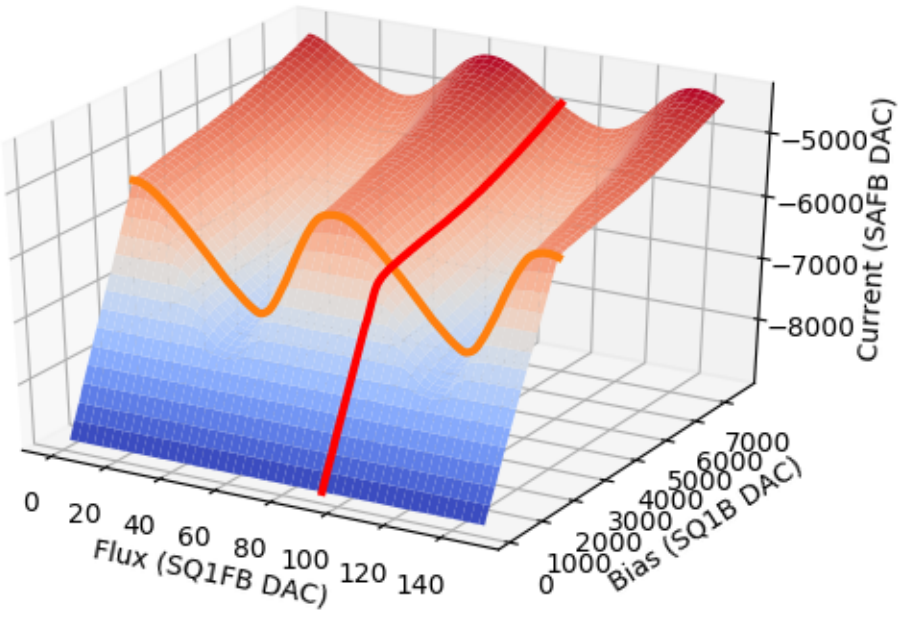

Figure 3.5: Three dimensional plot showing the current through the SQ1 bias line as a function of SQ1FB and SQ1B. Here, SQ1B is the the bias applied to the multiplexer circuit and parallel 1 Ω resistor. Since this is measured by the series array, it is in units of SAFB. The plot is inverted to make it easier to interpret, since SAFB decreases as SQ1 current increases. The green curve shows the SQ1 curve near I_C^{max}. The red curve has a constant flux equal to the lock point chosen by the MCE. This manifold is generated by collecting `sq1servo_sa` curves at many SQ1B points and treating them as cross-sections.

The test results are put into a database and later used to select chips for array deployment. The data collected are:

- Test logistics; specifically, the date of testing, test PCB number, date received, testing location, and chip identifying information.
- Whether or not the chip is deployable. If not, a reason is given. In some cases, a failure of another chip on the same row or column can cause the test to be inconclusive, in which case, the chip is marked to be retested.
- Which other chips were tested on the same row and column.

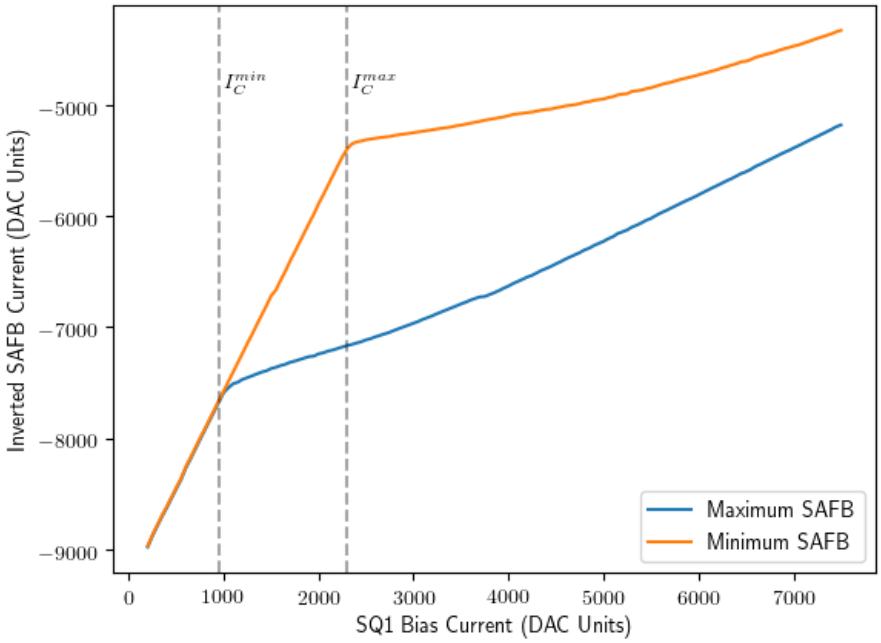

Figure 3.6: The minimum and maximum SAFB current to lock the series array servo while ramping SQ1FB as a function of SQ1 bias current. The y axis has been inverted, since SAFB decreases as current through the SQ1 increases. These data are a subset of the data presented in Fig. 3.5. Vertical lines have been drawn to show the SQ1 bias values of I_C^{min} and I_C^{max}. The linear portion of the curves at low SQ1 bias current show the superconducting branch of the SQUID. Above I_C^{min}, there is at least some portion of the SQ1 V-Φ that is not superconducting, and above I_C^{max}, there is no superconducting branch. It is easy to see from this example that the amplitude of the SQ1 curve is maximal near I_C^{max}.

- I_C^{min} for each channel
- I_C^{max} for each channel
- Row select "on" current for each channel. The "off" value is also collected but is typically near zero.

3.6 Failure Modes

In this section, I attempt to categorize failure modes witnessed during testing. Where applicable, I also identify causes and possible work-arounds.

- **Dead SQUID**. This will typically manifest as a single channel where one tuning stage shows only noise in SAFB or SQ1FB. Any tuning stage after the failed stage will also fail for this channel. This will identify the offending part of the circuit, but the chip is marked not deployable in any case. A bad `row_select` curve indicates a problem with the FAS, and a good `row_select` but bad `sq1_servosa` indicates a problem with the SQ1.
- **Open row select**. This problem is encountered in warm continuity checking of the test PCB. In fact, it can be *caused* by continuity checking of the test PCB if care is not taken regarding probe excitation currents and electrostatic discharge. An open row select on just one column will prevent the entire row from reading out, so it must be corrected before the test can continue. The chip is marked bad and the channel is removed by placing a wire bond that shorts the row select input on the offending column.
- **Trapped flux**. The superconducting loop that makes up a SQUID will trap lines of magnetic flux if they are passing through the SQUID when it transitions from the normal to the superconducting state. This causes a phase shift of the SQUID V-Φ curve. For a single SQUID, this is not a problem, but the series array, flux activated switch, and SQ1 SQUIDs are really arrays of 33 SQUIDs (as noted in Fig. 3.2). These SQUIDs typically act in unison as if they were effectively a single SQUID, but phase differences between them due to trapped flux can cause the V-Φ seen by the readout

electronics to take on strange shapes, and can render the channel useless. Fortunately, trapped flux can be remedied by warming the system above the superconducting critical temperature (9 K for our Niobium SQUIDs) and below it again, being careful not to introduce current or magnetic fields into the system. Sufficient magnetic shielding mitigates this problem greatly. Unfortunately the process of warming the array above T_C and cooling it again can be quite time consuming, especially in the field. We call this process "expelling trapped flux."

- **Unusual SQUID curves**. A `row_select` or `sq1servo_sa` curve looks qualitatively strange. A strange row select usually causes persistence, see below. A bad SQ1 might prevent adequate lock, introduce excessive noise into the system, or lead to unexpected behavior in the signal. These can be caused by trapped flux or they can be due to problems with the SQUID itself. If these are seen, an attempt at expelling trapped flux can be made. If this fails to solve the problem, the chip should be marked bad. The curves can look unusual in many different ways, and at many points in testing I saw curves that were unusual in ways I had not seen before, even after screening hundreds of chips. Since this failure mode is so unpredictable, it is most useful at this scale of manufacture to individually inspect every tuning stage for every channel by eye, rather than trying to automate a detection scheme. Many of the curves were unusual in their period (the amount of flux equal to 1 Φ_0), which may be related to the resistance of a feedback or row select line.

- **Persistence**. An FAS may fail to have a superconducting branch; in other words, $I_{C,col}^{FAS}$ is less than the SQ1 bias. This is often caused by the above problem, which may in turn be caused by trapped flux. However, some-

times it is a permanent feature of the channel. If this happens, the switch will permanently divert current to its channel's SQ1, and some of the signal from that SQ1 will bleed into every other channel on the column. This is tested for by tuning with all row select currents set to zero to turn them off. If `sq1servo_sa` curves are nonzero, there is persistence.

If the level of persistence is relatively low, decreasing the SQ1 bias current could create a superconducting branch in the FAS while still providing enough current to bias the SQ1 on. Specifically, this will work if $I_{C,col}^{FAS} > I_C^{min}$ for every channel on the column. However, larger values of $I_{C,col}^{FAS}$ compared to I_C^{min} are preferable. This provides a workaround for this problem in some cases, if necessary. In other cases, the superconducting branch of the FAS does not appear above I_C^{min}, rendering the column useless. If this error is seen during testing, and flux expulsion does not correct it, the chip is marked bad and all chips on the same column must be retested.

Because the nonzero `sq1servo_sa` curve appears on every channel within a column, it is not entirely straightforward to find the responsible channel. I know of two approaches, one of which usually works. First, an unusual `row_select` on a given channel usually indicates the channel causing the problem. In some cases, the `row_select` curves may all look fairly normal. If that is true, then the amplitude of the `sq1servo_sa` curve can be compared across the entire column. The amplitude of the channel causing persistence is often much higher than the other channels. Why? When two channels are on simultaneously (both the intended readout channel and the persistent channel), current is diverted to both SQ1s, causing excess voltage drop. If the persistent channel only is turned on, then there is not an extra voltage drop from the second channel, thus

increasing the current measured by the series array relative to the non-persistent channels.

- **Open input coil**. In this case, the input coil that couples the SQ1 SQUID to the TES is open. All tuning stages will appear normal until `sq1ramp_tes`. This problem affects only a single channel and was not explicitly tested for at Cornell, though it did appear in a small quantity of mux chips tested at Stanford.
- **Shorts**. A small number of chips were found to have shorts between two lines. In one case, this was between the SQ1FB and SQ1B lines, preventing readout of the entire column. In two other cases, this was a short between the SQ1B and row select. This failure prevents readout of both the affected column and the affected row! Therefore, although this problem was extremely uncommon, it had the potential to disable large numbers of channels. Fortunately, this problem can be probed for at room temperature. It did not suddenly appear later in chips due to handling or poor wire bonding, so the initial, pre-cooling continuity check is sufficient to completely eliminate this problem.

3.7 Testing Results and Chip Selection

Of the 1031 multiplexer chips tested for Advanced ACTPol, 614 were deemed deployable and 158 failed screening and thus were deemed undeployable. 184 required retesting for one reason or another, but were never retested since enough chips had become available to integrate all four arrays. The remaining 75 chips passed screening but were of the older "MUX13C" design, and

therefore not considered for deployment. Chips were undeployable for any of the reasons listed in the previous section, or too great a variance of I_C^{max}, or if $I_{C,col}^{FAS} < 2I_C^{max}$.

A nice cross check that both SQUID design and chip testing are well understood is to compare the ratio I_C^{min}/I_C^{max} to the parameter $\beta_L \equiv 2LI_0/\Phi_0$. Here, L is the SQUID loop inductance, which I assume to be the nominal design value 120 pH; I_0 is the josephson junction critical current, and Φ_0 is the magnetic flux quantum. See Fig. 3.7 for this comparison. The parameter β_L is calculated by solving the transcendental, steady-state equation

$$\delta_1 - \delta_2 = 2\pi\phi_a + \beta_L \frac{\pi}{2}(\sin\delta_2 - \sin\delta_1) \tag{3.1}$$

where ϕ_a is the applied magnetic flux and δ_1 and δ_2 are the phase differences across the SQUID's two Josephson junctions. The critical current in this equation is the point where, for a fixed β_L and ϕ_a, the value $|\sin\delta_1 + \sin\delta_2|$ is maximized; then I_C^{max} and I_C^{min} are the maximal and minimal critical currents obtained while varying ϕ_a. This equation comes from [14], and the results are in Fig. 3.7.

Since it is ideal to bias the SQ1 near I_C^{max}, deployable chips were sorted according to mean I_C^{max} across all rows. Note that every row on a given chip tended to have similar I_C^{max}, but chips with a total range of I_C^{max} greater than 25% were not deployed. In this sorted list, chips were grouped into columns of six for deployment. Some chips within the list were left out of any column, so that there were spare chips with various I_C^{max} to be used as replacements for any chips damaged in handling. The columns themselves were integrated in arbitrary positions on the array. Similar care was not taken with the row select values, since the row select on and off values were extremely consistent between all deployable chips (in fact, having an unusual `rs_servo` frequency would have flagged the chip

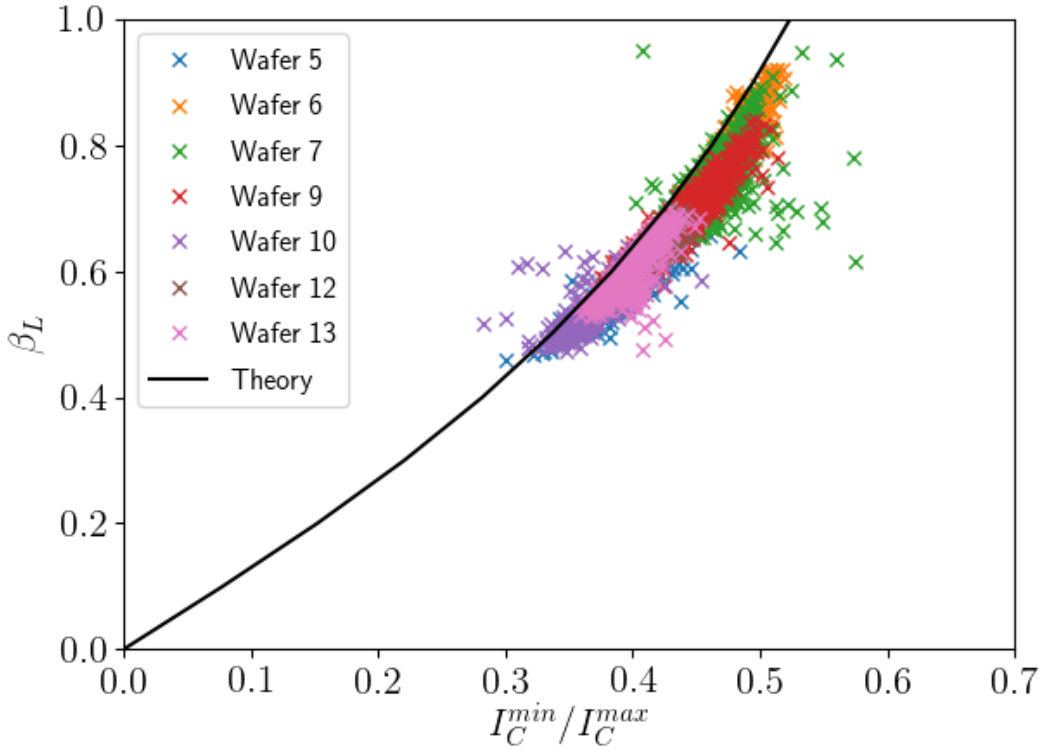

Figure 3.7: The parameter $\beta_L \equiv 2LI_0/\Phi_0$ vs I_C^{min}/I_C^{max} for MUX15B chips screened for Advanced ACTPol. Only chips that passed screening are shown, since measurements are not reliable for others. Data are organized by fabrication wafer. The theory-derived relationship between the two is also plotted with the data. This theory-derived curve is obtained by numerically solving a transcendental equation from [14].

undeployable, but deviations from typical values tended to be quite large).

On deployed arrays, despite mux chip screening, the primary cause of dead channels is still multiplexing. However, the detector yield on all deployed arrays is higher than the fraction of chips that passed screening, suggesting that the screening is effective at improving yield. More importantly, some of the more catastrophic failure modes, like shorts between SQ1B and row select, have been entirely eliminated. Some of the yield issues on deployed arrays are at-

Array	Frequency (GHz)	NET (μK $\sqrt{(s)}$)
HF	150	13
HF	230	26
MF1	90	12
MF1	150	14
MF2	90	11
MF2	150	12

Table 3.1: Sensitivity of deployed AdvACT arrays in units of μK $\sqrt{s}$. Sensitivity is at 1.3mm of precipital water vapor divided by the sine of the observing altitude [17].

tributable to trapped flux, while others may be the result of handling the chips during transportation, integration, and deployment.

The first AdvACT array to deploy was the high frequency (HF) array in 2016, depicted in Fig. 3.8. The readout on this array was more complex than the others due to the enormous number of channels - 2024 total detectors across 503 on-sky pixels. The detector yield of this array upon deployment was 70% [33]. Improvements in wire bonding and integration techniques improved yield in later arrays. The next two arrays deployed were both mid-frequency (MF), with 1716 detectors across 429 pixels on each array. The first array, MF1, had an 88% detector yield. The second, MF2, had only a 76% yield, because it had one persistent column that could not be repaired by underbiasing [16]. Finally, the low frequency (LF) array is being deployed as I write this, but laboratory tests showed over 90% detector yield. It has 390 detectors spread across 73 pixels [42]. Sensitivities of the deployed arrays are listed in Tab. 3.1.

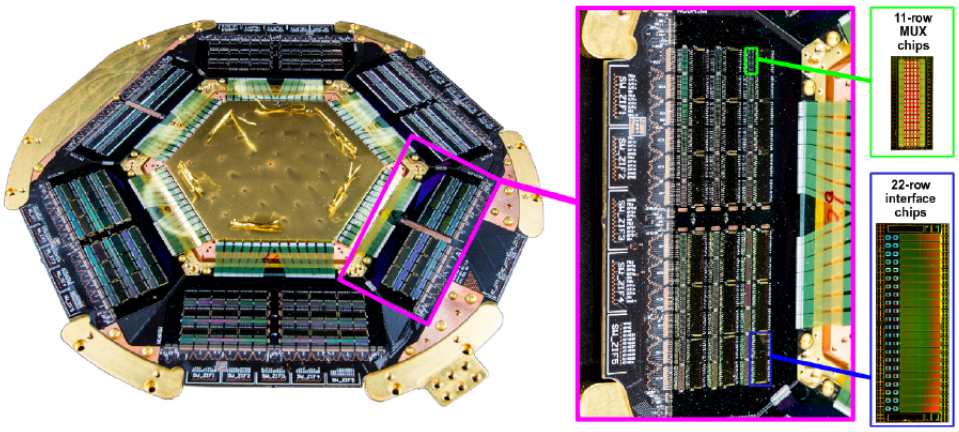

Figure 3.8: Back side of the Advanced ACTPol high frequency (HF) array. Image from [30]. The hexagonal detector array is seen in the center, connected by flexible cabling to the readout electronics PCB that surrounds it. The close-up shows the multiplexing and interface chips, which themselves are mounted on silicon wiring chips that are in turn mounted to the PCB. Wire bonds connect the PCB to the wiring chip and the wiring chip to the mux and interface chips.

CHAPTER 4

RESONATOR MULTIPLEXING

4.1 Introduction

Recently, readout methods that use high frequency resonators to multiplex detector signals have become popular. These methods are less mature than the time-domain multiplexing technology, but they have the potential to achieve multiplexing factors of order 1000.

Kinetic inductance detectors (KIDs) are naturally multiplexed this way, and are relatively simple to read out [46]. They are also relatively easy to fabricate. In a KID, a microwave tone passes through a strip of superconducting material that acts as the detector; this is in series with a capacitance to form a resonator. Photons that strike the superconductor break cooper pairs, changing the superconductor's inductance. The shift in resonator frequency is dependent on the photon power, so it is interpreted as a signal. KIDs are still a relatively new technology, though, and less mature than transition edge sensors.

Transition edge sensors can be multiplexed with a similar, although slightly more complicated, scheme. This scheme, called microwave multiplexing (μ-MUX) will be described in Sec. 4.2. At Cornell, I developed a system for measuring microwave resonators and used it to test μ-MUX chips fabricated at NIST. In this chapter, I describe the measurement techniques and applications.

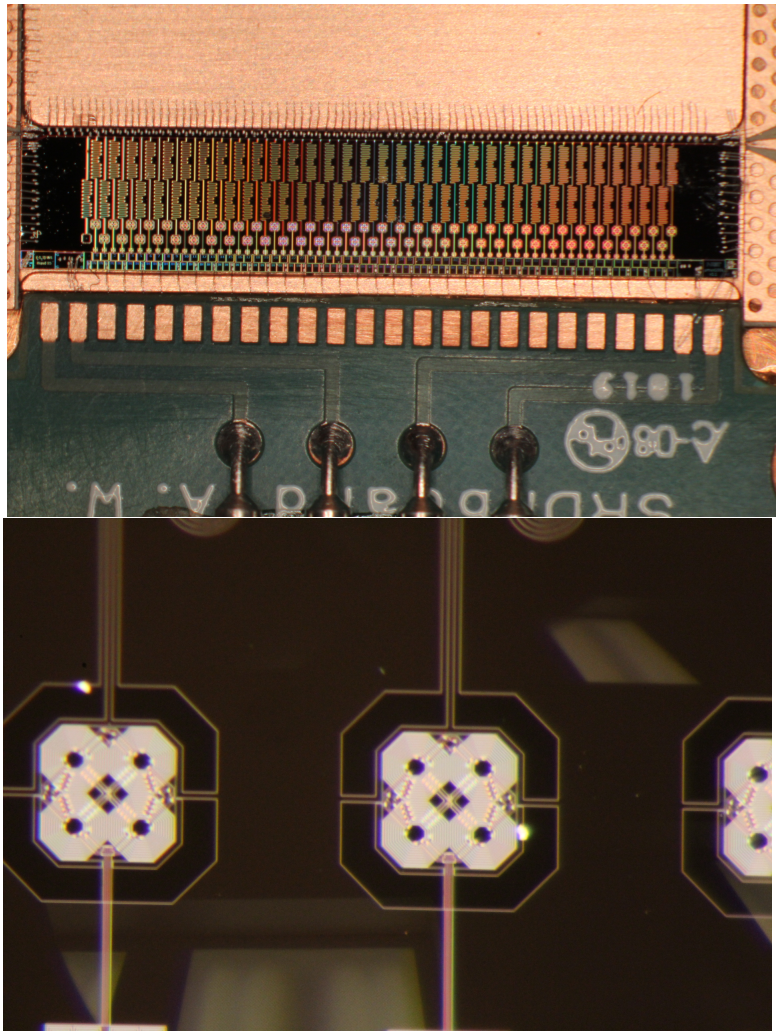

Figure 4.1: Pictures of an example the μ-MUX chips under test in this chapter. Fabricated at NIST. *Top*: Image of the chip under magnification. The individual resonators are visible. The chip is integrated in the test box. *Bottom*: Magnification of the RF-SQUID portion of the resonator. Four RF-SQUIDs are visible. They are counter-wound to eliminate sensitivity to spatially constant ambient magnetic fields.

4.2 Description of μ-MUX

Like the time domain multiplexing scheme of Chapter 3, the μ-MUX scheme couples a TES bias circuit to a SQUID. An excellent overview of this multiplexing method is described in [45]. The SQUID in the μ-MUX circuit is an RF-SQUID rather than a DC-SQUID. The RF-SQUID couples into a microwave resonator, shifting its resonance frequency as a function of the magnetic flux through the RF-SQUID.

A complication arises because, like the voltage in the time domain multiplexing case, the resonant frequency of the resonator is periodic (approximately sinusoidal) as a function of the magnetic flux. The readout electronics can see shifts in the resonator frequency, but can't determine the SQUID's position on the f-Φ (frequency vs magnetic flux) curve, nor demodulate that directly into an input signal from the TES. The SQUID input response must be linearized. In TDM, this was achieved by "servoing." In μ-MUX, linearization is achieved by flux-ramp modulation.

Figure 4.2 shows a schematic of the detector and resonator circuit. The TES bias line is inductively coupled into the RF-SQUID, as is a "flux ramp" line. The flux ramp line couples to every RF-SQUID in the readout chain. A sawtooth wave is fed into the flux ramp line, causing the resonator to sweep through a few periods of the f-Φ curve. The TES bias circuit couples some additional magnetic flux into the SQUID. Assuming the change in flux due to the TES signal is slow compared to the flux ramp frequency, the flux from the TES creates a phase offset in the f-Φ. The readout electronics measure the resonant frequency over time, and the phase becomes the detector signal. See Fig. 4.3.

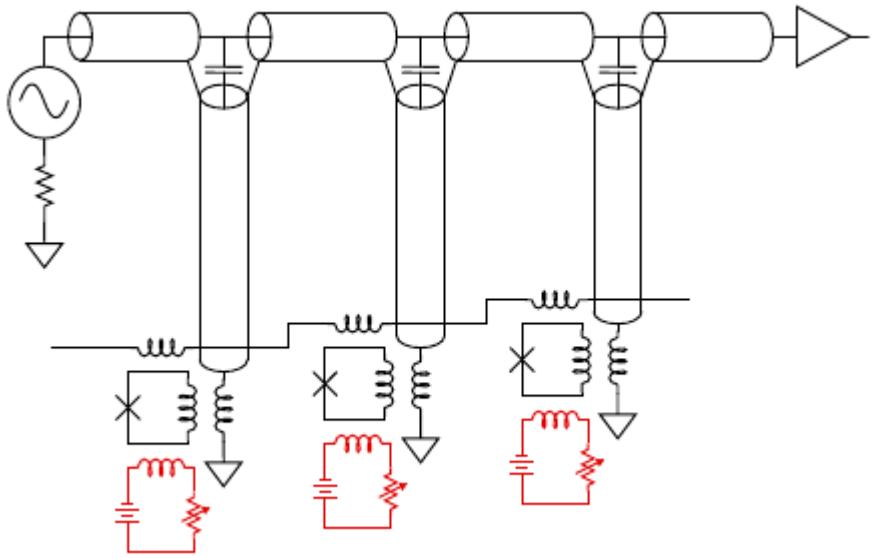

Figure 4.2: Schematic of a set of three Transition Edge Sensors read out by μ-MUX resonators. The TESes couple to RF-SQUIDs, modulating the resonator frequency. The flux ramp line is also visible, coupling into each RF-SQUID. Figure is from [45].

4.3 Apparatus

At Cornell, we took measurements of the microwave resonators with our dilution refrigerator at $\sim$ 100mK. My goal was to take measurements of the resonator centers and quality factors, and to trace out the f-Φ curve for each resonator. Since this measurement doesn't require real-time, high speed data acquisition, I used a vector network analyzer (VNA) to take measurements of the resonator S_{21}. I couldn't take measurements of detector time streams this way; that would require specialized readout hardware, like a ROACH2 [60] or SMuRF [29] system. Both of these readout systems were eventually acquired by the laboratory.

The flux ramp line was biased by a signal generator set to a constant voltage signal. The flux ramp signal passes through a warm 10 kΩ resistor, constituting

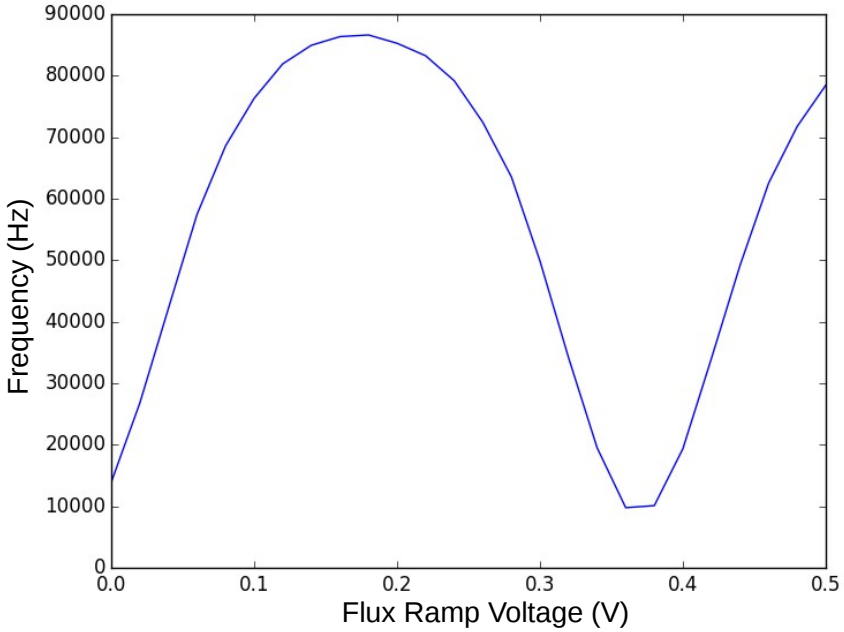

Figure 4.3: A μ-MUX resonator f-Φ. The y-axis has had a constant $\sim$ 5 GHz subtracted to provide better scale. In these data, the resonator depicted in Fig. 4.8 was fit using the method described in Sec. 4.4.2. Then, the voltage down the flux ramp line was increased by 0.02 Volts, and the process repeated until the flux ramp voltage was 0.5 Volts. The f-Φ curve depicted here is the fitted resonator center frequency f_0 as a function of flux ramp voltage. In an actual readout system, the flux ramp would pass through several Φ_0 periods, and the f-Φ would be fit to a sine wave. The phase becomes the detector signal, since a phase shift will occur when the current changes in the coupled TES bias line.

the majority of the flux ramp line resistance. Both the VNA and the signal generator were controllable by an ethernet SCPI interface, allowing for complete automation of data acquisition.

The microwave readout line was calibrated such that the entire cryogenic system was the device under test; this was necessary since the calibration source was not cryogenic. A series of stainless steel coax lines passed the signal into

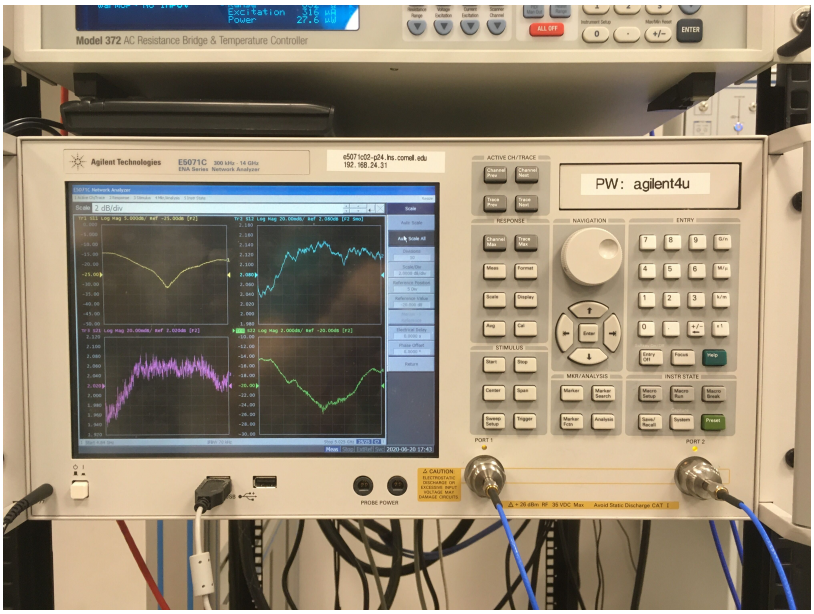

Figure 4.4: VNA used in the resonator measurement experiments.

colder stages through SMA connectors. On the 4 Kelvin stage, 20 dB of attenuation, plus an additional 20 dB directional coupler, precede the resonator chip. After the resonators, the signal passes through a circulator and bias-tee before being amplified by a cryogenic Low Noise Factory 4-8GHz LNF-LNC4-8C HEMT. It then passes up the cryogenic stages, out of the cryostat and back to the VNA. See Fig. 4.5.

4.4 Resonator Fitting

Accurate determination of the resonator center frequency f_0 is necessary for extraction of the detector signal. Accurate measurement of the quality factor Q is also useful for calculating the level of noise contributed to the signal by the multiplexing electronics.

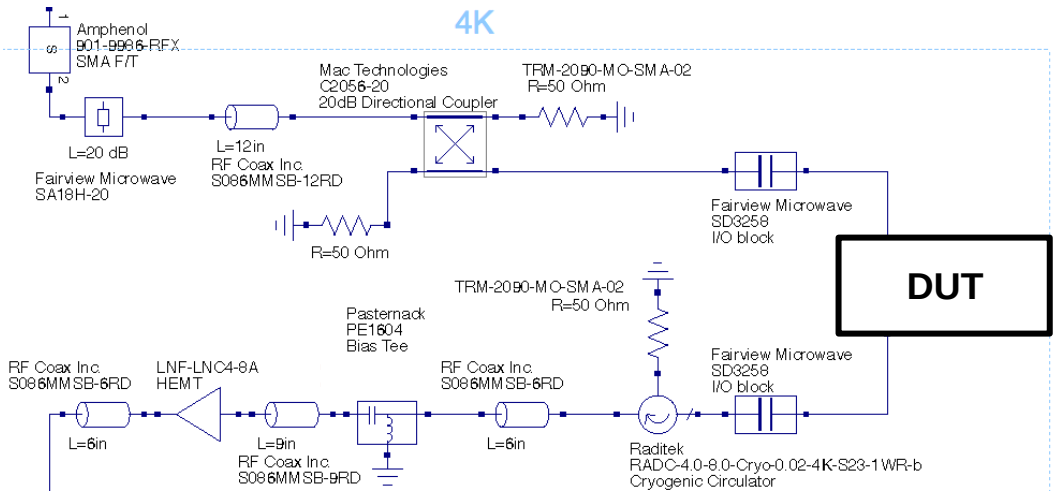

Figure 4.5: Diagram of the 4 K stage of the resonator measurement circuit. The device under test (DUT) here is the set of microwave resonators. Microwave input is at the top left, and output is the bottom left. This schematic is modified from one created by Shawn Henderson.

The method used for extracting these can vary depending on the application. In real-time applications, such as in the field, fast algorithms implemented in hardware and FPGA-based firmware are necessary. In some readout implementations, such as ROACH systems, the resonator center frequency is determined in the multiplexer tuning process. A frequency comb consisting of the combination of center frequencies of all resonators on the microwave line is transmitted down the line. The magnitude and phase shift of the output is recorded over time, and used to infer how the resonator shifts and extract a signal.

Newer systems, such as SMuRF electronics, may implement tone-tracking. This scheme functions similarly, but the frequencies transmitted in the comb are changed to match the frequencies of the resonators as they shift. This new method can greatly improve noise performance and nonlinearity properties.

More complete data can be collected and accurately analyzed in circum-

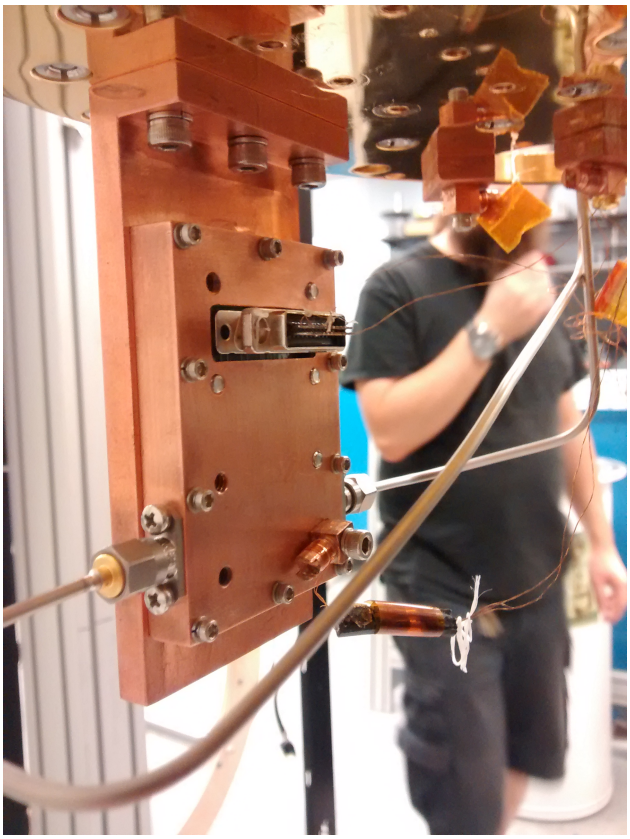

Figure 4.6: The μ-MUX test box, mounted beneath the cold stage of the dilution refrigerator. Steel coaxial cables connect the input and output on either side. A 25-pin connector routs the flux-ramp line. This 25-pin connector could also be used to carry a TES bias circuit in the event that the box contains test detectors. Author in the background.

stances that don't require fast, real-time acquisition of the signal. This can be done with, for example, a VNA. The method outlined in the rest of this section is designed to be implemented with a VNA and was used to characterize properties of TES μ-MUX resonators for the Simons Observatory at Cornell.

4.4.1 Determining approximate f_0

A broad VNA sweep, covering the span of the entire resonator comb, must be taken first to find approximate f_0 for each resonator. These approximate f_0 are used to determine the VNA window that will be set to collect high resolution data for each individual resonator. Actually detecting each resonator and extracting f_0 is a more complex task than it might seem, especially if common code will be used to measure different collections of resonators in different circumstances.

One complication comes from the fact that it is hard to calibrate out the contribution to the S_{21} signal that comes from the cryogenic portion of the circuit (excluding the resonators). Fortunately, VNA S_{21} data changes much more rapidly as a function of frequency near high-Q resonators than it does due to other parts of the microwave line. An appropriately tuned high-pass filter removes non-resonator contributions to the signal effectively. The contribution due to the resonator is also affected by the filter; however, if the filtered S_{21} data passes below some small, negative threshold, it usually indicates the presence of a resonator. The point the data crosses below the threshold is the start of a resonator search window. The filtered data tends to go positive after f_0, defining the end of the window. The local minimum of the unfiltered S_{21} data within this window is taken to be a resonator center. See Fig.4.7.

This method is not precise, but is good enough for this application. It tends to fail in two cases. The first is if the resonator Q is poor enough that the resonator does not cross the threshold. In this case, the resonator may not even be a "real" resonator; if it is, it is likely of poor quality. The second case is in the event of two colliding resonators. In that case, only one of the resonators may

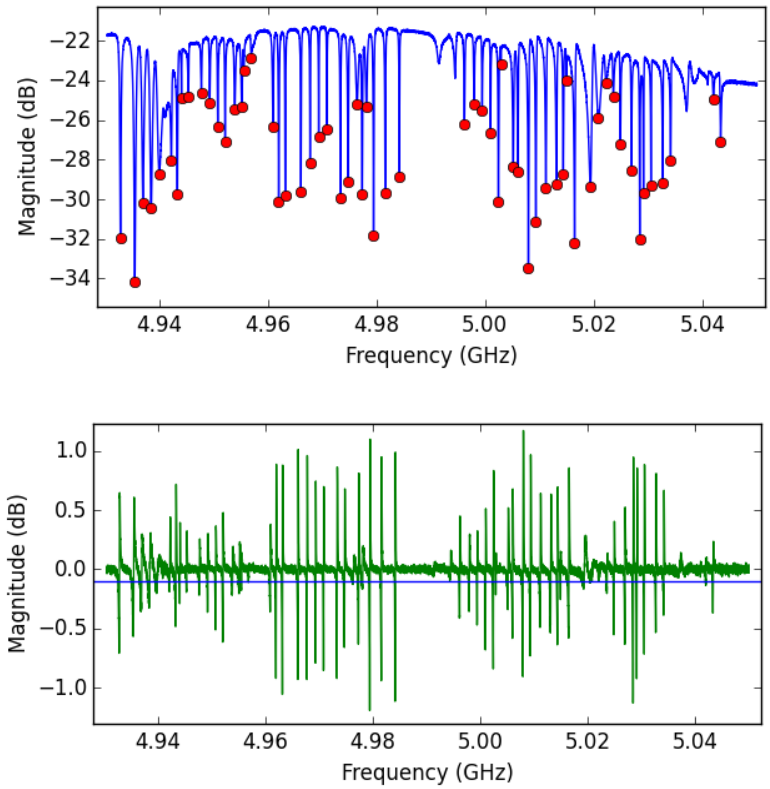

Figure 4.7: Example of the method described in Sec. 4.4.1 on a 64-resonator test box. *Top*: Raw S_{21}, with the discovered resonator centers marked with dots. 60 resonators were discovered. *Bottom*: The same data, with high pass filter applied. The horizontal line indicates the threshold used for discovering resonators. A resonator detection is "triggered" when the filtered data passes below this line.

be detected. Both cases lead to a false negative, but are indicative of an obvious, fatal problem with a resonator.

4.4.2 Resonator Precision Fitting

The list of approximate f_0 is fed into a data acquisition script that collects data for each of the detected resonators. These data are high-resolution sweeps taken

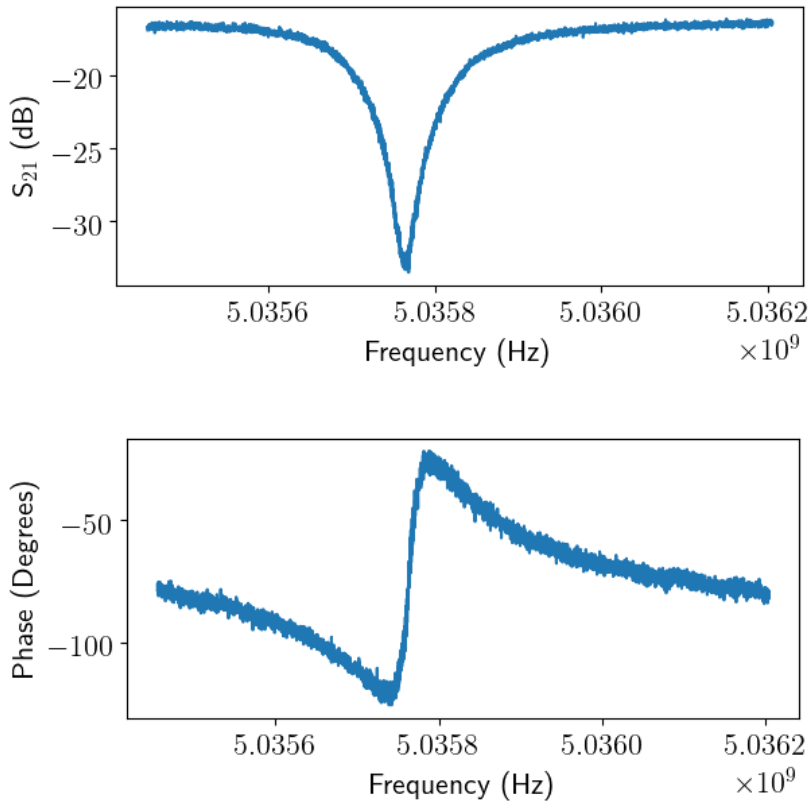

Figure 4.8: VNA traces of a single μ-MUX resonator with high resolution, for fitting as per Sec. 4.4.2. *Top*: Magnitude, *Bottom*: Phase.

in 1 MHz windows about each resonator singly. The data include both S_{21} phase and magnitude as a function of frequency. An example is shown in Fig. 4.8.

This work uses the method described in [52] to perform precision fitting of the resonator. I outline the method here. The first step is to map the S_{21} magnitude and phase data onto the complex plane. The real and imaginary components are sometimes referred to as I and Q components (in-phase and quadrature), but I will stick with the real-imaginary naming convention instead to avoid confusion of the Q component with the quality factor Q, and to be consistent with [52]. To perform this conversion, consider the magnitude and

phase data to be equivalent to radial coordinates (r, θ) in the complex plane; that is, take each point to be $re^{i\theta}$.

It is useful to have a good algorithm for fitting circles in order to work with resonator data in the complex plane. I use an algebraic method, using LaGrange multipliers and matrix algebra to analytically calculate the circle of best fit (it is the same method used by [52]). Note the curve the resonator forms in the complex plane is parameterized by frequency, so frequency data is lost in this conversion after fitting. However, transformed data points can still be mapped to their original frequencies.

Removing Envorionmental Factors

For an ideal resonator, these data form a circular arc in the complex plane. Actual resonator data will include environmental effects. In the model outlined in [52], the environmental factors accounted for are: first, an arbitrary phase and amplitude offset, applying a factor of $ae^{i\alpha}$; and second, a frequency dependent phase shift due to the time delay of the microwave stimulus traveling through the circuit, applying a factor of $e^{-2\pi i f \tau}$. Here, τ is the "cable delay."

The cable delay term distorts the circular data, since it shifts each data point by a different frequency-dependent phase. Since τ is roughly the time it takes a signal to travel between the ports of the VNA, it can be guessed approximately by knowing the length of cable involved and that the signal travels an appreciable fraction of the speed of light. Next, the complex S_{21} data are fit to a circle, assuming some τ, and the goodness of fit χ^2 is calculated. Then step τ some small amount and repeat. Few data points may be needed, since the χ^2 usually

fits well to some kind of polynomial of even degree (Fourth degree fits often work in this case; if not, the degree can be increased). If χ^2 shows a minimum for some value of τ in the tested range, that value is likely the cable delay. Extrapolation should be avoided, however.

The cable delay should be constant across a system, unless something has changed. Installing new cables or components requires a new calculation of τ. Otherwise, expect that it should be the same for all resonators in the system. Of course, the measurements aren't ideal, so if multiple resonators are available, measure τ for each of them, and select one that fits the system. There is a bit of an art to this, but forming a histogram of measured τ values and taking the median often gives a good approximation. Additionally, I have observed that order one factors of cable delay do not change the measured f_0 significantly. I measured a cable delay of 70 ns in the system at Cornell.

Final Fit

Once a reasonable value for τ has been established, the complex S_{21} data can be multiplied by $e^{-2\pi i f \tau}$ to cancel the effects of cable delay. Next, an algebraic circle fit determines the circle's center (x_0, y_0). The circle is translated so that its center is at the origin. Finally, these translated points are converted back into magnitude and phase data. The transformed phase vs frequency is fit to the model

$$\theta(f) = \theta_0 + 2\arctan\left(2Qr\left[1 - \frac{f}{f_0}\right]\right) \tag{4.1}$$

where r is the radius of the circle.

This is good enough to extract the resonator center frequency f_0. The Q

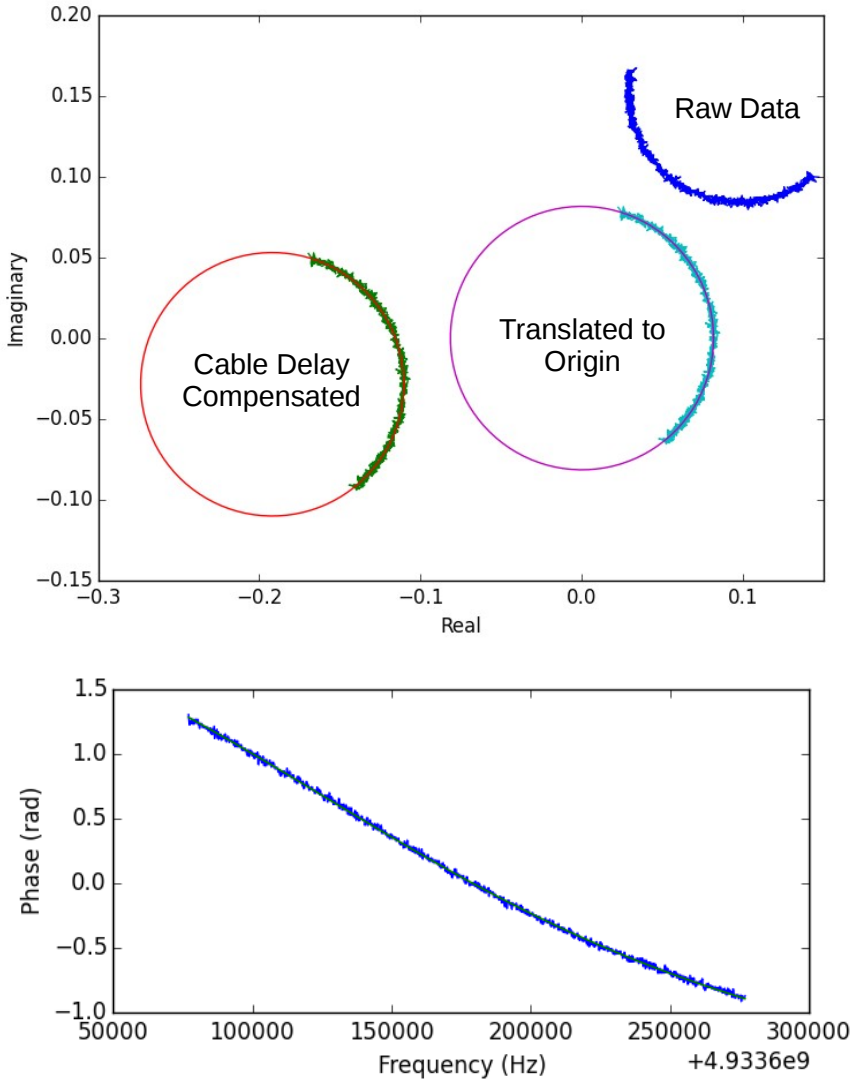

Figure 4.9: Fits to a resonator. The resonator data has been cropped to only data within the resonator well. *Top*: The resonator in the complex plane. I've shown the raw data, the data with the cable delay accounted for, and the same data translated to the origin. The latter two are shown with fits. Note that the raw data already looks pretty circular; the cable delay was calculated statistically by taking many different resonators into account, as described in Sec. 4.4.2. *Bottom*: The phase data for the resonator fit to the model in Eqn. 4.1. The data and fit are both shown, but the fit is difficult to see because it follows the data so closely.

in this equation is the total quality factor. The coupling quality factor Q_c, which is quality factor due to the environment, can be calculated by dividing Q by $2r\exp(i\arcsin(y_0/r))$ to account for the impedance mismatch. Finally, the internal quality factor, Q_i, which is an intrinsic property of the resonator, is $Q_i^{-1} = Q^{-1} - \mathrm{Re}\{Q_c^{-1}\}$.

Notice that an overall amplitude does not affect the fit, since it is a fit to phase only. An arbitrary, constant phase offset will affect θ_0 but not Q or f_0. Therefore, the environmental factor $ae^{i\alpha}$ is not necessary to extract measurements of interest. I therefore do not include it in my algorithm. Even so, [52] describes a method for extracting this environmental factor, which can be useful for fitting the same resonator more quickly in the future.

4.5 Application

This apparatus and this code were used to test the magnetic susceptibility of the μ-MUX readout in [62]. It has also been used to inform selection of magnetic shielding for the Simons Observatory. In these applications, a Helmholtz coil outside of the dilution refrigerator applies an external magnetic field, and the phase shift in the f-Φ curve is measured for each resonator as a function of external magnetic field.

This measurement is slightly complicated by two factors. First, the RF-SQUIDs are actually four separate SQUIDs, with coils wound in such a way as not to be sensitive to a constant magnetic field, but rather, a gradient of a magnetic field (they are "gradiometers"). See Fig. 4.1. Nonetheless, these measurements are suitable to give an approximate idea of the phase shift of a resonator

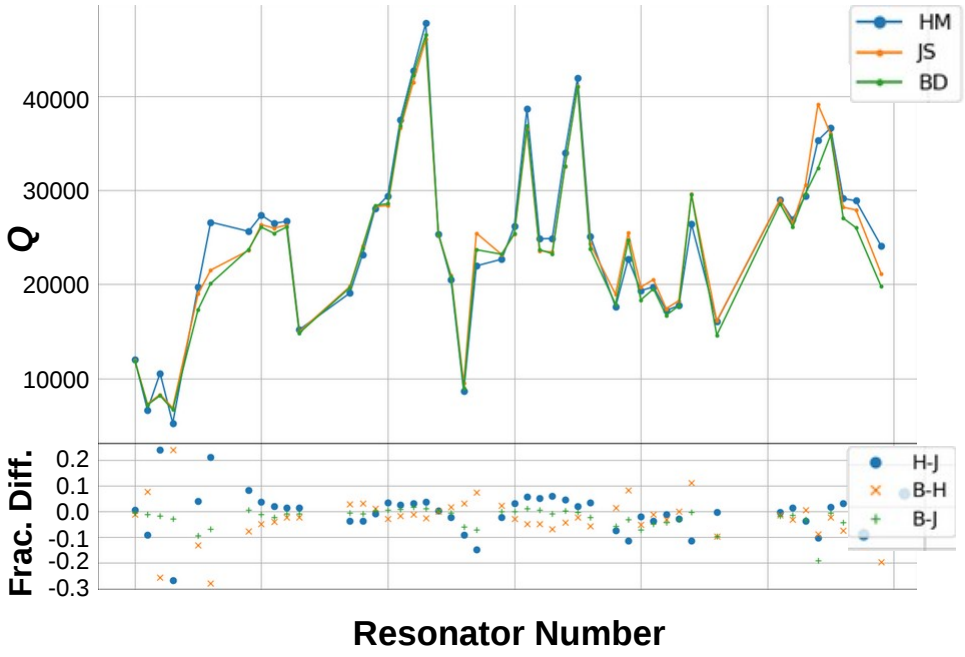

Figure 4.10: Comparison of the total quality factor Q of the same data for three different resonator fitting codes. The top plot shows the absolute Q as measured by each code, which is labelled by the initials of the author (J.S. is mine; the other two are by Heather McCarrick of Princeton and Brad Dober of NIST). The bottom plot shows the fraction difference in each, taken pairwise. A similar measurement of the f_0 shows negligible disagreement between the three algorithms. Plot contributed by Cody Duell.

in real world applications.

The second complication is the hysteresis of the resonator phase shift when a magnetic field is applied and removed. It was observed that the application of a magnetic field and then removal of the field did not return the resonator f-Φ to its original phase offset. However, performing this operation a second time did not further change the phase. Therefore, it is necessary to apply the max-

imum magnetic field and then remove it before taking measurements in order to "settle" the resonators. This may be due to the creation of superconducting vortices and their shifting to potential minima. Note that the resonator traces are Niobium, a type II superconductor.

The cryogenic μ-MUX system tested in these experiments will be deployed on the Simons Observatory [54], read out by SMuRF room-temperature electronics. Testing these multiplexers is important enough that three separate codes to fit resonators were written independently and compared, see Fig. 4.10. The differences in f_0 were negligible between the three, but there were some differences in Q. A standardized version of these codes is being used across Simons Observatory test institutions to characterize multiplexing components consistently.

CHAPTER 5

SURVEY STRATEGIES OF CHILEAN CMB TELESCOPES

5.1 Introduction

A survey strategy can be described as a schedule designating where a telescope should be observing as a function of time. Survey strategies are critical to a telescope's mission; they are highly dependent on science goals, and a number of complexities arise in efficiently designing them. Ground-based CMB survey strategies differ greatly from the survey strategies of satellite missions, and the strategies of Chilean telescopes differs from the strategies of south pole telescopes.

A ground-based CMB mission typically performs scans of the sky over a range of azimuth at some fixed elevation. The rotation of the Earth passes the fixed sky through the arc of the telescope scan over time. Fixed elevation scans aid in keeping the power incident on the detectors from the sky relatively constant, reducing the complexity of detector calibration and atmospheric systematics.

In this section, I describe the process ultimately used to design the survey strategies used in Advanced ACTPol. I apply the same techniques to design prospective survey strategies for the Simons Observatory. I will describe how fields are selected, how the strategies are assembled, how they avoid the Sun and the Moon, and how the quality of the strategies is measured. I focus on large area strategies. I hope that other cosmologists will find this text useful in designing Chilean CMB survey strategies into the future.

5.2 Selecting Fields

The target sky regions form a starting point for constructing any survey strategy. Target fields are largely selected as motivated by the telescope's specific science goals. For CMB telescopes, foreground dust emissions can be a significant systematic, so typically low-dust regions are targeted. There is also strong motivation to overlap with galaxy cluster surveys in order to study the Sunyaev-Zel'dovich effect.

Broadly, survey strategies can either target large or small sky fraction $f_{\rm sky}$. Typically, observing a smaller sky area allows the telescope to take more sensitive data of the region it observes. A smaller but deeper observed sky region has been used for attempts at initial detection of the tensor-to-scalar ratio r, since it allows a better signal-to-noise ratio, albeit only in specific modes of the CMB power spectrum. Wider survey areas allow analysis over a much larger number of modes, and will ultimately be necessary for constraint of r; additionally, larger areas are useful for other types of science that depend on measurement of smaller angular scale modes [1].

Prior to 2016, ACTPol observed less than 4000 square degrees [11] (which is $f_{\rm sky} < 0.1$). In 2016, with the deployment of AdvACT, the total observed sky area expanded greatly, targeting $f_{\rm sky} > 0.34$. The total observed sky area is greater still, since the telescope often observes outside the target region. The Simons Observatory will target an even larger sky fraction, with the large aperture telescope observing over half the sky [57]. These large area strategies allow greater overlap with optical surveys and also more effectively target smaller scale fluctuations in the CMB power spectrum.

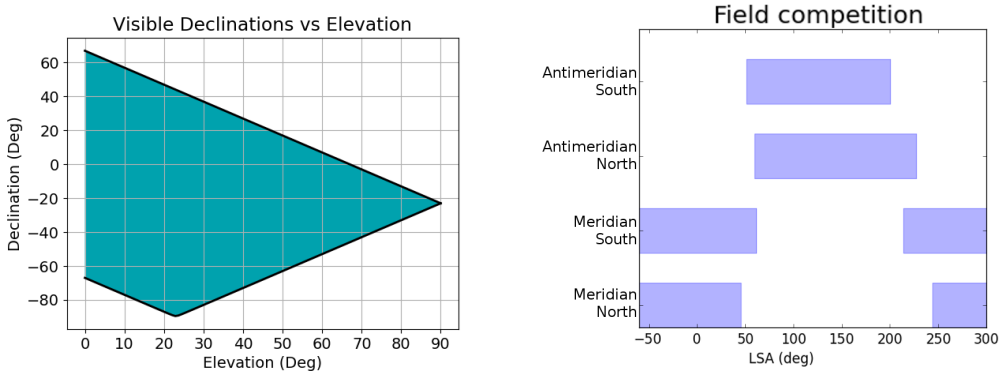

Figure 5.1: Left: Declinations visible from the Atacama desert, at 23° south latitude, as a function of telescope scan elevation. The shaded region is visible. Right: Ranges of local sidereal angles for which the various fields in a proposed Simons Observatory large aperture strategy are visible assuming a 40° elevation scan. Fields that overlap in local sidereal angle (LSA) can't be observed simultaneously. It is desirable for there to be some field visible for every LSA. These ranges are determined by the field definitions, scan elevation and whether a patch is rising or setting. From [57].

Large and small area surveys each have their own challenges, and in each case these challenges should be mitigated by wisely choosing the target fields. In the case of small area surveys, there may be large quantities of time where no targets are available, leading to low *observing efficiency* (the fraction of time the telescope has a target to observe). As $f_{\rm sky}$ increases, it becomes much easier to fill in the telescope idle time, but conflicts may be introduced as multiple fields are available simultaneously. See Fig. 5.1 right for an example of a large $f_{\rm sky}$ survey. The x-axis is local sidereal angle (LSA), which is analogous to local sidereal time (1 sidereal hour = 15°). Notice that the Meridian and Antimeridian fields are observable at different, complementary LSAs. The two Meridian fields can not be observed simultaneously, nor can the two Antimeridian fields.

Finally, a consideration for ground-based telescopes is that for a given po-

sition on the Earth, only certain declinations are observable. A given azimuth and elevation in horizontal coordinates will always point to the same declination in equatorial coordinates; this is just a result of the first equation in Eqn. 5.2 being time-independent. Each declination is only observable from a specific set of elevations as shown in Fig. 5.1 left.

5.2.1 Building the AdvACT Strategy

In 2016, AdvACT began targeting fields totaling over 14000 square degrees. Since then, AdvACT's strategy has been different at night than in the day. Initially, the daytime strategy observed a subset of the total area observed at night. While observing a smaller area in the day does increase observing depth within that area, a more significant consideration was sun avoidance; the path of the sun through the sky over the year did not pass through the daytime fields. Here, the definition of "day" is 11:00 to 23:00 GMT.

The field `wide_12h_n` was selected specifically to overlap with the BOSS survey [20]. It is the only field observed within its range of local sidereal angles in order to improve the observation depth. The `wide_01h_n` and `wide_01h_s` fields were selected to cover the low dust region near the southern galactic pole. The field `deep5` had been observed prior to 2016 and was selected to fill time the telescope would otherwise have no targets.. In 2019, `galactic_18h` was introduced over the galactic center. This field, like `deep5`, fills idle time and does not interfere with the `wide` fields. It is hoped that observations of `galactic_18h` will lead to measurements of astronomical objects near the galactic center. See Fig. 5.2 for a map of these fields.

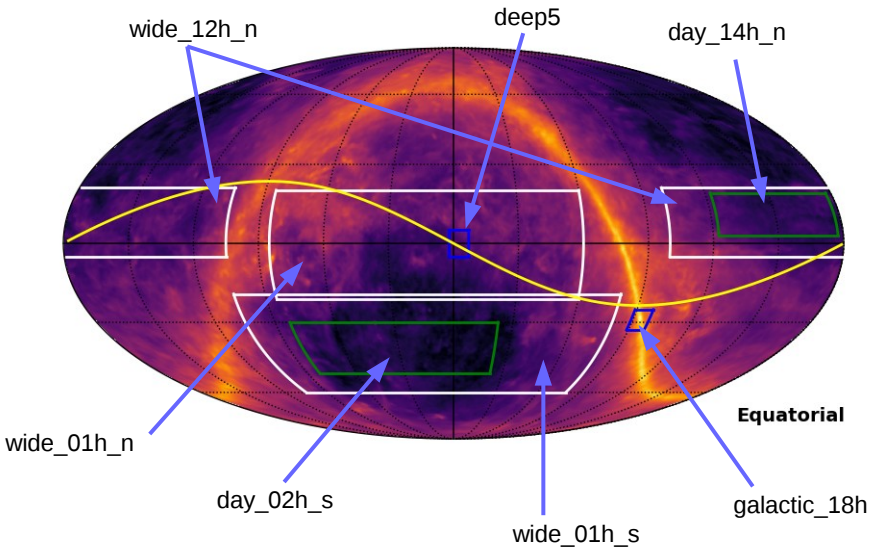

Figure 5.2: Advanced ACTPol fields plotted over the Planck dust map. The white outlined fields are the wide fields. These were initially observed only at night, but beginning in 2019 were observed for the entire schedule. The galactic center field and `deep5` field are in blue. The fields observed during the day prior to 2019 are in green. The yellow curve is the path of the sun over the year. Notice the sun does not enter the green daytime fields.

The two day fields together cover the full range of local sidereal angles, but do not conflict with one another. However, there are a number of conflicts between the night fields that must be resolved in order to improve uniformity of depth across the fields. The solution implemented is to develop twelve independent survey strategies and interleave them, cycling between each of the strategies daily at 23:00 GMT. The twelve strategies represent unique combinations of observing options.

Since `wide_01h_n` and `wide_01h_s` are not simultaneously observable, one such option is which of these fields to observe on a given night. The second option is whether to observe the wide fields in the rising sky or the setting sky.

Day	North/South?	Rising/Setting?	Elevation	Complement
1	North	Rising	40°	South Setting 47.5°
2	North	Rising	45°	South Setting 45°
3	North	Rising	47.5°	South Setting 40°
4	North	Setting	40°	South Rising 47.5°
5	North	Setting	45°	South Rising 45°
6	North	Setting	47.5°	South Rising 40°
7	South	Rising	40°	North Setting 47.5°
8	South	Rising	45°	North Setting 45°
9	South	Rising	47.5°	North Setting 40°
10	South	Setting	40°	North Rising 47.5°
11	South	Setting	45°	North Rising 45°
12	South	Setting	47.5°	North Rising 40°

Table 5.1: The cycle of strategies used on Advanced ACTPol's wide fields. The strategy switches to the next at 23:00 GMT. After 12 days, the cycle begins again. On a given day, the telescope observes only the north or the south fields; it observes only the rising or setting sky; and it observes at only one elevation, as specified. The Simons Observatory classical strategies proposed in [57] are similar, but observe at differing elevations. The complementary strategy is used for Sun and Moon avoidance.

The last option is which of three elevations, 40°, 45°, or 47.5°, to perform the observations at. These three choices lead to the $2 \times 2 \times 3 = 12$ strategies. These strategies are listed, in order, in Tab. 5.1.

5.2.2 Building the Simons Observatory Classical Strategies

The Simons Observatory is deploying both small (~0.5 m) and large (~6 m) aperture telescopes, each of which will require their own separate observing strategies. The small aperture telescope will observe a relatively small sky fraction, $f_{sky} \sim 0.1$, in order to detect primordial B-modes. It will have a large field of view, with a diameter of $\sim 35°$. The large aperture telescope will have similar science goals to ACT and should observe $f_{\rm sky} \sim 0.4$ with a field of view of the or-

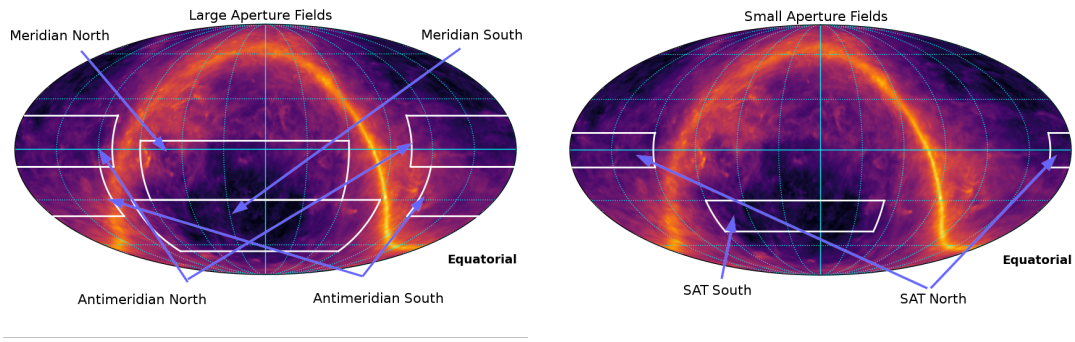

Figure 5.3: Simons Observatory target fields. Left: Fields for a proposed large aperture, large area survey over the Planck dust intensity map. The fields inside the boxes cover 17,095 square degrees and represent the region targeted by the telescope boresight. Right: Fields for a proposed small aperture survey. The boresight targets 4,920 square degrees, but in practice the observed area is much larger due to the 35° field of view of the telescopes. From [57].

der of a degree. In addition, measurements from the LAT will be used to delens the SAT observations [26].

In [57] strategies for these telescopes are presented in two variants: "classical" and "opportunistic." The classical strategies are constructed in a similar fashion to the AdvACT schedule, while the opportunistic schedules use software implemented in the CMB simulation and analysis library TOAST. I will focus on the classical strategies here. The fields targeted by these strategies can be seen in Fig. 5.3.

The LAT strategy is based heavily on the AdvACT strategy mentioned in Sec. 5.2.1, with some modifications. The Sun and Moon avoidance radius has been set to 30°, and the observing elevations are 40°, 44°, and 47°. The smaller fields `deep5` and `galactic_18h` have been removed. In place of naming the fields after their approximate right ascension, they have been named "Merid-

Day	Rising/Setting?	Elevation	Complement
1	Rising	50°	South Setting 57°
2	Rising	53°	South Setting 53°
3	Rising	57°	South Setting 50°
4	Setting	50°	South Rising 57°
5	Setting	53°	South Rising 53°
6	Setting	57°	South Rising 50°

Table 5.2: The cycle of strategies used on Simons Observatory SAT. This works similarly to the AdvACT strategy described in Tab. 5.1, but there are only six sub-strategies.

ian" and "Antimeridian" to describe their position on the sky relative to the meridian RA=0. Finally, both the Meridian and Antimeridian fields have a southern counterpart. Observations either observe both of the southern fields, or both of the northern fields, but none of the 12 sub-strategies observe both a northern and a southern field. The fields themselves have slightly different definitions. Finally, the avoidance radii have been changed; see Sec. 5.3. Aside from these changes, the strategy is constructed similarly to the AdvACT strategy. The sub-strategies listed in Tab. 5.1 also describe the LAT strategy except for the change in elevation.

The SAT strategy follows a similar format, but has a reduced number of fields and targeted sky fraction, $f_{\rm sky} \sim 0.12$. There are only two fields and one is clearly closer to the north galactic pole while the other is closer to the south, so they have simply been named "north" and "south." They exist at independent right ascensions and have been specifically chosen not to be simultaneously observable, so the SAT strategy does not require the north/south split used in the previous strategies. Observing elevations are 50°, 53°, and 57°. Unlike ACT and the LAT, the SAT has a very large field of view, $\sim 35°$. The target fields totaling $f_{\rm sky} \sim 0.1$ and shown in Fig.5.3 are the targets for the boresight; while the total

area observed is always larger than this, for the SAT this is especially true due to the large field of view. Other than these differences, the SAT strategy follows a similar construction to the LAT and ACT strategies, with a 6 day (instead of 12) cycle. The sub-strategies are described in Tab. 5.2.

5.3 Sun and Moon Avoidance

Beginning in 2017, Advanced ACTPol's night strategy implemented a Moon avoidance algorithm in order to mitigate the effects of optical power from the Moon entering the telescope's side lobes and inadvertently contributing to the measured sky signal. In the Atacama Cosmology Telescope, significant side lobes have been measured at $\sim 10^\circ$, $\sim 30^\circ$, and $\sim 90^\circ$ from the boresight [28]. The avoidance algorithm is described in this section. In 2019, with the implementation of the 12-day wide area strategy in the daytime, this algorithm is also used to avoid the sun. It is also used in the Simons Observatory classical strategies described in [57].

The algorithm is based on the idea that the Moon (Sun) is either in the rising sky or the setting sky, and observing the opposite *drift* (defined as whether the observation is rising or setting) to the Moon (Sun) will usually point the telescope away from it. I define *avoidance radius* as the angular distance between the astronomical object and the boresight within which the avoidance algorithm will be triggered. For AdvACT, this is set at 35° to avoid the 10° and 30° side lobes. Since there are twelve daily strategies to choose from, and one of the options that determines the strategy is the drift, a strategy with a different drift can be chosen when the object comes within the avoidance radius.

For each of the twelve strategies, a *complement* strategy is chosen; these are listed in Tab. 5.1. The complement strategy observes at opposite drift. When the Moon (or Sun) enters the avoidance radius, the strategy changes to the complementary strategy until the object would no longer be within the avoidance radius. This turns the telescope around and hopefully moves the Moon (Sun) out of the avoidance radius. In addition to changing the drift, the complementary strategy also swaps 40° elevation observations with 47.5° observations and swaps north fields for south fields. This should create additional angular separation between the highest elevation scans and their complements.

It is desirable for the avoidance algorithm to maintain as best possible the fact that an equal amount of time is spent observing with each of the twelve strategies. Therefore, it is important that the mapping from strategies to their complements is bijective. Maintaining this equal time distribution is facilitated by the fact that over the course of an orbital period, the Moon (Sun) spends a roughly equal amount of time at each right ascension, and therefore each strategy is subverted to its complement roughly equally.

This algorithm has some limitations. First, it is not guaranteed that shifting to the complementary strategy will move the object out of the avoidance radius. The greatest risk of this occurring should be when the object is closest to zenith. This problem is exacerbated by a larger avoidance radius, which is why the avoidance radius does not include the 90° sidelobe. Second, the Moon and Sun can't be avoided simultaneously with this method. Therefore, for strategies where this algorithm is used for both Sun and Moon avoidance, I use Sun avoidance when the sun is above the horizon (elevation 0°) and Moon avoidance is used when the sun is below the horizon. Power from the moon will likely enter

the sidelobes during the day.

The same algorithm is used in the classical strategies proposed for the Simons Observatory. For Simons Observatory strategies, the avoidance radius is reduced to 30°, and a hard cut is also set to 30°. That is, if switching to the complementary strategy doesn't work, the scan is replaced with idle time. These changes were made to facilitate comparison with the aforementioned opportunistic scheduler and could be changed before first light.

Since these strategies do not change fields in the daytime, the same technique is maintained as AdvACT 2019, using Sun avoidance when the sun is above the horizon and Moon avoidance otherwise. The stricter Sun and Moon avoidance used in these Simons Observatory results in reduced observing efficiency compared to AdvACT; whereas AdvACT's 2019 strategy has an observing efficiency of 98.5%, the Simons Observatory LAT strategy has only 91.3% efficiency. The SAT, due to its reduced observing area, has 64.6% efficiency.

An interesting representation of the efficacy of this algorithm is displayed in Fig. 5.4. These are similar to the hit maps described in Sec. 5.4 but show the amount of time the astronomical object of interest (either the Sun or the Moon) are within each pixel. The center of the map is the telescope boresight and the north pole of the map is 90° above the boresight along a great circle through the boresight and zenith. The white circle shows the avoidance radius. These plots clearly demonstrate that the time these objects spend within the avoidance radius is greatly reduced.

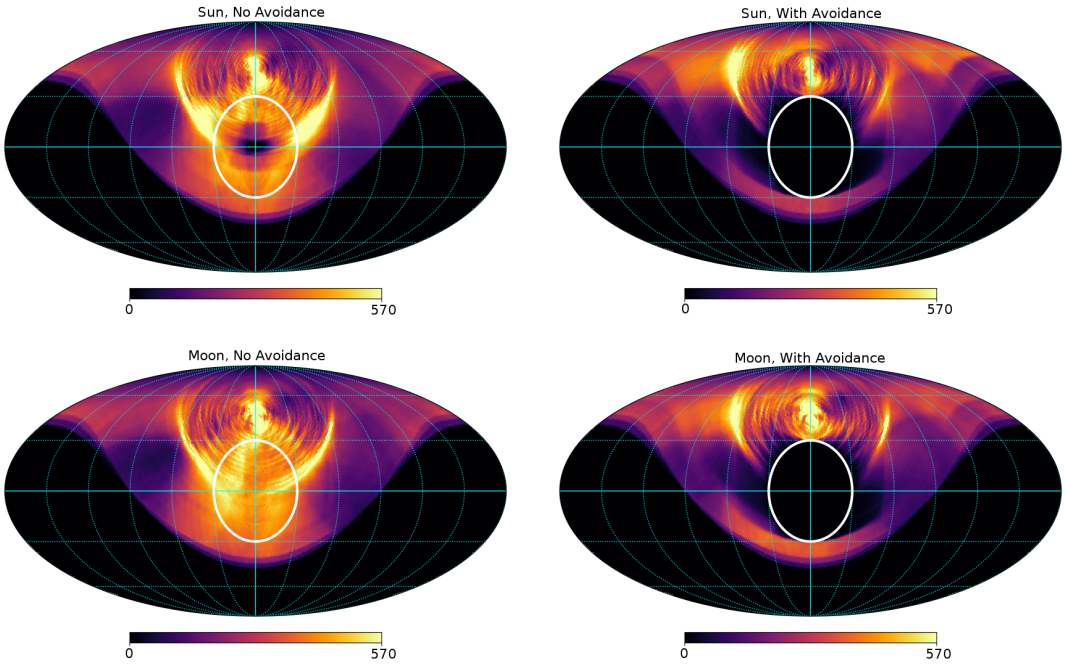

Figure 5.4: Sun (Moon) avoidance for the Simons Observatory LAT classical strategy. The coordinate system is defined such that the boresight is at the center of the map and the polar axis of the coordinate system is perpendicular to the direction the telescope is pointing. The central meridian corresponds to directly above and below the boresight in local coordinates. The depth shows the amount of time the Sun (Moon) is in each position in the sky relative to the boresight. The white circle shows the 30° exclusion region. Left maps show the strategy with neither Sun nor Moon avoidance, and right maps show the strategy with Sun and Moon avoidance. Top maps are Sun maps, and bottom maps are Moon maps.

5.4 Generating Hit Maps

Hit maps are useful tools for developing survey strategies. A hit map displays the time each sky position is viewed per unit area, or some variation of this. In this work, hit maps are typically expressed in units of seconds per square arcminute. This allows one to generate a more general hit map that doesn't de-

pend on the detector array. This "single detector" hit map could be multiplied by the number of detectors to get a map in units of detector seconds per square arcminute. Going a step further, if the detector array sensitivity in μK·s is also known, the formula

$$\mu\text{K arcmin} = \frac{\text{array sensitivity}}{\sqrt{\text{hits}}} \tag{5.1}$$

can convert the map into measurement noise [31].

Generating a hit map can be computationally intensive, so optimizing the calculation is necessary in order to generate hit maps on a standard workstation. In addition to writing the code in a high performance programming language like C++, the following methods can be used to optimize the code for time.

The telescope's fixed elevation scans are easily expressed in horizontal coordinates by considering line segments of constant elevation on the sphere. The hit map is expressed in a coordinate system fixed relative to the CMB, and for ground-based experiments, equatorial coordinates are typically used. Therefore, these optimizations will be highly dependent both on taking advantage of the simple geometry in horizontal coordinates, as well as the specific coordinate transformation between horizontal and equatorial coordinates.

To transform from horizontal to equatorial coordinates, use [61]:

$$\begin{cases} \sin\delta = \sin a \sin\varphi + \cos a \cos\varphi \cos A \\ \sin H = \frac{-\sin A \cos a}{\cos\delta} \\ \cos H = \frac{\sin a - \sin\delta \sin\varphi}{\cos\delta \cos\varphi} \end{cases} \tag{5.2}$$

where a is elevation, A is azimuth, φ is telescope latitude on the Earth, δ is declination, and H is the hour angle. Hour angle is defined by $H = t - \alpha$, where α is right ascension and t is local sidereal time.

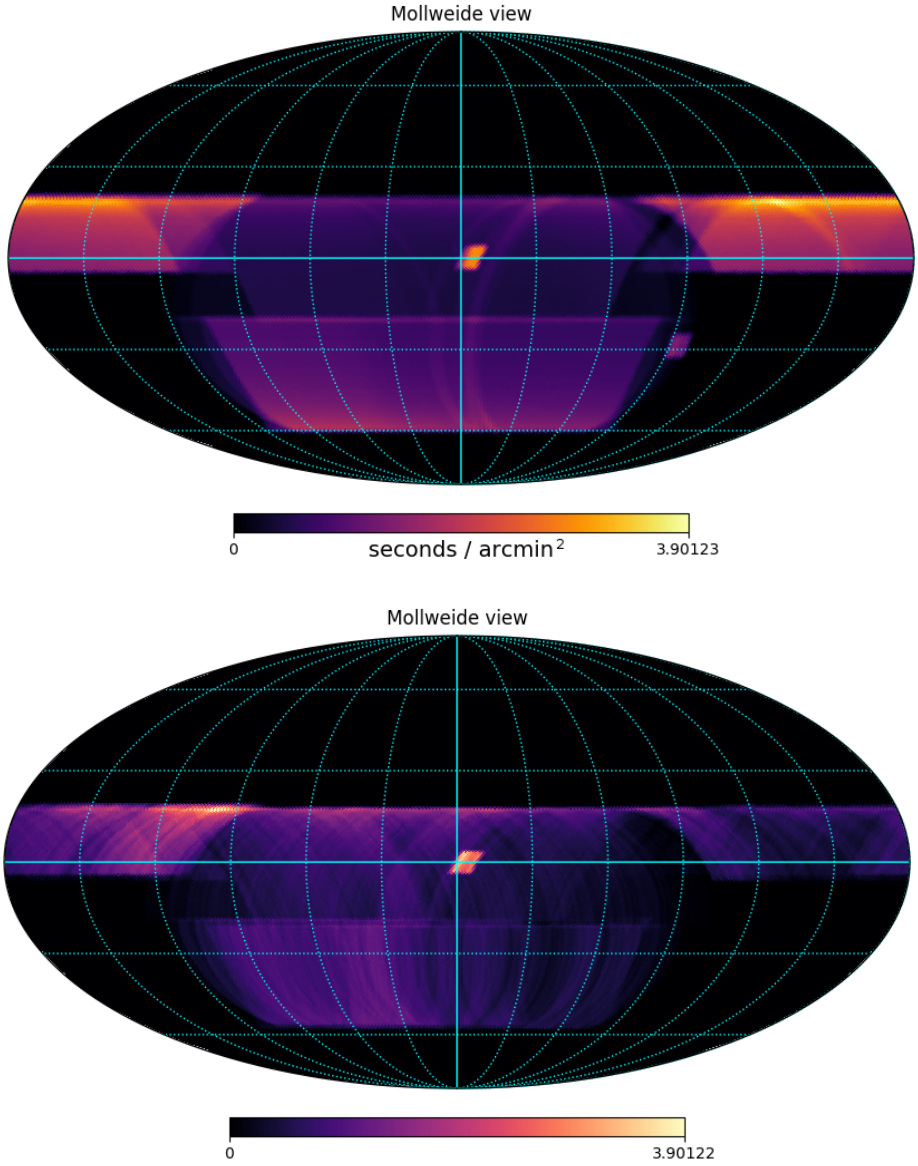

Figure 5.5: *Top*: The full simulated hit map for Advanced ACTPol, calendar year 2019. Assumes one detector, so this can be converted into detector seconds per square arcminute by multiplying the depth by the number of detectors. *Bottom*: Actual data for ACT, season 18, which is similar but loses the small field near the galactic center. The units are proportional to $1/\mu K^2$, which is approximately proportional to seconds/arcmin^2 but the conversion is nontrivial, so the map is peak-normalized to the top map. Some of the missing depth is expected, since in practice observations do not occur for the full calendar year.

There are two key observations that can be made here. The first is that declination is uniquely defined by the first equation, and this equation is time-independent. The second is that right ascension and time appear together only in the context of the hour angle; it is clear from their relationship that an advancement of time is completely equivalent to a proportional shift in right ascension. The combination of these two facts implies the following: if the telescope performs the same scan at two different times, the only effect will be to shift the scan in right ascension. This is true independent of scan geometry.

For an AdvACT-like strategy, there are only a few combinations of fields and elevations. The field's declination range, drift, and the telescope elevation uniquely define the scan's elevation, azimuth, and throw. Therefore, the scans can be divided into equivalence classes: two scans are in the same class if they have the same geometry (azimuth, elevation, and throw). Since the combinations of fields and scan elevations are limited, the number of classes is small compared to the total number of scans in a full schedule.

Since a class of scan always has the same geometry by definition, all scans within a class will be drawn the same way in equatorial coordinates except shifted in right ascension according to the local sidereal time. Therefore, the primary optimization is to generate a hit map for only a single local sidereal time for each equivalence class (it is convenient to choose $t = 0$), and only the first time that scan class is encountered. Then, create a histogram (in the form of an array) that stores the amount of time that class of scan occurs as a function of the local sidereal time. The number of bins in this histogram is dependent on the desired map resolution; it should be exactly as large as the number of pixels along the right ascension axis. After the entire schedule has been stepped

through, a hit map of each scan class can be generated by shifting the $t = 0$ hit map through each local sidereal time, multiplying it by the time in the array, and adding it to the total map. Finally, the maps for each scan class can be added to obtain the full hit map. See Fig. 5.6 to see examples of these intermediate maps.

The great-circle distance is the shortest distance between two points on a sphere. It can be expressed:

$$\cos\mu = \sin a_1 \sin a_2 + \cos a_1 \cos a_2 \cos(A_1 - A_2) \tag{5.3}$$

where μ is the distance, and I have intentionally used a and A as the "latitude" and "longitude" coordinates, respectively, to refer to Eqn. 5.2; horizontal coordinates are the special case of interest here.

To generate the $t = 0$ hit map for each scan class, loop over each pixel, obtaining its horizontal coordinates at $t = 0$. In that pixel, store the fraction of the scan during which the telescope can see this pixel. For simplicity's sake, I have ignored the telescope turn around and assumed that the telescope scans at a constant rate across the sky. If a circle with a radius equal to the field of view is drawn around the pixel, then the fraction to record is the fraction of the line segment defined by the scan geometry that is within the circle. If the line segment is entirely contained within the field of view sized circle, then store 1.0 (the telescope can see the pixel throughout the scan). If the line segment is entirely outside of the circle, store 0 (the telescope can never see the pixel).

Usually, this fraction can be calculated by first calculating the intersection of the pixel-centered circle with the line (not line segment!) of constant elevation a. Typically, this involves plugging the field of view in for μ and solving Eqn. 5.3 for $A_1 - A_2$. If there is no intersection, then either $\cos(A_1 - A_2) > 1$, which implies the constant a line lies entirely outside of the pixel-centered circle and a 0

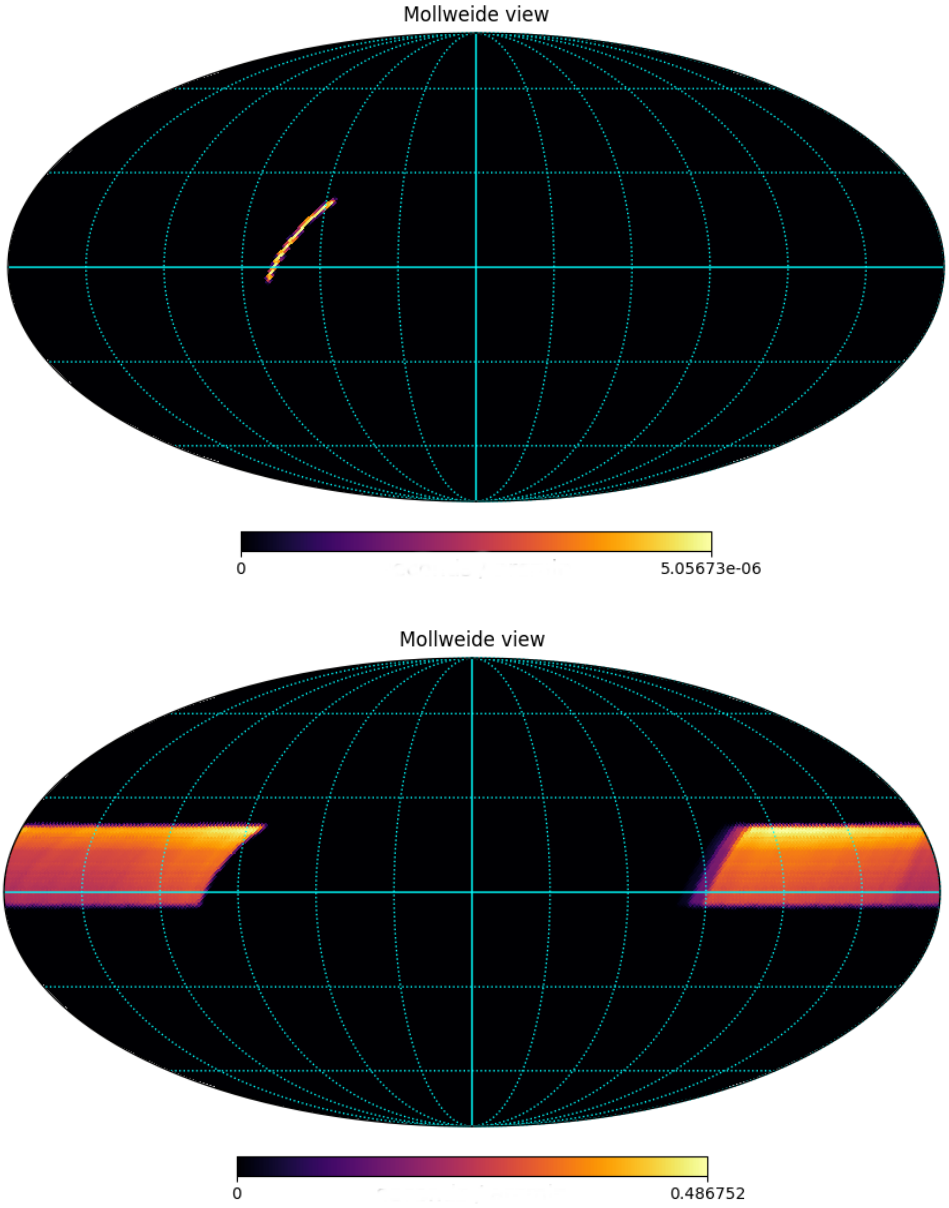

Figure 5.6: Examples of hit maps for one scan class. The top map shows the scan only at local sidereal time 0. The bottom map is the shifted and added map for the scan class across the entire schedule. Maps like the bottom one are generated for each scan class and summed to form the full hit map in Fig.5.5

.

is recorded, or $\cos(A_1 - A_2) < -1$, in which case the constant a line lies entirely within the pixel-centered circle, and a 1 is recorded. This latter case won't happen under normal circumstances, as it requires a large field of view telescope looking near zenith.

5.5 Cross-linking

It is desirable in a ground-based survey strategy to have good *cross-linking* in order to reduce systematics associated with the telescope scan direction. Informally, good cross-linking is the property that the telescope scan direction crosses each pixel at many different angles uniformly. In the worst case of a badly cross-linked pixel, every scan of the pixel will cross it at the same angle. Good cross-linking reduces systematics associated with the telescope scan direction and enables maximum-likelihood map making. See [57] and [59] for further discussion.

One metric for assessing the quality of cross-linking for a given pixel is by analogy with Stokes parameters. In this method, ignore "circular" polarization and reduce the Stokes vector to:

$$\begin{pmatrix} I \\ Q \\ U \end{pmatrix} = \begin{pmatrix} I \\ Ip\cos 2\phi \\ Ip\sin 2\phi \end{pmatrix} \tag{5.4}$$

For a single observation, I is the duration of the observation, $p = 1$, and ϕ is the crossing angle of the scan, which differs from the parallactic angle by 90°. Actually, the parallactic angle can be used instead, since an arbitrary offset of ϕ does not affect the final result. Sum the vectors from each observation. In

the resultant map, I will be the usual hit map and p is the figure-of-merit for cross-linking. Values of p range between 0 and 1 with values closer to 0 being preferable. Note that this can be achieved, for example, by making an equal number of orthogonal observations.

There is a region without cross-linking near $\sim -34^\circ$ declination. To understand what causes this, first consider the equations used to determine the crossing angle in Eqn. 5.4:

$$\begin{aligned} \sin\phi &= \frac{\sin\varphi - \sin\delta\sin a}{\cos a\cos\delta} \\ \cos\phi &= -\frac{\sin A\cos\varphi}{\cos\delta} \end{aligned} \tag{5.5}$$

which can be derived by applying the spherical law of cosines to the astronomical triangle and relates the crossing angle ϕ to the coordinates of the observed point. If the crossing angle is a multiple of 180°, due to the symmetry of the sky, it will also be a multiple of 180° for the opposite drift (and therefore, observing the opposite drift contributes the same to Q and U, preventing good cross-linking). This happens if $\sin\phi = 0$, i.e. $\sin\phi = \sin\delta\sin a$. It's easy to see this occurs for a single elevation. For a telescope at latitude $\varphi = -23^\circ$, at elevation $a = 45^\circ$, declination $\delta = -33.5^\circ$ will be poorly cross-linked. There is still a poor cross-linking region if multiple elevations are observed, where the vector sums of Equ. 5.4 happen to have a component that cancels, leading to totally "polarized" observations. For example, by setting $\sin\phi(a = 47.5^\circ) = -\sin\phi(a = 40^\circ)$, it can be seen that the $\sin\phi$ components of these two types of observations cancel at declination $\delta = -34.3^\circ$, assuming the two elevations get equal observing time. This cancellation occurs close to the $\delta = -33.5$ of the 45° elevation observations, so somewhere near that declination we might expect to see a region of zero cross-linking. Unfortunately, it is nearly impossible to avoid poor cross-linking for *some* declination, since for any set of reasonable observing elevations there

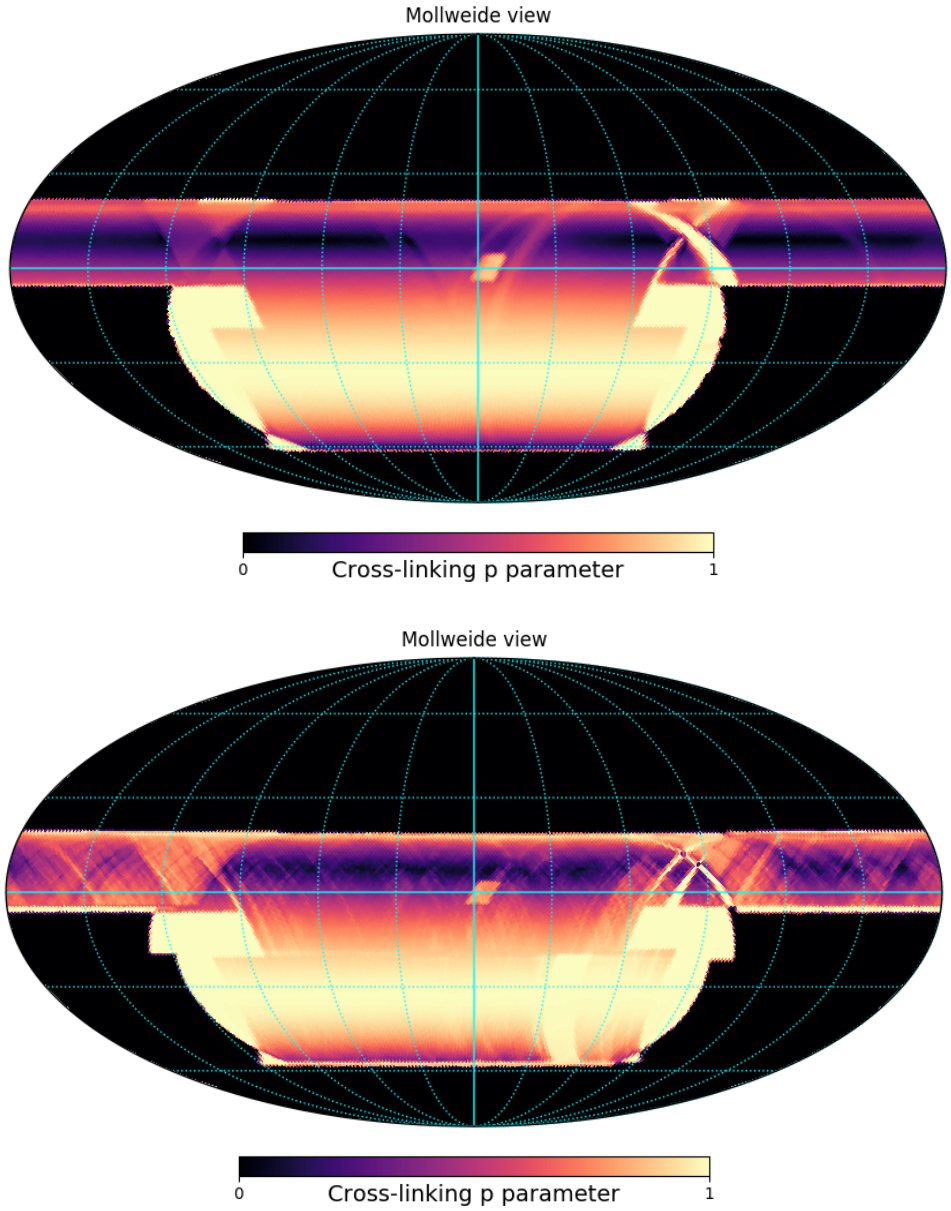

Figure 5.7: *Top:* Cross-linking parameter p for the Advanced ACTPol 2019 schedule from Fig. 5.5. Values closer to zero are preferable. Notice there is a region near declination $\delta = -34^\circ$ where it is impossible to achieve any cross-linking due to the sky geometry. *Bottom:* Cross-linking parameter p calculated from on-sky data, 2018 season. The telescope scans can be made out in the data, and telescope down-time may contribute to a difference between the two maps, but they are nonetheless quite similar.

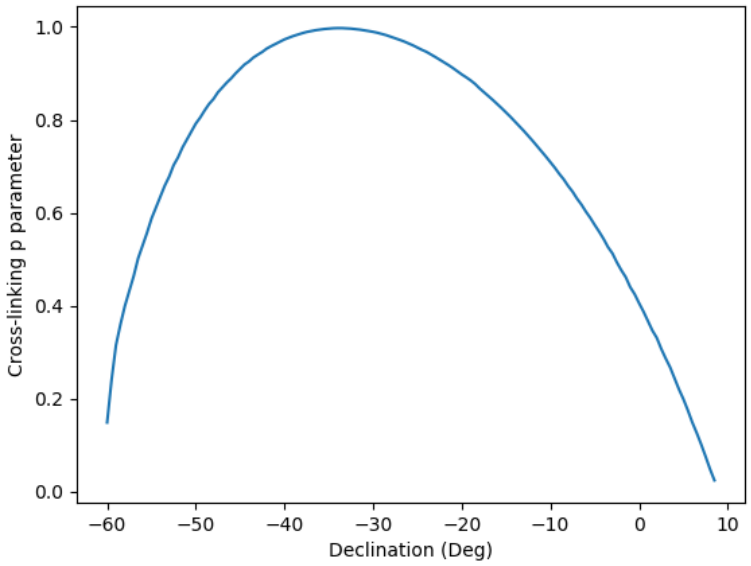

Figure 5.8: Crosslinking parameter p vs declination for AdvACT 2019. This is measured through a line of constant $RA = 30°$, and excludes the extremes of the measured declination range where edge effects of the scan dominate. The no cross-linking region can be seen at $\sim -34°$.

will be a region where these vector components cancel.

5.6 Measuring the Quality of Observing Strategies

One of the most difficult questions one must address when optimizing observing strategies is: "What makes one strategy better than another?" This becomes complicated by the fact that different goals interfere with one another. For instance, observing a larger area will probably reduce the depth of measurement per unit area. Observing at higher elevations may reduce systematics from the atmosphere but will limit observing efficiency and survey area. Getting good cross-linking and uniformity of field measurement improves analysis but may

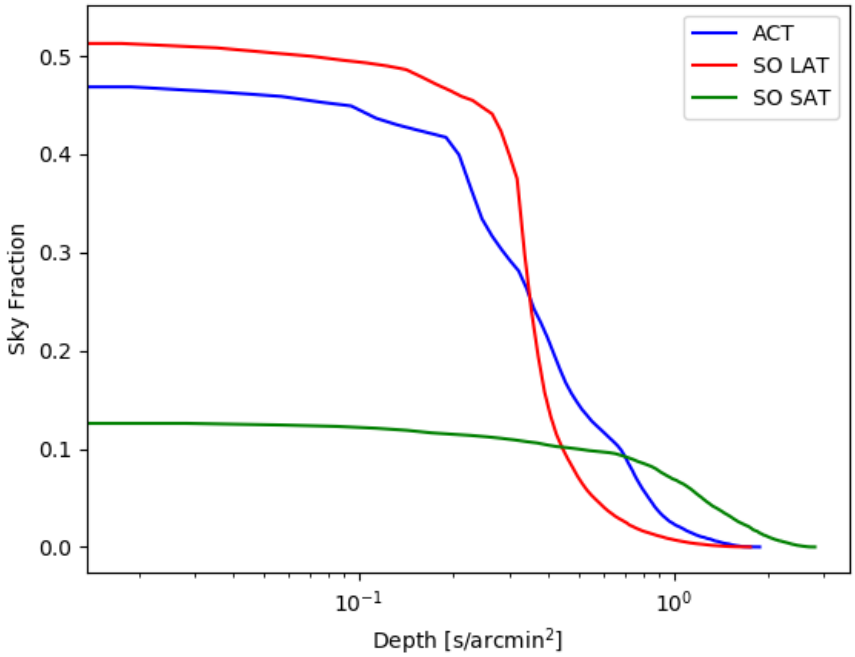

Figure 5.9: Fractional sky area deeper than a given depth for the outlined strategies for the calendar year 2019. Plots like this one can be insightful both for comparing depth of strategies as well as measurement uniformity.

introduce additional complications. While choosing one strategy over another is usually dependent on specific science goals, in this section I will outline various metrics that are used to compare the quality of one strategy to another. Most of these have been mentioned already, but I hope this list will provide a useful explicit reference.

1. Depth of measurement. The more time is spent on an observation the more sensitive the measurement.

2. Sky fraction. It is advantageous to observe larger sky fractions for many science cases. This may conflict with depth of measurement. Additionally, one may consider the *effective* sky fraction rather than the total sky fraction,

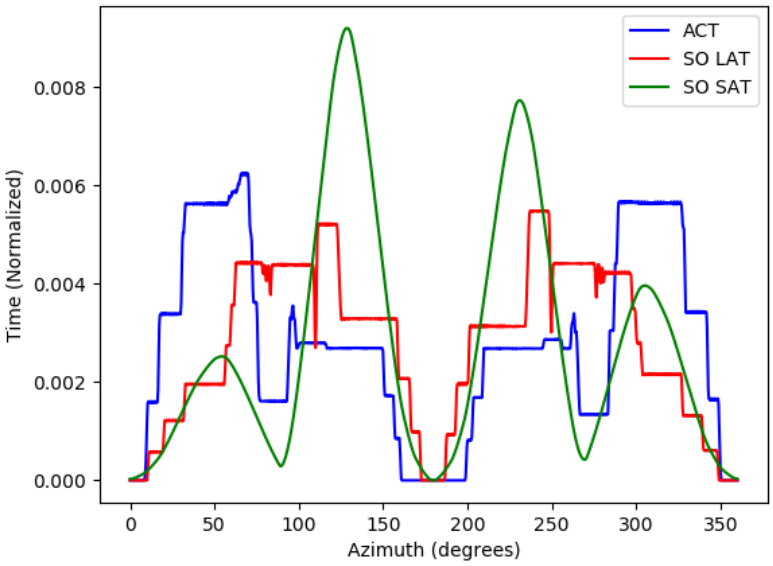

Figure 5.10: Normalized detector time spent at each azimuth for the three described strategies. The Simons Observatory SAT has a relatively simple structure with four peaks, which represent the four unique combinations of field and drift. The larger 35° field of view is clearly discernible here. The ACT and Simons Observatory LAT have a similar structure to each other, with sharper steps between scan regions due to the small field of view, and a more complex structure of different scan types. A plot like this one can yield insight into systematics introduced due to pick up of power from the ground into the telescope side lobes.

as defined by:

$$f_{\text{sky,eff}} = f_{\text{sky,tot}} \frac{w_2^2}{w_4} \tag{5.6}$$

where w_i is the ith moment of the projected weight map [32].

3. Foreground noise. Mostly I am referring to observing away from the galaxy and its associated dust, but this may include making observations at higher elevations to reduce atmospheric noise.

4. Observing efficiency. Telescope downtime should be minimized, and often it is better to make poor quality observations of an uninteresting target

than to make none at all.

5. Cross-linking. This is typically optimized by observing at different drifts and elevations. See section 5.5.

6. Measurement uniformity. Data analysis is aided by having approximately equal observation depth across an entire target field. See Fig.5.9 for a plot demonstrating a measurement of field uniformity for the strategies described in this chapter.

7. Power from side lobes. Telescope side lobes represent power received by the detector that is not from the direction of the telescope pointing, and objects within these side lobes can contaminate the signal. This is partially mitigated by Sun and Moon avoidance. Additionally, there is side lobe power due to objects on the Earth, which are usually at a fixed position in horizontal coordinates. This can introduce additional systematics that are also mitigated by observing different drifts and elevations. See Fig. 5.10 for an example of a plot that shows detector time relative to these fixed ground objects.

The large area Advanced ACPol strategy and the Simons Observatory strategies share several traits in common to optimize each of these characteristics. A large sky fraction is observed in each case, but I attempt to avoid observing the high-foreground galactic region by selecting fields appropriately. I selected three different elevations for each strategy, and observed fields both rising and setting, in order to improve cross-linking and reduce systematic noise. Finally, the daily cycling of strategies produces sub-strategies that generally have exactly one field visible at each local sidereal angle, reducing conflict and improving field uniformity. The division of large regions into both northern and south-

ern fields reduces the scan throw and thus further mitigates conflict near the edges of the fields. Results from Advanced ACTPol's large area scans are now beginning to be published [18][7].

CHAPTER 6

CURRENT AND FUTURE RESULTS

A final question remaining is how the instrumentation developed is influencing our understanding of the cosmology laid out in Chapter 1. Among upcoming Chilean CMB observatories, the Simons Observatory is most prominently featured in this dissertation. A discussion of this topic and the future of CMB measurements wouldn't be complete, though, without also mentioning CMB-S4 and CCAT-prime. This chapter covers the status of ACT, the outlook of future observatories, and a small sample of their forecasts. The forecasts presented will generally relate to the topics covered in Chapter 1, as far as such forecasts are known. For more detailed information, I invite the reader to refer to the most recent publications by each collaboration.

6.1 The Atacama Cosmology Telescope

The Atacama Cosmology Telescope (ACT) collaboration is in the process of releasing its fourth data analysis, called DR4, consisting of data collected in the 2013-2016 seasons. The new data release includes some of the updates mentioned in this manuscript: a wide area, $\sim$ 17000 square degree survey area, and dichroic TES detectors, neither of which were present in previous analyses from ACT. The results are summarized in [18] and [7].

These two publications go into great detail regarding the details of the instrumentation and analysis. The results of the maximum likelihood fit of the power spectrum are included in [18]. There are some differences compared to the DR3 2017 results [43], attributable to the differences in the τ prior. In [7]

Figure 6.1: The Atacama Cosmology telescope. The telescope is located inside the large, visible ground screen, which mitigates pickup of systematic noise from the surrounding terrain from entering the telescope sidelobes. The structures in the foreground contain equipment and facilities. Author in the foreground.

Parameter	ACT	ACT+WMAP	ACT+Planck
$100\Omega_b h^2$	2.153 ± 0.030	2.239 ± 0.021	2.237 ± 0.013
$100\Omega_c h^2$	11.78 ± 0.38	12.00 ± 0.26	11.97 ± 0.13
τ	0.065 ± 0.014	0.061 ± 0.012	0.072 ± 0.012
n_s	1.008 ± 0.015	0.9729 ± 0.0061	0.9691 ± 0.0041
$\ln(10^{10} A_s)$	3.050 ± 0.030	3.064 ± 0.024	3.086 ± 0.024
H_0	67.9 ± 1.5	67.6 ± 1.1	67.53 ± 0.56
Ω_Λ	0.696 ± 0.022	0.687 ± 0.016	0.6871 ± 0.0078
Ω_k	$-0.003^{+0.022}_{-0.014}$	$-0.001^{+0.014}_{-0.010}$	$-0.018^{+0.013}_{-0.010}$
$\sum m_\nu$ [eV]	< 3.1	< 1.2	< 0.54
$N_{\rm eff}$	2.42 ± 0.41	2.46 ± 0.26	2.74 ± 0.17

Table 6.1: Some results from ACT DR4 release taken from [7]. I have included the six cosmological parameters included in Ch. 1 and a few other beyond-ΛCDM parameters relevant to the cosmology discussed in that chapter.

there are details about the map making and other analysis and extraction of cosmological parameters. In each case results are compared with Planck. The ACT and Planck results for H_0 are remarkably similar. See Tab. 6.1 and Fig. 6.2.

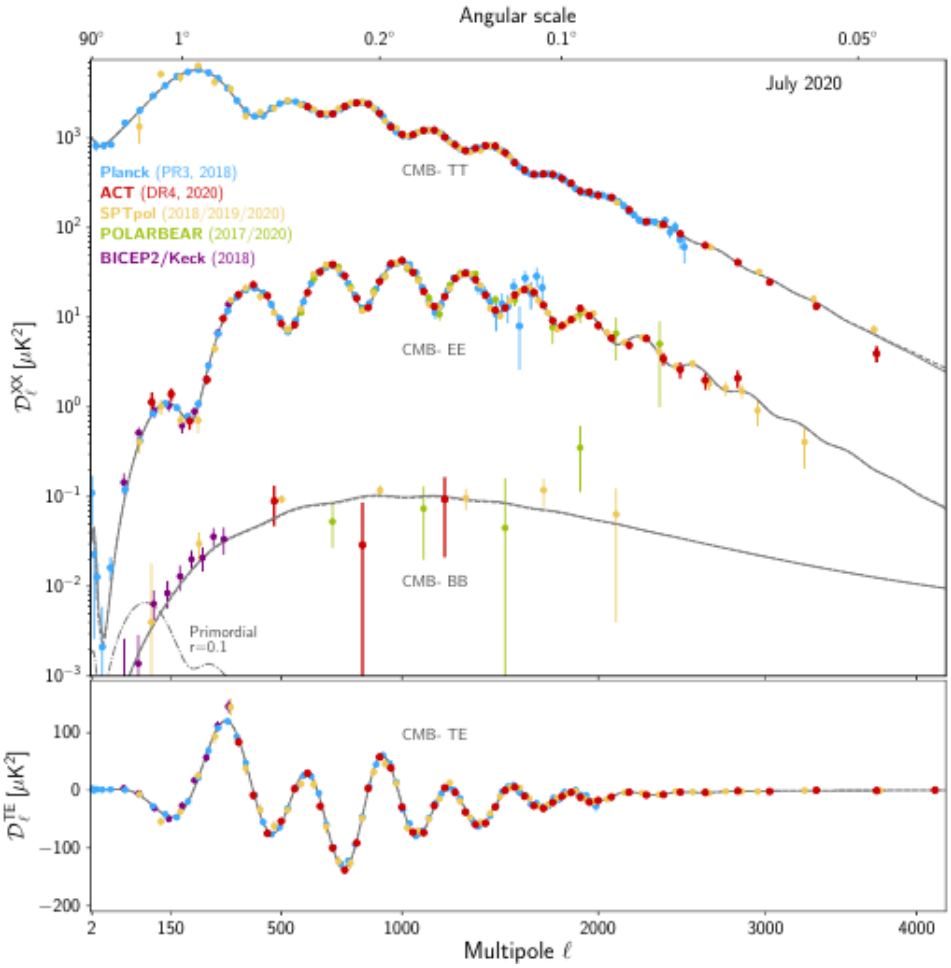

Figure 6.2: ACT DR4 power spectra fit, maximum likelihood. Taken from [18]. Includes one-sigma error bards and similar fits from Planck, SPTPol, POLARBEAR, and BICEP2/Keck.

6.2 The Simons Observatory

The Simons Observatory will be located adjacent to the ACT site on Cerro Toco in the Atacama desert. It will feature a large aperture telescope with a wide area survey strategy and three small aperture telescopes with smaller $f_{\rm sky}$ as discussed in Chapter 5. In total, it will deploy over 60,000 transition edge sensors spanning 27 GHz to 285 GHz in center frequency [56]. Observations are planned to begin in 2021.

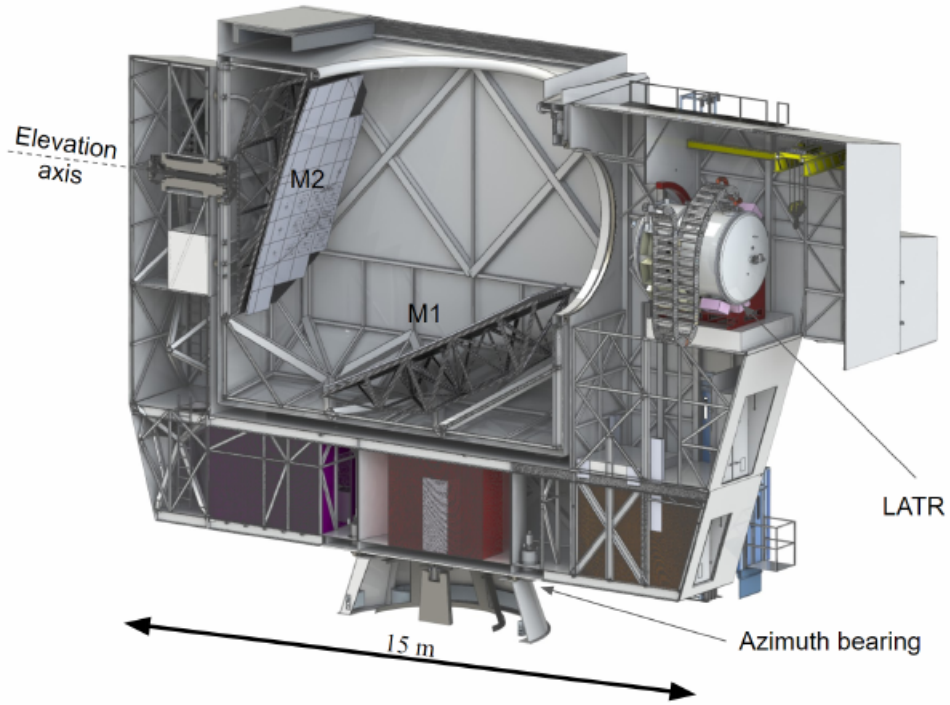

Figure 6.3: A cross-section of the Simons Observatory large aperture telescope design. This design is shared with CCAT-prime. The entire structure can rotate in azimuth, and the central portion containing the two mirrors M1 and M2 can rotate about the elevation axis. Light enters the telescope, from the top as oriented here, and reflects off the 6 meter primary mirror M1, then a 6 meter secondary M2, before entering the large aperture telescope receiver (LATR). Figure is from [64].

These forecasts come from [26]. All Simons Observatory forecasts listed here include an additional 25% uncertainty in case of as yet undetermined systematic effects. The forecasts assume that Simons Observatory data will be combined with Planck data. The Simons Observatory lists both a "Baseline," or nominal, value, and a "Goal" value, both of which are discussed here.

The Simons Observatory baseline for $\sum m_\nu$ is measurement with an uncertainty σ = 40meV and goal σ = 30meV. This could provide the first cosmological detection of nonzero neutrino mass if $\sum m_\nu$ is greater than about 100 meV.

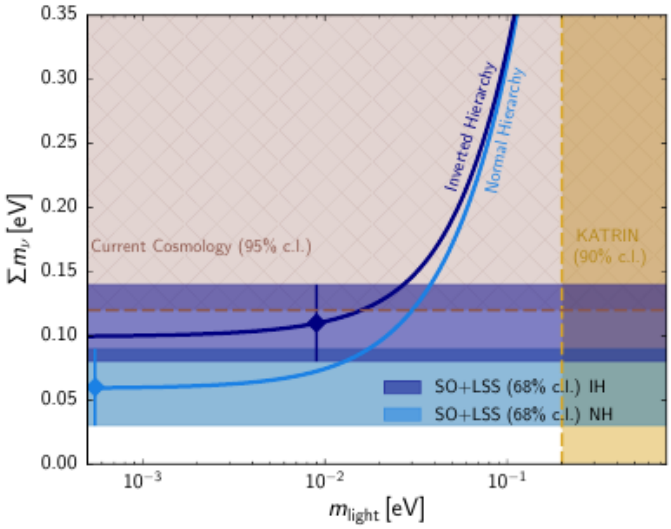

Figure 6.4: Simons Observatory constraint on the sum of the neutrino mass $\sum m_\nu$. The x-axis is the lightest neutrino mass eigenstate m_{light}, and the curves show $\sum m_\nu$ for both the normal and inverted heirarchy. The brown dashed line shows current cosmological constraints, and the colored bands show examples of the Simons Observatory uncertainty when combined with large scale structure measurements. Figure is from [5].

A sufficiently small $\sum m_\nu$ would suggest a normal mass hierarchy. These constraints will come from a combination of CMB lensing and SZ effect analyses.

The baseline figure for N_{eff} is measurement with an uncertainty $\sigma = 0.07$, and goal $\sigma = 0.05$. This uncertainty could rule out with 95% confidence any models with more than three light non-scalar particles in thermal equilibrium with the standard model particles, since these must contribute at least 0.047 to N_{eff}. This constraint will be extracted from a combination of temperature, E-mode, and lensing power spectra.

Regarding dark energy, the baseline uncertainty for the Hubble constant H_0 is $\sigma = 0.04\text{km s}^{-1}\text{Mpc}^{-1}$, with a goal uncertainty of $\sigma = 0.3\text{km s}^{-1}\text{Mpc}^{-1}$, with a combination of temperature, E-mode, and lensing power spectra. Additionally,

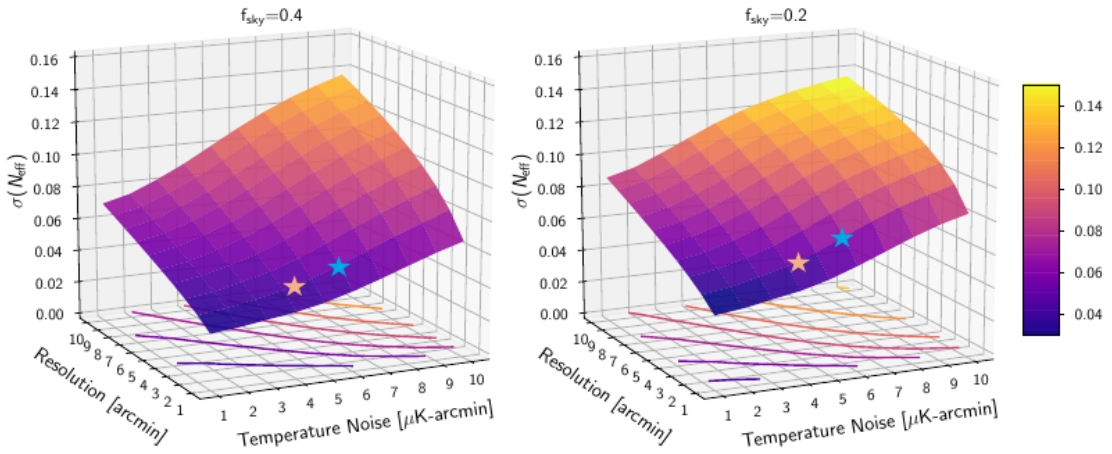

Figure 6.5: Simons Observatory forecast showing uncertainty on $N_{\rm eff}$ as a function of resolution and temperature noise for two different $f_{\rm sky}$ values: $f_{\rm sky} = 0.4$ (left) and $f_{\rm sky} = 0.2$ (right). The stars represent the baseline and goal uncertaintys. Figure is from [5].

lensing and SZ data, when combined with data from LSST [3] will constrain the amplitude of matter perturbations at $z > 1$. This parameter, called σ_8 for short, can be used to determine any deviation from a cosmological constant. The baseline uncertainty for σ_8 is 2%, but the goal uncertainty is 1%. Assuming the model from Eqn. 1.14, the baseline uncertainty on w_0 is $\sigma = 0.06$ and the baseline uncertainty on w_a is $\sigma = 0.2$.

The Simons Observatory forecasts also include dark matter constraints, assuming certain models. In the case of ultralight axions with an axion mass 10^{-26} eV, the axion fraction Ω_a/Ω_d (fraction of dark matter energy density Ω_d that is axions) has a baseline uncertainty of $\sigma = 0.005$. In the case of a dark matter-baryon interaction, Simons Observatory has baseline forecasts on the scattering cross section σ_p. For a 1 MeV dark matter particle, Simons Observatory expects to place an upper limit on the scattering cross section of $5 \times 10^{-27}\text{cm}^2$; for a 1 GeV dark matter particle, this upper limit is $3 \times 10^{-26}\text{cm}^2$. Current upper limits, from

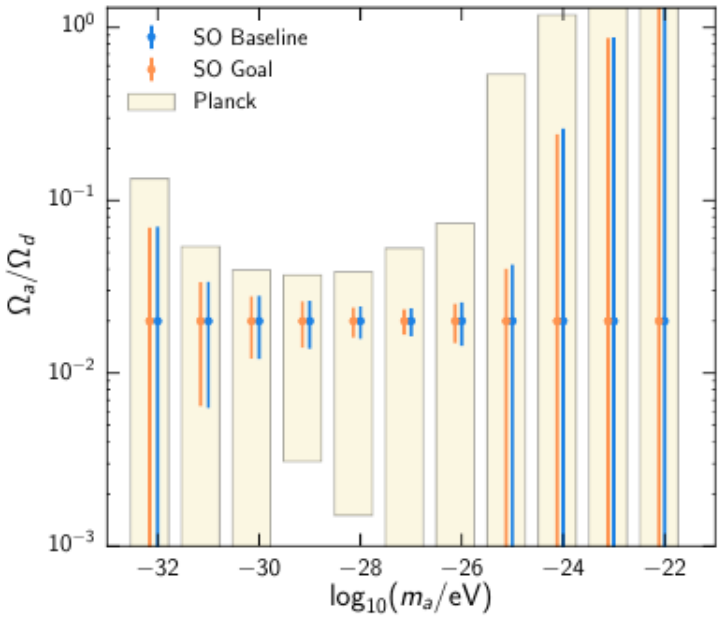

Figure 6.6: Simons Observatory forecast showing axion fraction Ω_a/Ω_d as a function of the logarithm of the axion mass m_a. The 1σ uncertainties are shown for both Simons Observatory baseline and goals, as well as the Planck uncertainties. The calculation assumes fiducial axion fraction is 2% of total dark matter content, and a neutrino mass of 0.06 eV. Figure is from [5].

Planck, are about an order of magnitude higher.

Finally, Simons Observatory B-mode measurements, combined with large-scale structure surveys for delensing, will constrain the tensor-to-scalar ratio r with a baseline uncertainty of $\sigma = 0.003$ and a goal uncertainty of $\sigma = 0.002$ (assuming $r \approx 0$. A non-zero detection of r implies the existence of primordial B-modes, providing evidence for inflation).

Many other cosmological variables that will be constrained by these measurements are described in [26].

This level of precision is only possible through great telescope sensitivity due to the large number of on-sky detectors the Simons Observatory will have;

the large area survey strategy, which overlaps with other, optical surveys; and the small aperture survey, which will be sensitive to large scale modes in the CMB power spectra.

6.3 CMB-S4

CMB-S4 represents the next generation of CMB telescopes collectively, beyond the current CMB stage 3 observatories. CMB-S4 consists of telescopes both in the Atacama desert and at the south pole. CMB-S4 will need of order 500,000 detectors on the sky in total to achieve its goals, many of which will need to be deployed on large aperture telescopes [4]. Current CMB-S4 forecasts are published in [1].

The CMB-S4 estimates on constraining the tensor-to-scalar ratio r suggest an uncertainty of order 10^{-3}. This constraint assumes 250,000 detectors dedicated to a B-mode search over the course of four years. An attempt has been made to anticipate measurement inefficiencies. Calculating the optimal $f_{\rm sky}$ to target in the B-mode search is complicated by a delensing requirement; see Fig. 6.7. Unlike the Simons Observatory, this means that the small aperture and large aperture strategies must overlap and be optimized together.

Assuming $\sum m_\nu \approx 58$ meV fiducially, CMB-S4 has a target 2σ uncertainty of $\sigma = 30$ meV and a 3σ uncertainty of $\sigma = 20$ meV on $\sum m_\nu$, with the outlook improving if $\sum m_\nu$ is larger. The bottleneck for this measurement is the optical depth τ, which currently comes from Planck large angular scale E-mode measurements. A cosmic variance limited τ and 2.5 μK-arcmin survey noise would reduce the $\sum m_\nu$ uncertainty to $\sigma < 15$ meV.

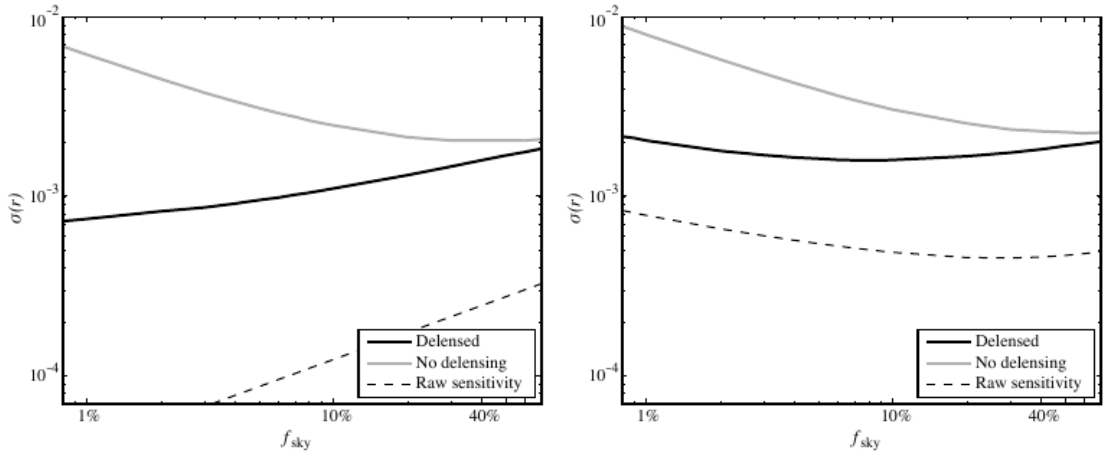

Figure 6.7: CMB-S4's forecasted 1σ uncertainty on r as a function of $f_{\rm sky}$. The left plot is in the case $r = 0$, and the right is in the case $r = 0.01$. Without delensing, the uncertainty decreases with larger $f_{\rm sky}$. Including delensing decreases the uncertainty, but has less impact at larger $f_{\rm sky}$, so that the relationship between the uncertainty on r and $f_{\rm sky}$ is not trivial. Figure is from [1].

The uncertainty on $N_{\rm eff}$ shrinks significantly with a larger $f_{\rm sky}$ survey; see Fig. 6.8. An $f_{\rm sky}$ of 0.2 brings the uncertainty on $N_{\rm eff}$ below 0.1 with a 1 arcminute beam. The CMB-S4 collaboration marginalizes this value over the primordial helium abundance Y_p, which is somewhat degenerate with $N_{\rm eff}$. The phase shift in the acoustic peaks mentioned in Sec. 1.3.2 will help break this degeneracy.

Combined with Planck data, CMB-S4 expects to constrain the Hubble constant H_0 to within an uncertainty of 0.24 km s^{-1} Mpc^{-1}. Tab. 1.2, which is an updated form of table 8-1 in [1], also lists uncertainties for the other five ΛCDM parameters.

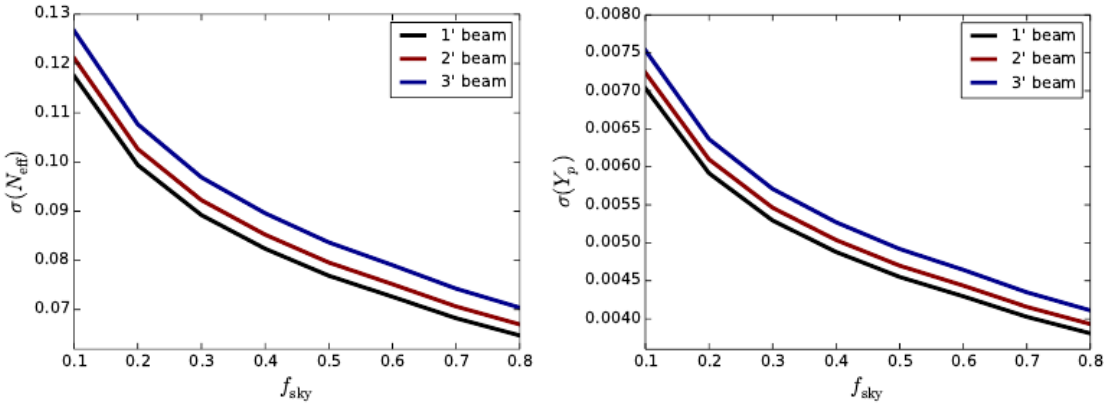

Figure 6.8: CMB-S4's forecasted uncertainty on $N_{\rm eff}$ marginalized over the primordial helium abundance Y_p (left) and errer bars on Y_p marginalized over $N_{\rm eff}$ (right) as a function of $f_{\rm sky}$. Calculations were done with 1, 2, and 3 arcminute beams; in both cases, the uncertainty decreases with larger $f_{\rm sky}$ and smaller beam size. These sensitivities are normalized to 1 μK-arcmin for $f_{\rm sky} = 0.4$, then scaled proportionally to $f_{\rm sky}^{1/2}$. Figure is from [1].

6.4 CCAT-prime

CCAT-prime will be located on Cerro Chajnantor, at 5600 m elevation; 400 m higher than ACT. The higher elevation decreases the amount of atmosphere the instrument has to stare through, improving its sensitivity [15]. It shares a telescope mechanical design with the Simons Observatory LAT, and expects first light in 2021. CCAT-prime's detectors will initially span 220-860 GHz, observing at higher frequencies compared to CMB telescopes like ACT or the Simons Observatory. These observations are designed to be complementary to other experiments [8].

The higher frequency CCAT-prime observations will enable different science. It will be able to better separate components of the SZ effect, which helps to constrain science derived from those measurements. It will be particularly

sensitive to galactic dust emission, so it can be used to improve foreground removal in B-mode searches. It will spectroscopically map the 158 μm [CII] emission line from star-forming regions to trace large scale density fluctuations and probe the structure of dark matter. CCAT-prime may provide the first detection of Rayleigh scattering of the CMB; measurements of this phenomenon may improve constraints on $N_{\rm eff}$.

6.5 Conclusion

I have only been able to give a very brief summary of the modern view of the universe and some of the instrumentation that is used to measure it. Many critical aspects of these projects are covered in other papers and theses that the interested reader could pursue.

I have covered a few basics of modern cosmology, and named a few open questions of interest in Chapter 1. I covered the complicated superconducting electronics in the next few chapters: multiplexing techniques and transition edge sensors. These and other cryogenic sensor technologies also have applications outside of cosmology, such as in X-ray science and national defense. Of course, the TES testing outlined in Chapter 2 has had a direct influence on the Simons Observatory final detector design.

Improvements in cosomological measurements depend significantly on improving sensitivity by increasing the number of detectors on the sky. The testing of over 1000 time domain multiplexer chips for Advanced ACTPol led to a large improvement in the final detector yield. This reduced the uncertainty of the ACT results referenced in this chapter. To get even more detectors in each ar-

ray, the μ-MUX method presented in Chapter 4 will be deployed on the Simons Observatory. Improvements in multiplexing factor like this one are absolutely necessary to increasing detector count since the physical constraints of the cryogenic electronics limit the number of signal lines that can be read out. An alternate detector technology, the kinetic inductance detector, naturally achieves a similar multiplexing factor as μ-MUX. Kinetic inductance detectors are planned for deployment on CCAT-prime.

Finally, those detectors must be put to use by pointing them at the sky in some systematic way, so I covered observing strategies in Chapter 5. The design strategies covered here are optimized for ground-based surveys of large areas on telescopes located away from the Earth's poles. Under other conditions, the design process for a survey strategy could vary drastically.

The survey strategy of a CMB telescope is directly responsible for the science that can be extracted from that instrument. The ACT large area survey strategy developed in Chapter 5 was the first large area strategy deployed on that instrument and led to the recent results out of our collaboration. This strategy will continue to produce results as future seasons of data are analyzed. It also formed a basis from which the Simons Observatory strategies began development, and likely will influence future telescopes. The high observing efficiency, as well as the Sun and Moon avoidance algorithms, lead to an improvement in measurement uncertainty by increasing effective integration time on the sky.

This final chapter described some of the upcoming experiments that will use these techniques. I also covered recent results from ACT, including the measurement of H_0 that was enabled by the large area survey strategies. I hope the work presented here tightens constraints on cosmological science for future tele-

scopes in addition to the ones that have been presented here. There will likely be many more such experiments of increasing sophistication far into the future.

APPENDIX A

SPECIFIC STEPS FOR COMPUTING AN OBSERVING STRATEGY

Here I describe the details of the specific steps implemented to compute an observing strategy, including what software I ran. I expect these details may not be relevant to most readers, but will be important for anyone with access to this software who is trying to reproduce these results.

1. Create each sub-strategy with `askans`. This is a software package written by Matthew Hasselfield for creating and analyzing observing strategies for ACT. An observing strategy could be made entirely in this step, but for large area strategies like AdvACT's, I find running the rest of the steps significantly improves the strategy. In this step, each sub-strategy should be made to observe at a single elevation and drift, and should fill as much local sidereal angle as possible without creating conflict between fields. This software will try to resolve conflicts when they arise, however, but greater field uniformity can be achieved by merging the fields manually.
2. Merge the sub-strategies with `jmerge.py`. This takes as input all of the sub-strategies and cycles between them, changing strategies at 23:00 GMT. This should be done again to create the "alternate" schedule, which changes the order of the strategies to swap each strategy for its complement. This alternate schedule will be used for sun and moon avoidance later.
3. Run `fill_gaps_with_alt.py` to fill any idle time in the observing strategy with the alternate strategy. This will improve observing efficiency. Later, if the sun or moon enter the avoidance radius during one of these times, the software will try to switch to the alternate schedule but will al-

ready be running the alternate schedule. This is one reason the trimming step may be important later. Note that this will not cause any drop in observing efficiency, since it was idle time only that was filled with the alternate schedule. This step could be skipped if the strategy is already very efficient, but can help improve efficiency greatly if the schedule is sparse.

4. Apply sun and moon avoidance. There are two separate `avoidance` programs, one for the Sun and one for the Moon, that can be applied individually. There is also a `divoidance` program that performs Sun avoidance when the Sun is above the horizon (el=0), and Moon avoidance otherwise. These programs work by filling any time the sun is within the avoidance radius with the alternate schedule. All three programs are written in C++ to improve performance, since the entire schedule must be run through in small time steps and the position of these astronomical objects is calculated at each time step.

5. Trim the schedules by running the `trim` programs for the Sun and the Moon. These programs are designed to remove any observations where the Sun or Moon are still within some defined radius of the boresight (I've often used 15°). This is necessary due both to the `fill_gaps_with_alt.py` code ran in an earlier step but also since switching to the alternate strategy is not guaranteed to clear the telescope of the Sun/Moon, especially if that object is near zenith. Further, it can be used to trim out time the Moon is within the avoidance radius during the day, when Moon avoidance is not applied.

6. Run `scan_clean.py` to generate a final version of the schedule. This performs two functions. The first is to remove scans that are less than 10 minutes in duration. It takes time at the beginning of each scan for the tele-

scope to change its pointing direction and re-tune the detectors. Therefore, particularly short scans are not useful. Secondly, the process of cutting and merging different schedule files described in the previous steps occasionally introduces instances where two identical scans occur back-to-back, and `scan_clean.py` combines these scans into a single scan.

7. Run `gaps.py` on the final schedule to calculate observing efficiency. This script also produces a histogram of the distribution of gap durations in the schedule.

8. Generate hit maps, cross-linking maps, etc.

APPENDIX B

OPTIMIZING TES INTERFACE CHIP INDUCTANCE ON ADVACT

A TES must be digitally sampled at a finite rate, which introduces aliasing noise above the Nyquist frequency. It is therefore beneficial to low-pass filter the circuit above this frequency by introducing an additional inductance on the TES bias line. This inductance must be carefully chosen not only because it affects the frequency response of the TES but also because the stability of the TES is affected by this inductance [36].

AdvACT interface chips have the option of being wired with varying inductances, either adding no additional inductance, 60 nH, or 200 nH [30]. However, the superconducting traces in the bias line have their own inductance, and the inductance due to these traces in the deployed array differs from those of the laboratory TES testing apparatus. Therefore it was necessary to predict the inductance of the bias line traces in order to choose the correct additional inductance on the interface chip.

There are three types of superconducting traces involved: those on the detector wafer, those on the flexible cable connecting the detector wafer to the readout PCB, and those on the wiring chips that route the signal from the flexible cable to the interface chip. Each of these types of traces differ geometrically, but were all assumed to be long, straight, and edge-coupled for the purposes of this prediction. See Tab. B.1 for the dimensions of each of these types of traces.

Since series inductances are added to yield total inductance, it suffices to calculate the inductance per unit length of each of these traces, multiply by the total length, and add the three inductance values. To calculate the inductance per

Type	Trace Thickness	Trace Width	Spacing	Material	λ
Wiring Chip	200 nm	15 μm	15 μm	Nb	39 nm
Flexible Cable	400 nm	50 μm	20 μm	Al	16 nm
Detector Wafer	200 nm	5 μm	1 μm	Nb	39 nm

Table B.1: Dimensions of each of the types of traces included in the calculation. Each pair of traces was assumed to be long, straight, and edge-coupled. Thickness and width are the physical dimensions of the trace, and spacing is the pitch between the signal and return lines. The material the trace is composed of is also listed, along with its London penetration depth (λ), which affects the inductance calculation.

Trace Type	Inductance/Length	Length Range	Inductance Range
Wiring Chip	8.64 nH/cm	0.9-5 cm	8-47 nH
Flexible Cable	7.12 nH/cm	2 cm	14 nH
Detector Wafer	6.33 nH/cm	1.3 cm	1.3-40 nH
Total			23-100 nH

Table B.2: Result of the FastHenry simulations for each trace type. The length of the traces varies for each TES on the array, so a range is given. The range of predicted inductance for each trace type is given, as well as the total. Values listed are specifically for the AdvACT high frequency array, but values are similar for the other AdvACT arrays.

unit length, the software `FastHenry` [`https://www.fastfieldsolvers.com`] was used. Each trace type was modeled in a separate simulation as a pair of traces connected at one end to complete the circuit B.1. Several trace lengths were simulated, and the slope of a linear regression to inductance as a function of trace length yielded the inductance per unit length of the trace type. Tab. B.2 shows the results of these simulations. Based on these predictions, no additional inductance was added at the interface chips for Advanced ACTPol arrays. Time constant measurements of these arrays suggest a range of inductance consistent with these predictions (See Fig. B.2).

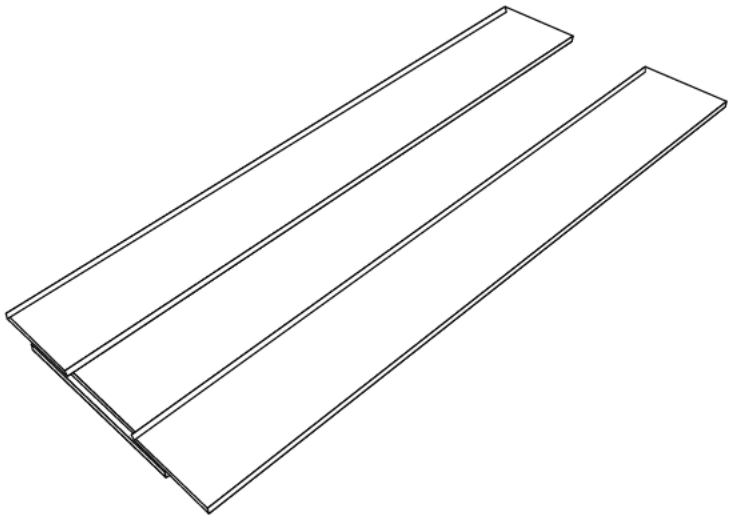

Figure B.1: Example rendering of the simulated traces for the wiring chip. Note one end is connected to complete the circuit. The overall length was varied. See Tab. B.1 for dimensions of this and other trace types.

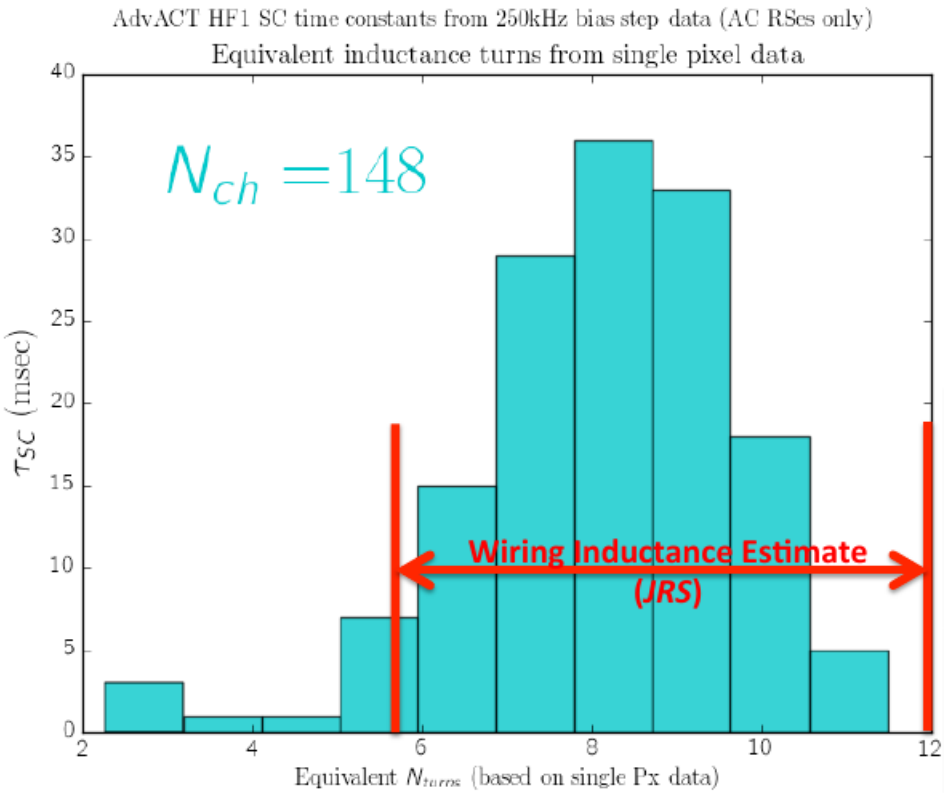

Figure B.2: Advanced ACTPol "equivalent turns" inductance as measured on the high frequency (HF) array using 250kHz time constant data. The red bars show the range of inductances predicted from the FastHenry simulations. The Advanced ACTPol interface chips can be wire bonded with inductors of 0, 9, or 17 turns of the inductive coil. In deployment, 0 turns were selected. The measured inductance is consistent with the inductance of the superconducting traces. Figure is from Shawn Henderson, who collected the time constant data.

BIBLIOGRAPHY

[1] Kevork Abazajian, Peter Adshead, Zeeshan Ahmed, Steven Allen, David Alonso, Kamugisha Arnold, Carlo Baccigalupi, James Bartlett, Nicholas Battaglia, Bradford Benson, Colin Bischoff, Julian Borrill, Victor Buza, Erminia Calabrese, Robert Caldwell, John Carlstrom, Clarence Chang, Thomas Crawford, Francis-Yan Cyr-Racine, and Wai Ling Kimmy Wu. CMB-S4 Science Book, First Edition. 10 2016.

[2] K.N. Abazajian, K. Arnold, J. Austermann, B.A. Benson, C. Bischoff, J. Bock, J.R. Bond, J. Borrill, E. Calabrese, J.E. Carlstrom, C.S. Carvalho, C.L. Chang, H.C. Chiang, S. Church, A. Cooray, T.M. Crawford, K.S. Dawson, S. Das, M.J. Devlin, M. Dobbs, S. Dodelson, O. DorÃ©, J. Dunkley, J. Errard, A. Fraisse, J. Gallicchio, N.W. Halverson, S. Hanany, S.R. Hildebrandt, A. Hincks, R. Hlozek, G. Holder, W.L. Holzapfel, K. Honscheid, W. Hu, J. Hubmayr, K. Irwin, W.C. Jones, M. Kamionkowski, B. Keating, R. Keisler, L. Knox, E. Komatsu, J. Kovac, C.-L. Kuo, C. Lawrence, A.T. Lee, E. Leitch, E. Linder, P. Lubin, J. McMahon, A. Miller, L. Newburgh, M.D. Niemack, H. Nguyen, H.T. Nguyen, L. Page, C. Pryke, C.L. Reichardt, J.E. Ruhl, N. Sehgal, U. Seljak, J. Sievers, E. Silverstein, A. Slosar, K.M. Smith, D. Spergel, S.T. Staggs, A. Stark, R. Stompor, A.G. Vieregg, G. Wang, S. Watson, E.J. Wollack, W.L.K. Wu, K.W. Yoon, and O. Zahn. Neutrino physics from the cosmic microwave background and large scale structure. *Astroparticle Physics*, 63:66 – 80, 2015. Dark Energy and CMB.

[3] Paul A. Abell et al. LSST Science Book, Version 2.0. 12 2009.

[4] Maximilian H. Abitbol, Zeeshan Ahmed, Darcy Barron, Ritoban Basu Thakur, Amy N. Bender, Bradford A. Benson, Colin A. Bischoff, Sean A. Bryan, John E. Carlstrom, Clarence L. Chang, David T. Chuss, Kevin T. Crowley, Ari Cukierman, Tijmen de Haan, Matt Dobbs, Tom Essinger-Hileman, Jeffrey P. Filippini, Ken Ganga, Jon E. Gudmundsson, Nils W. Halverson, Shaul Hanany, Shawn W. Henderson, Charles A. Hill, Shuay-Pwu P. Ho, Johannes Hubmayr, Kent Irwin, Oliver Jeong, Bradley R. Johnson, Sarah A. Kernasovskiy, John M. Kovac, Akito Kusaka, Adrian T. Lee, Salatino Maria, Philip Mauskopf, Jeff J. McMahon, Lorenzo Moncelsi, Andrew W. Nadolski, Johanna M. Nagy, Michael D. Niemack, Roger C. O'Brient, Stephen Padin, Stephen C. Parshley, Clement Pryke, Natalie A. Roe, Karwan Rostem, John Ruhl, Sara M. Simon, Suzanne T. Staggs, Aritoki Suzuki, Eric R. Switzer, Osamu Tajima, Keith L. Thompson, Peter Timbie, Gregory S. Tucker, Joaquin D. Vieira, Abigail G. Vieregg, Benjamin Westbrook, Edward J. Wollack, Ki Won Yoon, Karl S. Young, and Edward Y. Young. Cmb-s4 technology book, first edition, 2017.

[5] Peter Ade, James Aguirre, Zeeshan Ahmed, Simone Aiola, Aamir Ali, David Alonso, Marcelo A. Alvarez, Kam Arnold, Peter Ashton, Jason Austermann, Humna Awan, Carlo Baccigalupi, Taylor Baildon, Darcy Barron, Nick Battaglia, Richard Battye, Eric Baxter, Andrew Bazarko, James A. Beall, Rachel Bean, Dominic Beck, Shawn Beckman, Benjamin Beringue, Federico Bianchini, Steven Boada, David Boettger, J. Richard Bond, Julian Borrill, Michael L. Brown, Sarah Marie Bruno, Sean Bryan, Erminia Calabrese, Victoria Calafut, Paolo Calisse, Julien Carron, Anthony Challinor, Grace Chesmore, Yuji Chinone, Jens Chluba, Hsiao-Mei Sherry Cho, Steve Choi, Gabriele Coppi, Nicholas F. Cothard, Kevin Coughlin, Devin Crichton, Kevin D. Crowley, Kevin T. Crowley, Ari Cukierman, John M. DEwart, Rolando DÃnner, Tijmen de Haan, Mark Devlin, Simon Dicker, Joy Didier, Matt Dobbs, Bradley Dober, Cody J. Duell, Shannon Duff, Adri Duivenvoorden, Jo Dunkley, John Dusatko, Josquin Errard, Giulio Fabbian, Stephen Feeney, Simone Ferraro, Pedro Fluxà, Katherine Freese, Josef C. Frisch, Andrei Frolov, George Fuller, Brittany Fuzia, Nicholas Galitzki, Patricio A. Gallardo, Jose Tomas Galvez Ghersi, Jiansong Gao, Eric Gawiser, Martina Gerbino, Vera Gluscevic, Neil Goeckner-Wald, Joseph Golec, Sam Gordon, Megan Gralla, Daniel Green, Arpi Grigorian, John Groh, Chris Groppi, Yilun Guan, Jon E. Gudmundsson, Dongwon Han, Peter Hargrave, Masaya Hasegawa, Matthew Hasselfield, Makoto Hattori, Victor Haynes, Masashi Hazumi, Yizhou He, Erin Healy, Shawn W. Henderson, Carlos Hervias-Caimapo, Charles A. Hill, J. Colin Hill, Gene Hilton, Matt Hilton, Adam D. Hincks, Gary Hinshaw, Renée Hložek, Shirley Ho, Shuay-Pwu Patty Ho, Logan Howe, Zhiqi Huang, Johannes Hubmayr, Kevin Huffenberger, John P. Hughes, Anna Ijjas, Margaret Ikape, Kent Irwin, Andrew H. Jaffe, Bhuvnesh Jain, Oliver Jeong, Daisuke Kaneko, Ethan D. Karpel, Nobuhiko Katayama, Brian Keating, Sarah S. Kernasovskiy, Reijo Keskitalo, Theodore Kisner, Kenji Kiuchi, Jeff Klein, Kenda Knowles, Brian Koopman, Arthur Kosowsky, Nicoletta Krachmalnicoff, Stephen E. Kuenstner, Chao-Lin Kuo, Akito Kusaka, Jacob Lashner, Adrian Lee, Eunseong Lee, David Leon, Jason S.-Y. Leung, Antony Lewis, Yaqiong Li, Zack Li, Michele Limon, Eric Linder, Carlos Lopez-Caraballo, Thibaut Louis, Lindsay Lowry, Marius Lungu, Mathew Madhavacheril, Daisy Mak, Felipe Maldonado, Hamdi Mani, Ben Mates, Frederick Matsuda, LoÃc Maurin, Phil Mauskopf, Andrew May, Nialh McCallum, Chris McKenney, Jeff McMahon, P. Daniel Meerburg, Joel Meyers, Amber Miller, Mark Mirmelstein, Kavilan Moodley, Moritz Munchmeyer, Charles Munson, Sigurd Naess, Federico Nati, Martin Navaroli, Laura Newburgh, Ho Nam Nguyen, Michael Niemack, Haruki Nishino, John Orlowski-Scherer, Lyman Page, Bruce Partridge, Julien Peloton, Francesca Perrotta, Lucio Piccirillo, Giampaolo Pisano, Davide Poletti, Roberto Puddu, Giuseppe Puglisi, Chris Raum, Christian L. Reichardt, Mathieu Remazeilles, Yoel Rephaeli, Dominik Riechers, Felipe Rojas, Anirban Roy, Sharon Sadeh, Yuki Saku-

rai, Maria Salatino, Mayuri Sathyanarayana Rao, Emmanuel Schaan, Marcel Schmittfull, Neelima Sehgal, Joseph Seibert, Uros Seljak, Blake Sherwin, Meir Shimon, Carlos Sierra, Jonathan Sievers, Precious Sikhosana, Maximiliano Silva-Feaver, Sara M. Simon, Adrian Sinclair, Praween Siritanasak, Kendrick Smith, Stephen R. Smith, David Spergel, Suzanne T. Staggs, George Stein, Jason R. Stevens, Radek Stompor, Aritoki Suzuki, Osamu Tajima, Satoru Takakura, Grant Teply, Daniel B. Thomas, Ben Thorne, Robert Thornton, Hy Trac, Calvin Tsai, Carole Tucker, Joel Ullom, Sunny Vagnozzi, Alexander van Engelen, Jeff Van Lanen, Daniel D. Van Winkle, Eve M. Vavagiakis, Clara Vergès, Michael Vissers, Kasey Wagoner, Samantha Walker, Jon Ward, Ben Westbrook, Nathan Whitehorn, Jason Williams, Joel Williams, Edward J. Wollack, Zhilei Xu, Byeonghee Yu, Cyndia Yu, Fernando Zago, Hezi Zhang, and Ningfeng Zhu and. The simons observatory: science goals and forecasts. *Journal of Cosmology and Astroparticle Physics*, 2019(02):056–056, feb 2019.

[6] N. Aghanim et al. Planck 2018 results. VI. Cosmological parameters. 7 2018.

[7] Simone Aiola, Erminia Calabrese, Loïc Maurin, Sigurd Naess, Benjamin L. Schmitt, Maximilian H. Abitbol, Graeme E. Addison, Peter A. R. Ade, David Alonso, Mandana Amiri, Stefania Amodeo, Elio Angile, Jason E. Austermann, Taylor Baildon, Nick Battaglia, James A. Beall, Rachel Bean, Daniel T. Becker, J Richard Bond, Sarah Marie Bruno, Victoria Calafut, Luis E. Campusano, Felipe Carrero, Grace E. Chesmore, Hsiao mei Cho., Steve K. Choi, Susan E. Clark, Nicholas F. Cothard, Devin Crichton, Kevin T. Crowley, Omar Darwish, Rahul Datta, Edward V. Denison, Mark J. Devlin, Cody J. Duell, Shannon M. Duff, Adriaan J. Duivenvoorden, Jo Dunkley, Rolando Dünner, Thomas Essinger-Hileman, Max Fankhanel, Simone Ferraro, Anna E. Fox, Brittany Fuzia, Patricio A. Gallardo, Vera Gluscevic, Joseph E. Golec, Emily Grace, Megan Gralla, Yilun Guan, Kirsten Hall, Mark Halpern, Dongwon Han, Peter Hargrave, Matthew Hasselfield, Jakob M. Helton, Shawn Henderson, Brandon Hensley, J. Colin Hill, Gene C. Hilton, Matt Hilton, Adam D. Hincks, Renée Hložek, Shuay-Pwu Patty Ho, Johannes Hubmayr, Kevin M. Huffenberger, John P. Hughes, Leopoldo Infante, Kent Irwin, Rebecca Jackson, Jeff Klein, Kenda Knowles, Brian Koopman, Arthur Kosowsky, Vincent Lakey, Dale Li, Yaqiong Li, Zack Li, Martine Lokken, Thibaut Louis, Marius Lungu, Amanda MacInnis, Mathew Madhavacheril, Felipe Maldonado, Maya Mallaby-Kay, Danica Marsden, Jeff McMahon, Felipe Menanteau, Kavilan Moodley, Tim Morton, Toshiya Namikawa, Federico Nati, Laura Newburgh, John P. Nibarger, Andrina Nicola, Michael D. Niemack, Michael R. Nolta, John Orlowski-Sherer, Lyman A. Page, Christine G. Pap-

pas, Bruce Partridge, Phumlani Phakathi, Heather Prince, Roberto Puddu, Frank J. Qu, Jesus Rivera, Naomi Robertson, Felipe Rojas, Maria Salatino, Emmanuel Schaan, Alessandro Schillaci, Neelima Sehgal, Blake D. Sherwin, Carlos Sierra, Jon Sievers, Cristobal Sifon, Precious Sikhosana, Sara Simon, David N. Spergel, Suzanne T. Staggs, Jason Stevens, Emilie Storer, Dhaneshwar D. Sunder, Eric R. Switzer, Ben Thorne, Robert Thornton, Hy Trac, Jesse Treu, Carole Tucker, Leila R. Vale, Alexander Van Engelen, Jeff Van Lanen, Eve M. Vavagiakis, Kasey Wagoner, Yuhan Wang, Jonathan T. Ward, Edward J. Wollack, Zhilei Xu, Fernando Zago, and Ningfeng Zhu. The atacama cosmology telescope: Dr4 maps and cosmological parameters, 2020.

[8] Manuel Aravena, Jason Austermann, Kaustuv Basu, Nicholas Battaglia, Benjamin Beringue, Frank Bertoldi, J. Richard Bond, Patrick Breysse, Ricardo Bustos, Scott Chapman, Steve Choi, Dongwoo Chung, Nicholas Cothard, Bradley Dober, Cody Duell, Shannon Duff, Rolando Dunner, Jens Erler, Michel Fich, Laura Fissel, Simon Foreman, Patricio Gallardo, Jiansong Gao, Riccardo Giovanelli, Urs Graf, Martha Haynes, Terry Herter, Gene Hilton, Renee Hlozek, Johannes Hubmayr, Doug Johnstone, Laura Keating, Eiichiro Komatsu, Benjamin Magnelli, Phil Mauskopf, Jeffrey McMahon, P. Daniel Meerburg, Joel Meyers, Norm Murray, Michael Niemack, Thomas Nikola, Michael Nolta, Stephen Parshley, Roberto Puddu, Dominik Riechers, Erik Rosolowsky, Sara Simon, Gordon Stacey, Jason Stevens, Juergen Stutzki, Alexander Van Engelen, Eve Vavagiakis, Marco Viero, Michael Vissers, Samantha Walker, and Bugao Zou. The ccatprime submillimeter observatory, 2019.

[9] E. S. Battistelli, M. Amiri, B. Burger, M. J. Devlin, S. R. Dicker, W. B. Doriese, R. DÃnner, R. P. Fisher, J. W. Fowler, M. Halpern, M. Hasselfield, G. C. Hilton, A. D. Hincks, K. D. Irwin, M. Kaul, J. Klein, S. Knotek, J. M. Lau, M. Limon, T. A. Marriage, M. D. Niemack, L. Page, C. D. Reintsema, S. T. Staggs, D. S. Swetz, E. R. Switzer, R. J. Thornton, and Y. Zhao. Automated SQUID tuning procedure for kilo-pixel arrays of TES bolometers on the Atacama Cosmology Telescope. In William D. Duncan, Wayne S. Holland, Stafford Withington, and Jonas Zmuidzinas, editors, *Millimeter and Submillimeter Detectors and Instrumentation for Astronomy IV*, volume 7020, pages 618 – 629. International Society for Optics and Photonics, SPIE, 2008.

[10] E. S. Battistelli, M. Amiri, B. Burger, M. Halpern, S. Knotek, M. Ellis, X. Gao, D. Kelly, M. MacIntosh, K. Irwin, and C. Reintsema. Functional description of read-out electronics forâ?time-domain multiplexed bolometers forâ?millimeter and sub-millimeter astronomy. *Journal of Low Temperature Physics*, 151(3):908–914, 2008.

[11] F. De Bernardis, J. R. Stevens, and M. Hasselfield *et al*. Survey strategy optimization for the Atacama Cosmology Telescope. In Alison B. Peck, Robert L. Seaman, and Chris R. Benn, editors, *Observatory Operations: Strategies, Processes, and Systems VI*, volume 9910, pages 359 – 372. International Society for Optics and Photonics, SPIE, 2016.

[12] Mark Birkinshaw. The Sunyaev-Zel'dovich effect. *Phys. Rept.*, 310:97–195, 1999.

[13] Sean M. Carroll. Quintessence and the rest of the world: Suppressing long-range interactions. *Phys. Rev. Lett.*, 81:3067–3070, Oct 1998.

[14] Boris Chesca, Reinhold Kleiner, and Dieter Koelle. *SQUID Theory*, chapter 2, pages 29–92. John Wiley Sons, Ltd, 2005.

[15] S. K. Choi, J. Austermann, K. Basu, N. Battaglia, F. Bertoldi, D. T. Chung, N. F. Cothard, S. Duff, C. J. Duell, P. A. Gallardo, J. Gao, T. Herter, J. Hubmayr, M. D. Niemack, T. Nikola, D. Riechers, K. Rossi, G. J. Stacey, J. R. Stevens, E. M. Vavagiakis, M. Vissers, and S. Walker. Sensitivity of the prime-cam instrument on the ccat-prime telescope. *Journal of Low Temperature Physics*, 199(3):1089–1097, May 2020.

[16] S. K. Choi, J. Austermann, J. A. Beall, K. T. Crowley, R. Datta, S. M. Duff, P. A. Gallardo, S. P. Ho, J. Hubmayr, B. J. Koopman, Y. Li, F. Nati, M. D. Niemack, L. A. Page, M. Salatino, S. M. Simon, S. T. Staggs, J. Stevens, J. Ullom, and E. J. Wollack. Characterization of the mid-frequency arrays for advanced actpol. *Journal of Low Temperature Physics*, 193(3):267–275, 2018.

[17] Steve K. Choi. *Measuring the Cosmic Microwave Background Anisotropy from the Atacama Desert*. PhD thesis, Princeton University, 2018.

[18] Steve K. Choi, Matthew Hasselfield, Shuay-Pwu Patty Ho, Brian Koopman, Marius Lungu, Maximilian H. Abitbol, Graeme E. Addison, Peter A. R. Ade, Simone Aiola, David Alonso, Mandana Amiri, Stefania Amodeo, Elio Angile, Jason E. Austermann, Taylor Baildon, Nick Battaglia, James A. Beall, Rachel Bean, Daniel T. Becker, J Richard Bond, Sarah Marie Bruno, Erminia Calabrese, Victoria Calafut, Luis E. Campusano, Felipe Carrero, Grace E. Chesmore, Hsiao mei Cho., Susan E. Clark, Nicholas F. Cothard, Devin Crichton, Kevin T. Crowley, Omar Darwish, Rahul Datta, Edward V. Denison, Mark J. Devlin, Cody J. Duell, Shannon M. Duff, Adriaan J. Duivenvoorden, Jo Dunkley, Rolando Dünner, Thomas Essinger-Hileman, Max Fankhanel, Simone Ferraro, Anna E. Fox, Brittany Fuzia, Patricio A. Gallardo, Vera Gluscevic, Joseph E. Golec, Emily Grace, Megan Gralla, Yilun

Guan, Kirsten Hall, Mark Halpern, Dongwon Han, Peter Hargrave, Shawn Henderson, Brandon Hensley, J. Colin Hill, Gene C. Hilton, Matt Hilton, Adam D. Hincks, Renée Hložek, Johannes Hubmayr, Kevin M. Huffenberger, John P. Hughes, Leopoldo Infante, Kent Irwin, Rebecca Jackson, Jeff Klein, Kenda Knowles, Arthur Kosowsky, Vincent Lakey, Dale Li, Yaqiong Li, Zack Li, Martine Lokken, Thibaut Louis, Amanda MacInnis, Mathew Madhavacheril, Felipe Maldonado, Maya Mallaby-Kay, Danica Marsden, Loïc Maurin, Jeff McMahon, Felipe Menanteau, Kavilan Moodley, Tim Morton, Sigurd Naess, Toshiya Namikawa, Federico Nati, Laura Newburgh, John P. Nibarger, Andrina Nicola, Michael D. Niemack, Michael R. Nolta, John Orlowski-Sherer, Lyman A. Page, Christine G. Pappas, Bruce Partridge, Phumlani Phakathi, Heather Prince, Roberto Puddu, Frank J. Qu, Jesus Rivera, Naomi Robertson, Felipe Rojas, Maria Salatino, Emmanuel Schaan, Alessandro Schillaci, Benjamin L. Schmitt, Neelima Sehgal, Blake D. Sherwin, Carlos Sierra, Jon Sievers, Cristobal Sifon, Precious Sikhosana, Sara Simon, David N. Spergel, Suzanne T. Staggs, Jason Stevens, Emilie Storer, Dhaneshwar D. Sunder, Eric R. Switzer, Ben Thorne, Robert Thornton, Hy Trac, Jesse Treu, Carole Tucker, Leila R. Vale, Alexander Van Engelen, Jeff Van Lanen, Eve M. Vavagiakis, Kasey Wagoner, Yuhan Wang, Jonathan T. Ward, Edward J. Wollack, Zhilei Xu, Fernando Zago, and Ningfeng Zhu. The atacama cosmology telescope: A measurement of the cosmic microwave background power spectra at 98 and 150 ghz, 2020.

[19] J. Clarke and A. I. Braginski, editors. *The SQUID handbook*. Wiley-VCH, Weinheim, 2004. OCLC: ocm52746892.

[20] Kyle S. Dawson and David J. Schlegel *et al*. THE BARYON OSCILLATION SPECTROSCOPIC SURVEY OF SDSS-III. *The Astronomical Journal*, 145(1):10, dec 2012.

[21] Roland de Putter, Oliver Zahn, and Eric V. Linder. Cmb lensing constraints on neutrinos and dark energy. *Phys. Rev. D*, 79:065033, Mar 2009.

[22] Suhail Dhawan, Saurabh W. Jha, and Bruno Leibundgut. Measuring the Hubble constant with Type Ia supernovae as near-infrared standard candles. *Astron. Astrophys.*, 609:A72, 2018.

[23] M. A. Dobbs, M. Lueker, K. A. Aird, A. N. Bender, B. A. Benson, L. E. Bleem, J. E. Carlstrom, C. L. Chang, H.-M. Cho, J. Clarke, T. M. Crawford, A. T. Crites, D. I. Flanigan, T. de Haan, E. M. George, N. W. Halverson, W. L. Holzapfel, J. D. Hrubes, B. R. Johnson, J. Joseph, R. Keisler, J. Kennedy, Z. Kermish, T. M. Lanting, A. T. Lee, E. M. Leitch, D. Luong-Van, J. J.

McMahon, J. Mehl, S. S. Meyer, T. E. Montroy, S. Padin, T. Plagge, C. Pryke, P. L. Richards, J. E. Ruhl, K. K. Schaffer, D. Schwan, E. Shirokoff, H. G. Spieler, Z. Staniszewski, A. A. Stark, K. Vanderlinde, J. D. Vieira, C. Vu, B. Westbrook, and R. Williamson. Frequency multiplexed superconducting quantum interference device readout of large bolometer arrays for cosmic microwave background measurements. *Review of Scientific Instruments*, 83(7):073113, 2012.

[24] Scott Dodelson. *Modern cosmology*. Academic Press, 2011.

[25] W. B. Doriese, K. M. Morgan, D. A. Bennett, E. V. Denison, C. P. Fitzgerald, J. W. Fowler, J. D. Gard, J. P. Hays-Wehle, G. C. Hilton, K. D. Irwin, Y. I. Joe, J. A. B. Mates, G. C. OâEUR(tm)Neil, C. D. Reintsema, N. O. Robbins, D. R. Schmidt, D. S. Swetz, H. Tatsuno, L. R. Vale, and J. N. Ullom. Developments in time-division multiplexing of x-ray transition-edge sensors. *Journal of Low Temperature Physics*, 184(1):389–395, 2016.

[26] Peter Ade *et al*. The simons observatory: science goals and forecasts. *Journal of Cosmology and Astroparticle Physics*, 2019(02):056–056, feb 2019.

[27] Brent Follin, Lloyd Knox, Marius Millea, and Zhen Pan. First detection of the acoustic oscillation phase shift expected from the cosmic neutrino background. *Phys. Rev. Lett.*, 115:091301, Aug 2015.

[28] Patricio A. Gallardo, Nicholas F. Cothard, Roberto Puddu, Rolando Dünner, Brian J. Koopman, Michael D. Niemack, Sara M. Simon, and Edward J. Wollack. Far sidelobes from baffles and telescope support structures in the Atacama Cosmology Telescope. In Jonas Zmuidzinas and Jian-Rong Gao, editors, *Millimeter, Submillimeter, and Far-Infrared Detectors and Instrumentation for Astronomy IX*, volume 10708, pages 369 – 378. International Society for Optics and Photonics, SPIE, 2018.

[29] Shawn W. Henderson et al. Highly-multiplexed microwave SQUID readout using the SLAC microresonator radio frequency (SMuRF) electronics for future CMB and sub-millimeter surveys (Conference Presentation). *Proc. SPIE Int. Soc. Opt. Eng.*, 10708:1070819, 2018.

[30] Shawn W. Henderson, Jason R. Stevens, Mandana Amiri, Jason Austermann, James A. Beall, Saptarshi Chaudhuri, Hsiao-Mei Cho, Steve K. Choi, Nicholas F. Cothard, Kevin T. Crowley, Shannon M. Duff, Colin P. Fitzgerald, Patricio A. Gallardo, Mark Halpern, Matthew Hasselfield, Gene Hilton, Shuay-Pwu Patty Ho, Johannes Hubmayr, Kent D. Irwin, Brian J. Koopman, Dale Li, Yaqiong Li, Jeff McMahon, Federico Nati, Michael

Niemack, Carl D. Reintsema, Maria Salatino, Alessandro Schillaci, Benjamin L. Schmitt, Sara M. Simon, Suzanne T. Staggs, Eve M. Vavagiakis, and Jonathan T. Ward. Readout of two-kilopixel transition-edge sensor arrays for Advanced ACTPol. In Wayne S. Holland and Jonas Zmuidzinas, editors, *Millimeter, Submillimeter, and Far-Infrared Detectors and Instrumentation for Astronomy VIII*, volume 9914, pages 346 – 362. International Society for Optics and Photonics, SPIE, 2016.

[31] Charles A. Hill, Sarah Marie M. Bruno, and Sara M. Simon *et al*. BoloCalc: a sensitivity calculator for the design of Simons Observatory. In Jonas Zmuidzinas and Jian-Rong Gao, editors, *Millimeter, Submillimeter, and Far-Infrared Detectors and Instrumentation for Astronomy IX*, volume 10708, pages 698 – 718. International Society for Optics and Photonics, SPIE, 2018.

[32] Eric Hivon, Krzysztof M. Gorski, C. Barth Netterfield, Brendan P. Crill, Simon Prunet, and Frode Hansen. MASTER of the cosmic microwave background anisotropy power spectrum: A fast method for statistical analysis of large and complex cosmic microwave background data sets. *The Astrophysical Journal*, 567(1):2–17, mar 2002.

[33] Shuay-Pwu Patty Ho, Jason Austermann, James A. Beall, Steve K. Choi, Nicholas F. Cothard, Kevin T. Crowley, Rahul Datta, Mark J. Devlin, Shannon M. Duff, Patricio A. Gallardo, Matthew Hasselfield, Shawn W. Henderson, Gene Hilton, Johannes Hubmayr, Brian J. Koopman, Yaqiong Li, Jeffrey McMahon, Michael D. Niemack, Maria Salatino, Sara M. Simon, Suzanne T. Staggs, Jonathan T. Ward, Joel N. Ullom, Eve M. Vavagiakis, and Edward J. Wollack. Highly uniform 150 mm diameter multichroic polarimeter array deployed for CMB detection. In Wayne S. Holland and Jonas Zmuidzinas, editors, *Millimeter, Submillimeter, and Far-Infrared Detectors and Instrumentation for Astronomy VIII*, volume 9914, pages 301 – 315. International Society for Optics and Photonics, SPIE, 2017.

[34] W. S. Holland, D. Bintley, E. L. Chapin, A. Chrysostomou, G. R. Davis, J. T. Dempsey, W. D. Duncan, M. Fich, P. Friberg, M. Halpern, K. D. Irwin, T. Jenness, B. D. Kelly, M. J. MacIntosh, E. I. Robson, D. Scott, P. A. R. Ade, E. Atad-Ettedgui, D. S. Berry, S. C. Craig, X. Gao, A. G. Gibb, G. C. Hilton, M. I. Hollister, J. B. Kycia, D. W. Lunney, H. McGregor, D. Montgomery, W. Parkes, R. P. J. Tilanus, J. N. Ullom, C. A. Walther, A. J. Walton, A. L. Woodcraft, M. Amiri, D. Atkinson, B. Burger, T. Chuter, I. M. Coulson, W. B. Doriese, C. Dunare, F. Economou, M. D. Niemack, H. A. L. Parsons, C. D. Reintsema, B. Sibthorpe, I. Smail, R. Sudiwala, and H. S. Thomas. SCUBA-2: the 10 000 pixel bolometer camera on the James Clerk Maxwell

Telescope. *Monthly Notices of the Royal Astronomical Society*, 430(4):2513–2533, 03 2013.

[35] Howard Hui, P. A. R. Ade, Z. Ahmed, R. W. Aikin, K. D. Alexander, D. Barkats, S. J. Benton, C. A. Bischoff, J. J. Bock, R. Bowens-Rubin, J. A. Brevik, I. Buder, E. Bullock, V. Buza, J. Connors, J. Cornelison, B. P. Crill, M. Crumrine, M. Dierickx, L. Duband, C. Dvorkin, J. P. Filippini, S. Fliescher, J. Grayson, G. Hall, M. Halpern, S. Harrison, S. R. Hildebrandt, G. C. Hilton, K. D. Irwin, J. Kang, K. S. Karkare, E. Karpel, J. P. Kaufman, B. G. Keating, S. Kefeli, S. A. Kernasovskiy, J. M. Kovac, C.-L. Kuo, K. Lau, N. A. Larsen, E. M. Leitch, M. Lueker, K. G. Megerian, L. Moncelsi, T. Namikawa, C. B. Netterfield, H. T. Nguyen, R. O'Brient, R. W. Ogburn IV, S. Palladino, C. Pryke, B. Racine, S. Richter, R. Schwarz, A. Schillaci, C. D. Sheehy, A. Soliman, T. St. Germaine, Z. K. Staniszewski, B. Steinbach, R. V. Sudiwala, G. P. Teply, K. L. Thompson, J. E. Tolan, C. Tucker, A. D. Turner, C. UmiltÃ , A. G. Vieregg, A. Wandui, A. C. Weber, D. V. Wiebe, J. Willmert, C. L. Wong, W. L. K. Wu, E. Yang, K. W. Yoon, and C. Zhang. BICEP Array: a multi-frequency degree-scale CMB polarimeter. In Jonas Zmuidzinas and Jian-Rong Gao, editors, *Millimeter, Submillimeter, and Far-Infrared Detectors and Instrumentation for Astronomy IX*, volume 10708, pages 1 – 15. International Society for Optics and Photonics, SPIE, 2018.

[36] K.D. Irwin and G.C. Hilton. *Transition-Edge Sensors*, pages 63–150. Springer Berlin Heidelberg, Berlin, Heidelberg, 2005.

[37] Marc Kamionkowski. How to derotate the cosmic microwave background polarization. *Phys. Rev. Lett.*, 102:111302, Mar 2009.

[38] Marc Kamionkowski and Ely D. Kovetz. The quest for b modes from inflationary gravitational waves. *Annual Review of Astronomy and Astrophysics*, 54(1):227–269, 2016.

[39] D. Larson et al. Seven-Year Wilkinson Microwave Anisotropy Probe (WMAP) Observations: Power Spectra and WMAP-Derived Parameters. *Astrophys. J. Suppl.*, 192:16, 2011.

[40] Antony Lewis and Anthony Challinor. Weak gravitational lensing of the CMB. *Phys. Rept.*, 429:1–65, 2006.

[41] Dale Li, Jason E. Austermann, James A. Beall, Daniel T. Becker, Shannon M. Duff, Patricio A. Gallardo, Shawn W. Henderson, Gene C. Hilton, Shuay-Pwu Ho, Johannes Hubmayr, Brian J. Koopman, Jeffrey J. McMahon, Federico Nati, Michael D. Niemack, Christine G. Pappas, Maria Salatino,

Benjamin L. Schmitt, Sara M. Simon, Suzanne T. Staggs, Jeff Van Lanen, Jonathan T. Ward, and Edward J. Wollack. Almn transition edge sensors for advanced actpol. *Journal of Low Temperature Physics*, 184(1):66–73, Jul 2016.

[42] Yaqiong Li, Jason E. Austermann, James A. Beall, Sarah Marie Bruno, Steve K. Choi, Nicholas F. Cothard, Kevin T. Crowley, Shannon M. Duff, Patricio A. Gallardo, Shawn W. Henderson, Shuay-Pwu Patty Ho, Johannes Hubmayr, Brian J. Koopman, Jeff J. McMahon, Michael D. Niemack, Maria Salatino, Sara M. Simon, Suzanne T. Staggs, Jason R. Stevens, Joel N. Ullom, Jonathan Ward, and Edward J. Wollack. Performance of the advanced ACTPol low frequency array . In Jonas Zmuidzinas and Jian-Rong Gao, editors, *Millimeter, Submillimeter, and Far-Infrared Detectors and Instrumentation for Astronomy IX*, volume 10708, pages 16 – 24. International Society for Optics and Photonics, SPIE, 2018.

[43] Thibaut Louis et al. The Atacama Cosmology Telescope: Two-Season ACTPol Spectra and Parameters. *JCAP*, 06:031, 2017.

[44] Kevin MacDermid, Peter Hyland, Francois Aubin, Eric Bissonnette, Matt Dobbs, Johannes Hubmayr, Graeme Smecher, and Shahjahen Wairrach. Tuning of Kilopixel Transition Edge Sensor Bolometer Arrays with a Digital Frequency Multiplexed Readout System. *AIP Conf. Proc.*, 1185(1):253, 2009.

[45] John Arthur Benson Mates. *The Microwave SQUID Multiplexer*. PhD thesis, University of Colorado Boulder, 2011.

[46] Benjamin A. Mazin. *Microwave Kinetic Inductance Detectors*. PhD thesis, California Institute of Technology, 2005.

[47] Eva-Maria Mueller, Francesco de Bernardis, Rachel Bean, and Michael D. Niemack. Constraints on gravity and dark energy from the pairwise kinematic Sunyaev-Zeldovich effect. *Astrophys. J.*, 808(1):47, 2015.

[48] Eva-Maria Mueller, Francesco de Bernardis, Rachel Bean, and Michael D. Niemack. Constraints on massive neutrinos from the pairwise kinematic sunyaev-zel'dovich effect. *Phys. Rev. D*, 92:063501, Sep 2015.

[49] John L. Orlowski-Scherer, Ningfeng Zhu, Zhilei Xu, Aamir Ali, Kam S. Arnold, Peter C. Ashton, Gabriele Coppi, Mark Devlin, Simon Dicker, Nicholas Galitzki, Patricio A. Gallardo, Brian Keating, Adrian T. Lee,

Michele Limon, Marius Lungu, Andrew May, Jeff McMahon, Michael D. Niemack, Lucio Piccirillo, Giuseppe Puglisi, Maria Salatino, Max Silva-Feaver, Sara M. Simon, Robert Thornton, and Eve M. Vavagiakis. Simons Observatory large aperture receiver simulation overview. In Jonas Zmuidzinas and Jian-Rong Gao, editors, *Millimeter, Submillimeter, and Far-Infrared Detectors and Instrumentation for Astronomy IX*, volume 10708, pages 644 – 657. International Society for Optics and Photonics, SPIE, 2018.

[50] Nikhil Padmanabhan and Douglas P. Finkbeiner. Detecting dark matter annihilation with cmb polarization: Signatures and experimental prospects. *Phys. Rev. D*, 72:023508, Jul 2005.

[51] Planck Collaboration, Aghanim, N., Arnaud, M., Ashdown, M., Aumont, J., Baccigalupi, C., Banday, A. J., Barreiro, R. B., Bartlett, J. G., Bartolo, N., Battaner, E., Benabed, K., Benoît, A., Benoit-Lévy, A., Bernard, J.-P., Bersanelli, M., Bielewicz, P., Bock, J. J., Bonaldi, A., Bonavera, L., Bond, J. R., Borrill, J., Bouchet, F. R., Boulanger, F., Bucher, M., Burigana, C., Butler, R. C., Calabrese, E., Cardoso, J.-F., Catalano, A., Challinor, A., Chiang, H. C., Christensen, P. R., Clements, D. L., Colombo, L. P. L., Combet, C., Coulais, A., Crill, B. P., Curto, A., Cuttaia, F., Danese, L., Davies, R. D., Davis, R. J., de Bernardis, P., de Rosa, A., de Zotti, G., Delabrouille, J., Désert, F.-X., Di Valentino, E., Dickinson, C., Diego, J. M., Dolag, K., Dole, H., Donzelli, S., Doré, O., Douspis, M., Ducout, A., Dunkley, J., Dupac, X., Efstathiou, G., Elsner, F., Enßlin, T. A., Eriksen, H. K., Fergusson, J., Finelli, F., Forni, O., Frailis, M., Fraisse, A. A., Franceschi, E., Frejsel, A., Galeotta, S., Galli, S., Ganga, K., Gauthier, C., Gerbino, M., Giard, M., Gjerløw, E., González-Nuevo, J., Górski, K. M., Gratton, S., Gregorio, A., Gruppuso, A., Gudmundsson, J. E., Hamann, J., Hansen, F. K., Harrison, D. L., Helou, G., Henrot-Versillé, S., Hernández-Monteagudo, C., Herranz, D., Hildebrandt, S. R., Hivon, E., Holmes, W. A., Hornstrup, A., Huffenberger, K. M., Hurier, G., Jaffe, A. H., Jones, W. C., Juvela, M., Keihänen, E., Keskitalo, R., Kiiveri, K., Knoche, J., Knox, L., Kunz, M., Kurki-Suonio, H., Lagache, G., Lähteenmäki, A., Lamarre, J.-M., Lasenby, A., Lattanzi, M., Lawrence, C. R., Le Jeune, M., Leonardi, R., Lesgourgues, J., Levrier, F., Lewis, A., Liguori, M., Lilje, P. B., Lilley, M., Linden-Vørnle, M., Lindholm, V., López-Caniego, M., Macías-Pérez, J. F., Maffei, B., Maggio, G., Maino, D., Mandolesi, N., Mangilli, A., Maris, M., Martin, P. G., Martínez-González, E., Masi, S., Matarrese, S., Meinhold, P. R., Melchiorri, A., Migliaccio, M., Millea, M., Mitra, S., Miville-Deschênes, M.-A., Moneti, A., Montier, L., Morgante, G., Mortlock, D., Mottet, S., Munshi, D., Murphy, J. A., Narimani, A., Naselsky, P., Nati, F., Natoli, P., Noviello, F., Novikov, D., Novikov, I., Oxborrow, C. A., Paci, F., Pagano, L., Pajot, F., Paoletti, D., Partridge, B., Pasian, F., Patanchon, G., Pearson, T. J., Perdereau, O., Perotto, L.,

Pettorino, V., Piacentini, F., Piat, M., Pierpaoli, E., Pietrobon, D., Plaszczynski, S., Pointecouteau, E., Polenta, G., Ponthieu, N., Pratt, G. W., Prunet, S., Puget, J.-L., Rachen, J. P., Reinecke, M., Remazeilles, M., Renault, C., Renzi, A., Ristorcelli, I., Rocha, G., Rossetti, M., Roudier, G., Rouillé d´Orfeuil, B., Rubiño-Martín, J. A., Rusholme, B., Salvati, L., Sandri, M., Santos, D., Savelainen, M., Savini, G., Scott, D., Serra, P., Spencer, L. D., Spinelli, M., Stolyarov, V., Stompor, R., Sunyaev, R., Sutton, D., Suur-Uski, A.-S., Sygnet, J.-F., Tauber, J. A., Terenzi, L., Toffolatti, L., Tomasi, M., Tristram, M., Trombetti, T., Tucci, M., Tuovinen, J., Umana, G., Valenziano, L., Valiviita, J., Van Tent, F., Vielva, P., Villa, F., Wade, L. A., Wandelt, B. D., Wehus, I. K., Yvon, D., Zacchei, A., and Zonca, A. Planck 2015 results - xi. cmb power spectra, likelihoods, and robustness of parameters. *A&A*, 594:A11, 2016.

[52] S. Probst, F. B. Song, P. A. Bushev, A. V. Ustinov, and M. Weides. Efficient and robust analysis of complex scattering data under noise in microwave resonators. *Review of Scientific Instruments*, 86(2):024706, 2015.

[53] Adam G. Riess, Stefano Casertano, Wenlong Yuan, Lucas M. Macri, and Dan Scolnic. Large Magellanic Cloud Cepheid Standards Provide a 1% Foundation for the Determination of the Hubble Constant and Stronger Evidence for Physics beyond ΛCDM. *Astrophys. J.*, 876(1):85, 2019.

[54] Mayuri Sathyanarayana Rao, Maximiliano Silva-Feaver, Aamir Ali, Kam Arnold, Peter Ashton, Bradley J. Dober, Cody J. Duell, Shannon M. Duff, Nicholas Galitzki, Erin Healy, Shawn Henderson, Shuay-Pwu Patty Ho, Jonathan Hoh, Anna M. Kofman, Akito Kusaka, Adrian T. Lee, Aashrita Mangu, Justin Mathewson, Philip Mauskopf, Heather McCarrick, Jenna Moore, Michael D. Niemack, Christopher Raum, Maria Salatino, Trevor Sasse, Joseph Seibert, Sara M. Simon, Suzanne Staggs, Jason R. Stevens, Grant Teply, Robert Thornton, Joel Ullom, Eve M. Vavagiakis, Benjamin Westbrook, Zhilei Xu, and Ningfeng Zhu. Simons observatory microwave squid multiplexing readout: Cryogenic rf amplifier and coaxial chain design. *Journal of Low Temperature Physics*, 199(3):807–816, May 2020.

[55] Blake D. Sherwin, Joanna Dunkley, Sudeep Das, John W. Appel, J. Richard Bond, C. Sofia Carvalho, Mark J. Devlin, Rolando Dünner, Thomas Essinger-Hileman, Joseph W. Fowler, Amir Hajian, Mark Halpern, Matthew Hasselfield, Adam D. Hincks, Renée Hlozek, John P. Hughes, Kent D. Irwin, Jeff Klein, Arthur Kosowsky, Tobias A. Marriage, Danica Marsden, Kavilan Moodley, Felipe Menanteau, Michael D. Niemack, Michael R. Nolta, Lyman A. Page, Lucas Parker, Erik D. Reese, Benjamin L. Schmitt, Neelima Sehgal, Jon Sievers, David N. Spergel, Suzanne T. Staggs, Daniel S. Swetz, Eric R. Switzer, Robert Thornton, Katerina Visnjic, and

Ed Wollack. Evidence for dark energy from the cosmic microwave background alone using the atacama cosmology telescope lensing measurements. *Phys. Rev. Lett.*, 107:021302, Jul 2011.

[56] Jason R. Stevens, Nicholas F. Cothard, Eve M. Vavagiakis, Aamir Ali, Kam Arnold, Jason E. Austermann, Steve K. Choi, Bradley J. Dober, Cody Duell, Shannon M. Duff, Gene C. Hilton, Shuay-Pwu Patty Ho, Thuong D. Hoang, Johannes Hubmayr, Adrian T. Lee, Aashrita Mangu, Federico Nati, Michael D. Niemack, Christopher Raum, Mario Renzullo, Maria Salatino, Trevor Sasse, Sara M. Simon, Suzanne Staggs, Aritoki Suzuki, Patrick Truitt, Joel Ullom, John Vivalda, Michael R. Vissers, Samantha Walker, Benjamin Westbrook, Edward J. Wollack, Zhilei Xu, and Daniel Yohannes. Characterization of transition edge sensors for the simons observatory. *Journal of Low Temperature Physics*, 2020.

[57] Jason R. Stevens, Neil Goeckner-Wald, Reijo Keskitalo, and Nialh McCallum *et al*. Designs for next generation CMB survey strategies from Chile. In Jonas Zmuidzinas and Jian-Rong Gao, editors, *Millimeter, Submillimeter, and Far-Infrared Detectors and Instrumentation for Astronomy IX*, volume 10708, pages 698 – 712. International Society for Optics and Photonics, SPIE, 2018.

[58] M. Tanabashi, K. Hagiwara, K. Hikasa, K. Nakamura, Y. Sumino, F. Takahashi, J. Tanaka, K. Agashe, G. Aielli, C. Amsler, M. Antonelli, D. M. Asner, H. Baer, Sw. Banerjee, R. M. Barnett, T. Basaglia, C. W. Bauer, J. J. Beatty, V. I. Belousov, J. Beringer, S. Bethke, A. Bettini, H. Bichsel, O. Biebel, K. M. Black, E. Blucher, O. Buchmuller, V. Burkert, M. A. Bychkov, R. N. Cahn, M. Carena, A. Ceccucci, A. Cerri, D. Chakraborty, M.-C. Chen, R. S. Chivukula, G. Cowan, O. Dahl, G. D'Ambrosio, T. Damour, D. de Florian, A. de Gouvêa, T. DeGrand, P. de Jong, G. Dissertori, B. A. Dobrescu, M. D'Onofrio, M. Doser, M. Drees, H. K. Dreiner, D. A. Dwyer, P. Eerola, S. Eidelman, J. Ellis, J. Erler, V. V. Ezhela, W. Fetscher, B. D. Fields, R. Firestone, B. Foster, A. Freitas, H. Gallagher, L. Garren, H.-J. Gerber, G. Gerbier, T. Gershon, Y. Gershtein, T. Gherghetta, A. A. Godizov, M. Goodman, C. Grab, A. V. Gritsan, C. Grojean, D. E. Groom, M. Grünewald, A. Gurtu, T. Gutsche, H. E. Haber, C. Hanhart, S. Hashimoto, Y. Hayato, K. G. Hayes, A. Hebecker, S. Heinemeyer, B. Heltsley, J. J. Hernández-Rey, J. Hisano, A. Höcker, J. Holder, A. Holtkamp, T. Hyodo, K. D. Irwin, K. F. Johnson, M. Kado, M. Karliner, U. F. Katz, S. R. Klein, E. Klempt, R. V. Kowalewski, F. Krauss, M. Kreps, B. Krusche, Yu. V. Kuyanov, Y. Kwon, O. Lahav, J. Laiho, J. Lesgourgues, A. Liddle, Z. Ligeti, C.-J. Lin, C. Lippmann, T. M. Liss, L. Littenberg, K. S. Lugovsky, S. B. Lugovsky, A. Lusiani, Y. Makida, F. Maltoni, T. Mannel, A. V. Manohar, W. J. Marciano, A. D. Martin, A. Masoni, J. Matthews, U.-G. Meißner, D. Milstead, R. E. Mitchell, K. Mönig,

P. Molaro, F. Moortgat, M. Moskovic, H. Murayama, M. Narain, P. Nason, S. Navas, M. Neubert, P. Nevski, Y. Nir, K. A. Olive, S. Pagan Griso, J. Parsons, C. Patrignani, J. A. Peacock, M. Pennington, S. T. Petcov, V. A. Petrov, E. Pianori, A. Piepke, A. Pomarol, A. Quadt, J. Rademacker, G. Raffelt, B. N. Ratcliff, P. Richardson, A. Ringwald, S. Roesler, S. Rolli, A. Romaniouk, L. J. Rosenberg, J. L. Rosner, G. Rybka, R. A. Ryutin, C. T. Sachrajda, Y. Sakai, G. P. Salam, S. Sarkar, F. Sauli, O. Schneider, K. Scholberg, A. J. Schwartz, D. Scott, V. Sharma, S. R. Sharpe, T. Shutt, M. Silari, T. Sjöstrand, P. Skands, T. Skwarnicki, J. G. Smith, G. F. Smoot, S. Spanier, H. Spieler, C. Spiering, A. Stahl, S. L. Stone, T. Sumiyoshi, M. J. Syphers, K. Terashi, J. Terning, U. Thoma, R. S. Thorne, L. Tiator, M. Titov, N. P. Tkachenko, N. A. Törnqvist, D. R. Tovey, G. Valencia, R. Van de Water, N. Varelas, G. Venanzoni, L. Verde, M. G. Vincter, P. Vogel, A. Vogt, S. P. Wakely, W. Walkowiak, C. W. Walter, D. Wands, D. R. Ward, M. O. Wascko, G. Weiglein, D. H. Weinberg, E. J. Weinberg, M. White, L. R. Wiencke, S. Willocq, C. G. Wohl, J. Womersley, C. L. Woody, R. L. Workman, W.-M. Yao, G. P. Zeller, O. V. Zenin, R.-Y. Zhu, S.-L. Zhu, F. Zimmermann, P. A. Zyla, J. Anderson, L. Fuller, V. S. Lugovsky, and P. Schaffner. Review of particle physics. *Phys. Rev. D*, 98:030001, Aug 2018.

[59] Daniel Thomas, Nialh McCallum, and Michael Brown. Controlling systematics in ground-based cmb surveys with partial boresight rotation, 05 2019.

[60] `https://casper.ssl.berkeley.edu/wiki/ROACH2`.

[61] `http://star-www.st-and.ac.uk/~fv/webnotes/chapter7.htm`.

[62] E. M. Vavagiakis, S. W. Henderson, K. Zheng, H.-M. Cho, N. F. Cothard, B. Dober, S. M. Duff, P. A. Gallardo, G. Hilton, J. Hubmayr, K. D. Irwin, B. J. Koopman, D. Li, F. Nati, M. D. Niemack, C. D. Reintsema, S. Simon, J. R. Stevens, A. Suzuki, and B. Westbrook. Magnetic sensitivity of almn teses and shielding considerations for next-generation cmb surveys. *Journal of Low Temperature Physics*, 193(3):288–297, Nov 2018.

[63] Steven Weinberg. *Cosmology*. Oxford, 2008.

[64] Ningfeng Zhu, John L. Orlowski-Scherer, Zhilei Xu, Aamir Ali, Kam S. Arnold, Peter C. Ashton, Gabriele Coppi, Mark J. Devlin, Simon Dicker, Nicholas Galitzki, Patricio A. Gallardo, Shawn W. Henderson, Shuay-Pwu Patty Ho, Johannes Hubmayr, Brian Keating, Adrian T. Lee, Michele Limon, Marius Lungu, Philip D. Mauskopf, Andrew J. May, Jeff McMahon,

Michael D. Niemack, Lucio Piccirillo, Giuseppe Puglisi, Mayuri Sathyanarayana Rao, Maria Salatino, Max Silva-Feaver, Sara M. Simon, Suzanne Staggs, Robert Thornton, Joel N. Ullom, Eve M. Vavagiakis, Benjamin Westbrook, and Edward J. Wollack. Simons Observatory large aperture telescope receiver design overview. In Jonas Zmuidzinas and Jian-Rong Gao, editors, *Millimeter, Submillimeter, and Far-Infrared Detectors and Instrumentation for Astronomy IX*, volume 10708, pages 259 – 273. International Society for Optics and Photonics, SPIE, 2018.